UNIVERSITY OF CALIFORNIA SAN DIEGO

Activated Sintering of TiO_2 and Field Assisted Sintering of ZnO based Materials

A dissertation submitted in partial satisfaction of the
requirements for the degree Doctor of Philosophy

in

Chemical Engineering

by

Jiuyuan Nie

Committee in charge:

Professor Jian Luo, Chair
Professor Javier Garay
Professor Olivia Graeve
Professor Kenneth S. Vecchio
Professor Kesong Yang

2019

The Dissertation of Jiuyuan Nie is approved, and it is acceptable in quality and form for publication on microfilm and electronically:

_____

_____

_____

_____

_____

Chair

University of California San Diego

2019

DEDICATION

To my mother, Ms. Yuzhi Li

TABLE OF CONTENTS

LIST OF FIGURES

LIST OF TABLES

ACKNOWLEDGEMENTS

I greatly appreciate the supports from other people throughout my graduate study. First, I would like to thank my Ph.D. advisor, Dr. Jian Luo, for his education of research fundamentals and guidance on multiple projects. He introduced me to methodologies of research and critical thinking, which I believe will benefit my life in many ways in the future. It was a great honor to learn from him in the past five years. I would also like to thank my committee members, Dr. Olivia Graeve, Dr. Javier Garay, Dr. Kenneth S. Vecchio, and Dr. Kesong Yang, for their valuable suggestions and precious time.

Secondly, I would like to acknowledge my collaborators and co-authors, Dr. Yuanyao Zhang, Dr. Jiajia Huang, Dr. Rongxia Huang, Dr. Naixie Zhou, Jonathan M. Chan, Mingde Qin, Sicong Jiang, and Haoyang Leng, with whom I had many valuable discussions. I am also thankful to Dr. Tao Hu for his training on electron microscopy.

I'm also grateful to my group members, Dr. Shengfeng Yang, Dr. Mojtaba Samiee, Dr. Joshua Gild, Andrew Wright, Chongze Hu, Qizhang Yan, Shu-Ting Ko, and Sheng Zhao, for the stimulating discussions and advices. I would also like to thank other colleagues, Dr. Chaoyi Zhu and Dr. Shiteng Zhao for their help and friendship. I also want to express my gratitude to Dr. Jeff Wu at Nano3 Facility, Wayne Neilson, Sabine Foulhaber, and Dr. Steve Horvath at NanoEngineering for their technical supports in the past few years. It is a great honor to be part of the NanoEngineering Community at UCSD.

Lastly and most importantly, I would like to thank my family members, Yuzhi Li, Yulan Wang, Chang'e Nie, and Danning Huang for their love, understanding, and encouragement.

Chapter 2, in part, is a reprint of the material "Liquid-Like Grain Boundary Complexion and Sub-Eutectic Activated Sintering in CuO-Doped TiO_2", J. Nie, J.M. Chan, M. Qin, N. Zhou, J. Luo, as it appears in Acta Materialia, 2017, 130, 329. The dissertation author was the primary investigator and author of this paper.

Chapter 3, in part, is a reprint of the material "Flash Sintering Activated by Bulk Phase and Grain Boundary Complexion Transformations", Y. Zhang, J. Nie, and Jian Luo, in preparation for publication. Part of the AZO experiments was carried out by Dr. Yuanyao Zhang. The dissertation author was the primary investigator and author of this paper.

Chapter 4, in part, in part, is a reprint of the material "Water-assisted flash sintering: Flashing ZnO at room temperature to achieve ~ 98% density in seconds", J. Nie, Y. Zhang, J.M. Chan, R. Huang, and J. Luo, as it appears in Scripta Materialia, 2018, 142, 79. Part of the sample preparation was carried out by Dr. Yuanyao Zhang, Dr. Rongxia Huang. Part of the electrode deposition was carried out by Jonathan M. Chan. The dissertation author was the primary investigator and author of this paper.

Chapter 5, in part, is a reprint of the material "Two-Step Flash Sintering of ZnO: Fast Densification with Suppressed Grain Growth", J. Nie, Y. Zhang, J.M. Chan, S. Jiang, R. Huang, J. Luo, as it appears in Scripta Materialia, 2017, 141, 6. Part of the sample preparation was carried out by Dr. Yuanyao Zhang, Sicong

Jiang, and Dr. Rongxia Huang. Part of the electrode deposition was carried out by Jonathan M. Chan. The dissertation author was the primary investigator and author of this paper.

Chapter 6, in part, is a reprint of manuscript “Electric Field Effect on Grain Growth and Grain Boundary Complexion” J. Nie, and J. Luo, in preparation. The dissertation author was the primary investigator and author of this paper.

VITA

2014	Bachelor of Science	Tsinghua University, China
2016	Master of Science	University of California San Diego, USA
2019	Doctor of Philosophy	University of California San Diego, USA

PUBLICATIONS

1. H. Leng, **J. Nie**, J. Luo, “Combining cold sintering and Bi_2O_3-Activated liquid-phase sintering to fabricate high-conductivity Mg-doped NASICON at reduced temperatures”, Journal of Materiomics, 2019, 5, 237.

2. **J. Nie**, Y. Zhang, J.M. Chan, R. Huang, J. Luo, “Water-assisted flash sintering: Flashing ZnO at room temperature to achieve ~ 98% density in seconds”, Scripta Materialia, 2018, 142, 79.

3. H. Leng, J. Huang, **J. Nie**, J. Luo, “Cold sintering and ionic conductivities of $Na_{3.256}Mg_{0.128}Zr_{1.872}Si_2PO_{12}$ solid electrolytes”, Journal of Power Sources, 2018, 391, 170.

4. **J. Nie**, Y. Zhang, J.M. Chan, S. Jiang, R. Huang, J. Luo, “Two-step flash sintering of ZnO: Fast densification with suppressed grain growth”, Scripta Materialia, 2017, 141, 6.

5. Y. Zhang, **J. Nie**, J.M. Chan, J. Luo, “Probing the densification mechanisms during flash sintering of ZnO”, Acta Materialia, 2017, 125, 465.

6. **J. Nie**, J.M. Chan, M. Qin, N. Zhou, J. Luo, “Liquid-like grain boundary

complexion and sub-eutectic activated sintering in CuO-doped TiO_2", Acta Materialia, 2017, 130, 329.

7. Y. Zhang, **J. Nie**, J. Luo, "Effects of phase and doping on flash sintering of TiO_2", Journal of the Ceramic Society of Japan, 2016, 124, 296.

8. **J. Nie**, J. Luo, "Electric Field Effect on Grain Growth and Grain Boundary Complexion Transformations", (in preparation).

9. Y. Zhang, **J. Nie**, J. Luo, "Flash Sintering Activated by Bulk Phase and Grain Boundary Complexion Transformations", (in preparation).

ABSTRACT OF THE DISSERTATION

Solid-state Activated Sintering of TiO_2 and Electric Field Assisted Sintering of ZnO based Materials

by

Jiuyuan Nie

Doctor of Philosophy in Chemical Engineering

University of California San Diego, 2019

Professor Jian Luo, Chair

Solid-state activated sintering of TiO_2-CuO system was systematically studied to reveal the effects of grain boundary structures on low temperature densification. Specifically, the eutectic temperature and composition of the TiO_2-CuO system were carefully measured to be 1010 ± 10 °C and 83CuO:17TiO_2, respectively. Subsequently, a TiO_2-CuO phase diagram was computed. Activated (enhanced) sintering of TiO_2 with the addition of CuO occurring at >300 °C below

the eutectic temperature was observed. High resolution transmission electron microscopy (HRTEM) characterization of water-quenched specimens revealed the formation of nanometer-thick, liquid-like, intergranular films (IGFs), a type of grain boundary (GB) complexion, concurrently with accelerated densification and well below the bulk eutectic temperature. Consequently, activated sintering is explained from the enhanced mass transport in this premelting-like complexion. An interfacial thermodynamic model was used to quantitatively explain and justify the stabilization of liquid-like IGFs below the eutectic temperature and the temperature-dependent IGF thicknesses. A GB λ diagram was computed, for the first time for a ceramic system, to represent the thermodynamic tendency for general grain boundaries to disorder.

Activated flash sintering of ZnO through a bulk phase transformation or a GB complexion transition was investigated. Specifically, in undoped and Al_2O_3-doped ZnO, the flash sintering is activated by natural thermal runways that can be quantitively predicted. In contrast, a bulk eutectic reaction and the associated formation of premelting-like IGFs in Bi_2O_3-doped ZnO can lead to a nonlinear rise in the specimen conductivity (above the Arrhenius extrapolation) to trigger flash sintering prior to the occurrence of the predicted natural thermal runaway. This work uncovers the roles of the bulk phase and interfacial (phase-like) complexion transformations in initiating flash sintering. Beyond high temperature interfacial liquids, water was used as an example of low temperature, transient, interfacial liquid to activate flash sintering at room temperature. ZnO powder pellets was water-assisted flash sintered (WAFS) to achieve ~ 98% of the theoretical density

in 30 s without any external furnace heating. The specimen conductivity can be increased by > 10,000 times via absorbing water vapor to enable the room-temperature flash. The initial electric field must be higher than a critical threshold to lead to densification, suggesting bifurcation in kinetic pathways.

Another method called two-step flash sintering (TSFS) was proposed as a new ceramic fabrication method to achieve fast densification with suppressed grain growth. Using ZnO as an examplar, ~ 96.5% of theoretical density was achieved using TSFS with a grain size of ~ 370 nm, representing a > 3 times reduction of the grain size in comparison with conventional flash sintering. TSFS achieved this result in a few minutes, > 200 times faster than that needed for conventional two-step sintering to obtain comparable results.

Lastly, the effect of electric field on grain growth and grain boundary structure was studied in the presence of ionic grain boundary liquids at high temperatures. Using Bi_2O_3-doped ZnO as a model system, this study reveals the electrochemical polarization of ionic defects driven by an external electric field and current. A mixed conducting model was developed to explain the asymmetric grain growth of sandwiched single crystal, abnormal grain growth near the cathode, as well as the pore formations. The ionic blocking, electric conducting single crystal decouples the effect of electric potential and electrochemical potential on grain growth. It is assumed that electric field and current polarized ionic defects and thereafter modified local space charges. Grain boundary complexion transitions were also observed after annealing under electric field and current.

Chapter 1. Introduction

1.1. Sintering

1.1.1. Brief Overview

Sintering, a term developed by archeologists in the late 18th century, originally refers to the agglomeration and hardening of mineral particles. The definition was then significantly diversified and generalized in the modern era to refer the thermal treatment for bonding particles into a predominantly solid structure. Ancient sintered objects in human history date back to 24000 B.C. according to archeological findings. However, human history of controlling sintering process for manufacturing is only a few hundred years. And the archival literature history of pursuing the science behind sintering is less than 200 years.

There are many variations of sintering technics. Fig. 1.1 is a taxonomy of common sintering technologies from literatures [1]. Many parameters involved in modern sintering practices. For example, pressures ranging from MPa to GPa are used in sintering techniques include hot pressing, spark plasma sintering, and hot isostatic pressing in addition to heating; liquid phase can be used to improve the sintering rate, which is very common in the industry. However, it is worth noting that as the development of sintering technologies, the complete classification of sintering is difficult, especially for processes involving multiple controlled parameters.

1.1.2. Theories

Qualitative and quantitative sintering theories were developed in 1940s. Even though the development of sintering theories was far behind the commercialization of modern sintered products, they drive the success of new technologies and new products.

The sintering of single phase powder by solid-state diffusion or multi-phase powder mixtures by liquid phase are generally described in three stages. As shown in Fig. 1.2 [2], starting with a porous green body, which is usually prepared by mechanical pressing particles in a mold, a phenomenon called “neck formation” happens in the initial stage of sintering. Concave necks will form between particles. Relative density will slightly increase, but the specimen is still very porous. In the intermediate stage, there are neck evolution and grain boundary evolutions. Major densification occurs during this stage, but the pores are still open networks. In the final stage, open pores are isolated to form closed pores between grains, and part of them are removed after completion of sintering. Thermodynamically, the driving force of sintering is the reduction of total interfacial energy.

Grain growth is another important phenomenon during densification as well as in fully dense polycrystalline materials. If the relative grain sizes have a simple and invariable distribution, it is characterized as normal grain growth. However, if there are exceptionally large grains exist, forming a bimodal grain size distribution, it is referred as abnormal grain growth. During the sintering of a powder compact, the increase of density and grain size happen simultaneously [1]. Thus, when studying the grain growth during sintering, the interaction between densification

and grain growth must be considered. Other aspects that should be considered include impurities, secondary phases, atmosphere, *etc.*

1.1.3. Solid-State Activated Sintering

Solid-state activated sintering is a process that can dramatically improve the densification of metal or ceramic green bodies at temperatures that no stable bulk liquid phase forms by adding a small amount of solid phase sintering aids [3]. Some famous examples are Ni-doped W and Mo [4-6] and Bi_2O_3-doped ZnO [7]. The activated sintering could initiate below 60% of the corresponding bulk eutectic temperatures.

The solid-state activated sintering has been studied for over 5 decades [8-14]. Recent developments in high resolution transmission electron microscopy (TEM) and scanning transmission electron microscopy (STEM) revealed the existence of stable intergranular films (IGFs) below the bulk eutectic temperatures in a wide range of ceramics and metals [15-17], suggesting enhanced mass transportation through these nanometer-thick, quasi-liquid films in solid-state activated systems.

A phenomenological interfacial thermodynamic model, Grain Boundary λ Model, was proposed to predict the stability of nanometer thick liquid-like intergranular films [18, 19]. Chapter 2 is an example of extending the model from metallic systems to ceramic systems.

1.1.4. Electric Field Assisted Sintering

Electric Field adds another flexibility to materials sintering practices. The early application of DC current assisted sintering includes consolidation of filaments by W.L. Voelker in 1898, resistance sintering developed by Sauerwald in 1922, sintering of refractory metals by Taylor in 1933, *etc.* [20]. However, the idea of using electric field on sintering was not widely spread to other materials at that time. Later, formulation of this technology and idea was significantly accelerated by the development of a technology called spark plasma sintering (SPS) in 1950s, as well as its commercialization in the 1990s. In the SPS technology, a pulsed DC current is used to heat up a graphite or tungsten carbide die in vacuum or an inert gas. In the meantime, a pressure is applied on the materials [21]. SPS has the advantage of sintering at lower temperature and in a shorter time than the conventional sintering method(s). There is a significant number of publications indicating that SPS can be used to produce nanocrystalline materials [22-25]. There are also findings showings that SPS can improve materials mechanical [26, 27], optical [24, 28], or ferroelectrical properties [29].

It is worth noting that, in most of the conventional SPS process, most of the electric current passes through the graphite or tungsten carbide die rather than the specimens. In 2010, Raj and his co-workers developed the Flash Sintering technology [30], which passes current through the specimens directly. They have successfully densified 3 mol. % yttria-stabilized zirconia (3YSZ) in a few seconds at a furnace temperature of ~ 850 °C, which was a few hundred degrees below the conventional sintering temperature. Fig. 1.3 represents the flash sintering

phenomenon and its difference with traditional field assisted sintering technology (FAST), which enhances densification moderately at low external electric fields.

In a typical Flash Sintering setup, a constant, high electric field is applied on a green specimen while heating it up in a furnace. Given an electric field that is high enough, an electrical and thermal instability of the specimen occurs, leading to a fast increase of current density as well as specimen temperature. After reaching a pre-set current limit, the power supply is switched to the constant-current mode. The specimen is sintered after holding it at the current limit for a very short time. Green specimens can reach almost fully dense in a few seconds using flash sintering.

Many materials have been successfully sintered using the Flash Sintering technology since its invention. For example, 8YSZ [31], $CoMnO_4$ [32], $SrTiO_3$ [33], TiO_2 [34], GDC [35], MgO-doped Al_2O_3 [36], SiC-Al_2O_3-Y_2O_5 [37], *etc*. Independent studies carried out at University of California San Diego [38], Oxford University [39], and University of Pennsylvania [40] proposed thermal runaway models to explain the onset of flash sintering. Electrical thermal runaway has been proposed and tested to be the major cause of the onset of flash sintering in many materials. On the other hand, there are other proposed mechanisms. For example, an avalanche nucleation of Frenkel pairs driven by the high electric field will initiate the flash sintering. This proposed mechanism remains controversial and needs further study in the future [41, 42].

To understand the fast densification mechanism during flash sintering, Zhang and his co-workers investigated the densification mechanism during flash

sintering [43]. Their study revealed the contribution of the high heating rate on the ultra-fast densification rate. Other mechanisms have also been proposed by researchers to explain the densification under electric fields. For example, Kim, Kang, and Chen proposed an electro-sintering mechanism that the surface diffusion of cations at the pores enhances the densifications [44].

The effect of electric field and current other than Joule heating during flash sintering is elaborated in Section 1.3.

1.2. Grain Boundary Complexion

Extending the Gibbs definition of bulk phases, “grain boundary complexion” is a term designated to describe the features of grain boundaries that is in thermodynamic equilibrium with its abutting phase(s) [45].

In 2007, Dillon, Hammer and their co-workers systematically characterized six grain boundary complexions (Fig. 1.4) in Al_2O_3 system based on their classification [46]: Complexion I is a Langmuir-McLean sub-monolayer adsorption with scattered dopant cations; Complexion II is “clean” grain boundary; Complexion III is a bilayer adsorption of ~0.35 nm thick; Complexion IV is a multi-layer adsorption of ~ 0.6 nm thick; Complexion V is an intergranular film with an equilibrium thickness of 1 – 2 nm; and Complexion VI is a wetting film.

The observation of various complexions beyond intergranular films further emphasized the complexity of grain boundaries. And, understanding the grain boundary complexions not only helps controlling the microstructural evolutions, but also explains and predicts materials mechanical, electrical, thermal, and chemical

properties [17, 18]. Thus, the new findings urge researchers to pursue a long-range scientific goal of developing grain boundary diagrams. Recently, using a lattice model and CALPHAD data, Zhou and co-workers successfully calculated and validated a grain boundary complexion diagram for Bi-doped Ni [47].

1.3. Electric Field Effects on Microstructures

In addition to the Joule heating effect, there are many evidences showing that the electric field/current also affects the microstructure evolution during field assisted sintering. For example, anomalous lattice expansion was observed in 8YSZ [48] and ceria [49] using in-situ diffractometry; reversible cubic-like phase appeared in 3YSZ under electric field and current [50]; abnormal grains were observed at the cathode side in flash sintered 3YSZ [51]; enhanced grain growth was observed at the anode side in flash sintered ZnO in air [38], but disappeared in flash sintered ZnO in reduced atmosphere [52].

Moreover, there are research on the asymmetric microstructure evolution of ceramic systems under electric field beyond the studies of sintering technologies. As one of the earliest studies on the effects of electric field on solid-state oxides processing, Mackenzie and co-workers demonstrated the improved cation mobility and their relationship with the direction of the external field in 1979 [53, 54]. Similar asymmetric grain growth in the presence of external electric field/current has also been observed by Kim and colleagues in pristine or doped Al_2O_3 systems in 2001 and 2003 [55, 56]. Recently, Hoffman and his coworkers observed the asymmetric grain growth of single crystals in $SrTiO_3$ [57], *etc.* In the fields of solid oxide fuel

cells (SOFCs), a great number of research has been conducted to understand the structural and electrical evolution of solid electrolyte during degradations, where materials typically experiences DC electric field, high temperature, and long testing/operating times [58-61].

Some mechanisms have been proposed to explain various structure changes of materials under electric fields. Some examples are shown here. (a) Jeong and co-workers proposed that electric field modified the activation energy of cations to jump across the grain boundaries, resulted the enhanced or retarded grain growth of Al_2O_3 depending on the direction of applied electric fields [62]. Similar explanations were also applied to TiO_2-doped and Li_2O-doped Al_2O_3, both of which modified the grain boundary charges compare with undoped Al_2O_3 according to the authors [63]. (b) In the presence of a liquid phase during the annealing of Nb-doped $BaTiO_3$, Jin and co-workers proposed that external electric fields modified the local bulk defect concentrations, which affected the grain boundary potentials. The liquid phase wetting was further affected by the changes in grain boundary potentials, thus resulted different grain growth behaviors at cathode and anode [64]. (c) Rheinheimer and co-workers proposed that the enhanced grain growth in $SrTiO_3$ was a result of defect redistribution across the sample through grain boundaries by comparing with grain growth data in literature [57, 65]. (d) Dong and his co-workers modelled the defect redistribution and the electrochemical reduction in YSZ under external electric field. Enhanced local cation kinetics were proposed to explain the asymmetric grain growth and pore

migrations [51, 58, 66]. The major electric field effects can vary in different materials depending on their microstructures and conducting mechanisms.

1.4. Motivation and Overview

On one hand, the research of flash sintering opens opportunities of developing new sintering technologies, especially when combined with other advanced sintering methods. On the other hand, the intriguing observations and fast development of field assisted sintering technologies urge for explorations of the electric field and current effects on bulk phases as well as the grain boundary complexions to guide the development of novel sintering technologies as a long-term scientific goal.

In **Chapter 2**, a solid-state activated sintering system, TiO_2-CuO was systematically studied to reveal the effects of grain boundary structures on low temperature densification. Specifically, the eutectic temperature and composition of the TiO_2-CuO system were carefully measured to be 1010 ± 10 °C and 83CuO:17TiO_2, respectively. Subsequently, a TiO_2-CuO phase diagram was computed, representing a correction and major improvement from the phase diagram available in literature. Dilatometry measurements and isothermal sintering experiments unequivocally demonstrated the activated (enhanced) sintering of TiO_2 with the addition of CuO, occurring at as low as >300 °C below the eutectic temperature. High resolution transmission electron microscopy (HRTEM) characterization of water-quenched specimens revealed the formation of nanometer-thick, liquid-like, intergranular films (IGFs), a type of grain boundary

(GB) complexion described in section 1.2, concurrently with accelerated densification and well below the bulk eutectic temperature. Consequently, activated sintering is explained from the enhanced mass transport in this premelting-like complexion. An interfacial thermodynamic model was used to quantitatively explain and justify the stabilization of liquid-like IGFs below the eutectic temperature and the temperature-dependent IGF thicknesses measured by HRTEM. A GB λ diagram was computed, for the first time for a ceramic system, to represent the thermodynamic tendency for general GBs in CuO-doped TiO2 to disorder.

In **Chapter 3**, possibilities to activate flash sintering were investigated: bulk phase transformation and/or a grain boundary (phase-like) complexion transition can cause an abrupt rise in the specimen conductivity to jump start flash sintering (prior to the occurrence of a natural thermal runaway). In undoped and Al_2O_3-doped ZnO, the flash sintering is activated by natural thermal runways that can be quantitively predicted from an Arrhenius extrapolation of low-temperature specimen conductivity. In contrast, a bulk eutectic reaction and the associated formation of premelting-like intergranular films in Bi_2O_3-doped ZnO can lead to a nonlinear rise in the specimen conductivity (above the Arrhenius extrapolation) to trigger flash sintering prior to the occurrence of the predicted natural thermal runaway. Consistent with and further supporting the proposed theory, a natural thermal runaway can still take place in Bi_2O_3-doped ZnO before the occurrence of the interfacial and bulk transformation if the initial electric field is increased to a sufficiently high level (800 V/cm in this case). This work uncovers the roles of the

bulk phase and interfacial (phase-like) complexion transformations in initiating flash sintering, thereby suggesting a new direction to understand and tailor the flash sintering process. The observation of ultra-fast field-induced migration of aliovalent cations during the flash sintering of Al_2O_3-doped ZnO is also reported.

In **Chapter 4**, water, a low temperature liquid phase in the green body, was used to trigger flash sintering of ZnO powder pellets at room temperature to achieve ~ 98% of the theoretical density in 30 s without any external furnace heating. The specimen conductivity can be increased by > 10,000 times via absorbing water vapor to enable the room-temperature flash. The initial electric field must be higher than a critical threshold to lead to densification, suggesting bifurcation in kinetic pathways. This new cost and energy saving water-assisted flash sintering (WAFS) technology can potentially be applied to consolidate other ceramic materials.

In **Chapter 5**, two-step flash sintering (TSFS) was proposed as a new ceramic fabrication method to achieve fast densification with suppressed grain growth. Using ZnO as an examplar, ~ 96.5% of theoretical density was achieved using TSFS with a grain size of ~ 370 nm, representing a > 3 times reduction of the grain size in comparison with conventional (one-step) flash sintering. Moreover, TSFS achieved this result in a few minutes, > 200 times faster than that needed for conventional two-step sintering to obtain comparable results, thereby representing an opportunity for significant energy and cost savings.

In **Chapter 6**, The effect of electric field on grain growth and grain boundary structure was studied in the presence of ionic grain boundary liquids at high

temperatures. Using Bi_2O_3-doped ZnO as a model system, this study reveals the electrochemical polarization of ionic defects driven by an external electric field and current in a series of self-comparable polycrystalline – single crystal – polycrystalline sandwich specimens. A mixed conducting model was developed to explain the asymmetric grain growth of the single crystal, abnormal grain growth near the cathode, as well as the pore formations. Additionally, the ionic blocking, electric conducting single crystal decouples the effect of electric potential and electrochemical potential on grain growth. It is assumed that electric field and current polarized ionic defects and thereafter modified local space charges. Grain boundary complexion transitions were also observed after annealing under electric field and current. Grain boundaries were metallic-like and highly ordered at electrochemically reduced locations but maintained disordered in oxidized locations. In addition, electric field induced textures of the abnormal grains were observed.

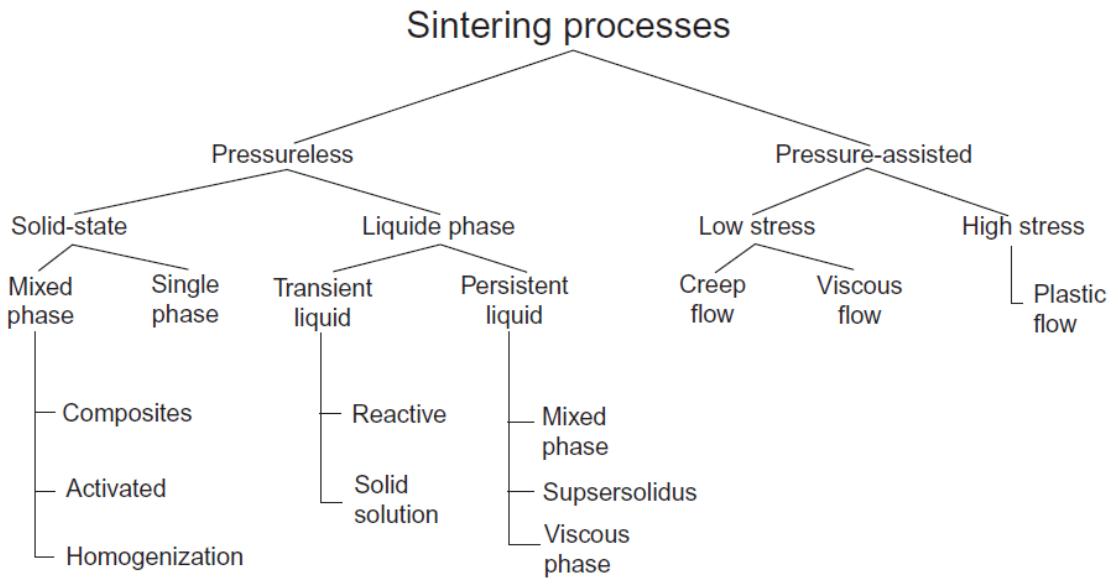

Figure 1.1 The taxonomy of sintering, showing process differentiation by various branches, starting with the application of pressure-assisted versus pressureless sintering [1].

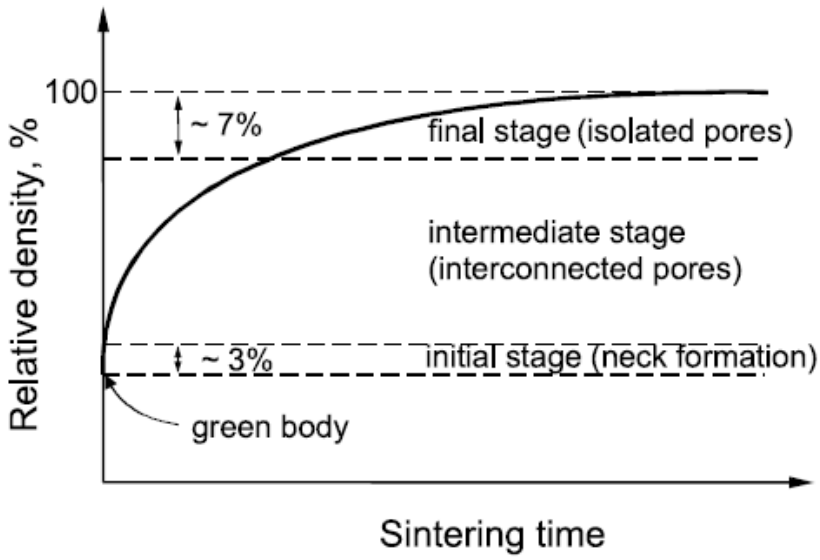

Figure 1.2 Schematics of densification curve of a powder compact and the three stages of sintering [2].

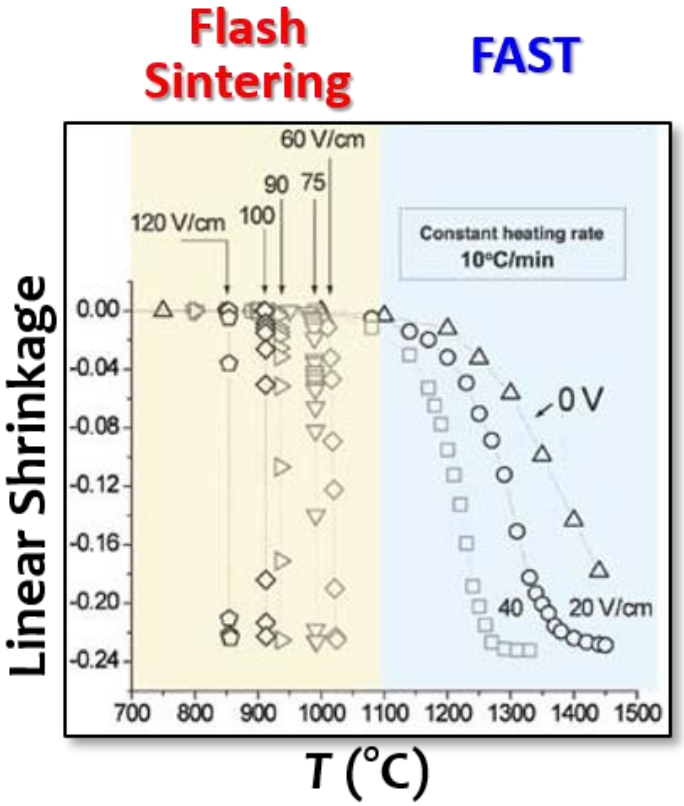

Figure 1.3 DC electrical fields enhance the rate of sintering in yttria-stabilized zirconia (3YSZ). An instability occurs when the field is greater than a threshold value, leading to sintering in just a few seconds at unusually low furnace temperatures. This kind of sintering process is called flash sintering [21].

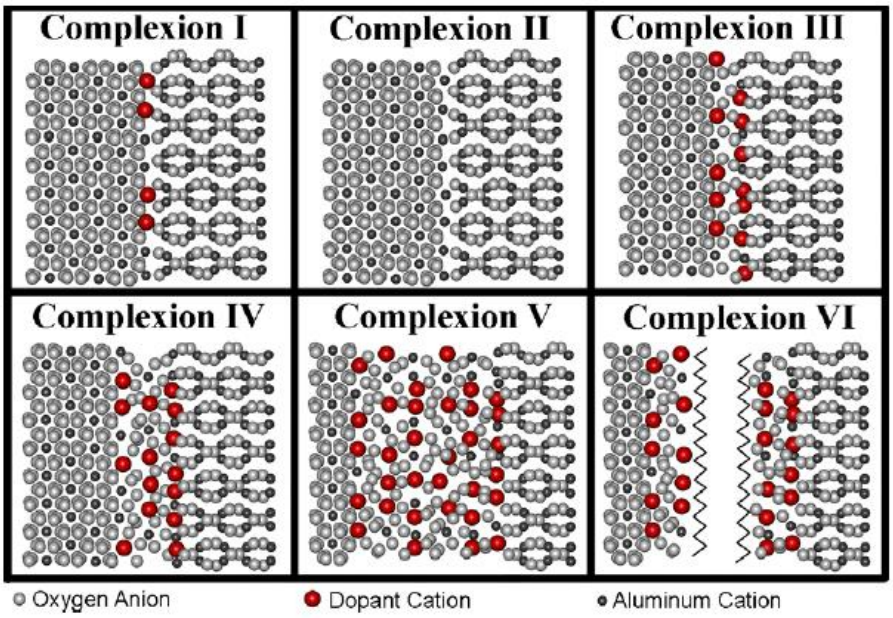

Figure 1.4 Schematic of the six different grain boundary complexions based on HRTEM images in Al_2O_3 systems: I, submonolayer adsorption; II, the ‘‘clean’’ grain boundary; III, bilayer adsorption; IV, multi-layer adsorption; V, an equilibrium thickness amorphous intergranular film; and VI, a wetting film [46].

References

[1] R.M. German, Sintering: From Empirical Observations to Scientific Principles, Sintering: from Empirical Observations to Scientific Principles (2014) 1-536.

[2] S.-J.L. Kang, Sintering: densification, grain growth and microstructure, Elsevier2004.

[3] J. Luo, Developing Interfacial Phase Diagrams for Applications in Activated Sintering and Beyond: Current Status and Future Directions, Journal of the American Ceramic Society 95(8) (2012) 2358-2371.

[4] X. Shi, J. Luo, Grain boundary wetting and prewetting in Ni-doped Mo, Appl. Phys. Lett. 94(25) (2009) 251908.

[5] V.K. Gupta, D.H. Yoon, H.M. Meyer III, J. Luo, Thin Intergranular Films and Solid-State Activated Sintering in Nickel-Doped Tungsten, Acta Mater. 55 (2007) 3131-3142.

[6] J. Luo, V.K. Gupta, D.H. Yoon, H.M. Meyer, Segregation-Induced Grain Boundary Premelting in Nickel-doped Tungsten, Appl. Phys. Lett. 87 (2005) 231902.

[7] J. Luo, H.F. Wang, Y.M. Chiang, Origin of solid-state activated sintering in Bi2O3-doped ZnO, Journal of the American Ceramic Society 82(4) (1999) 916-920.

[8] H.W. Hayden, J.H. Brophy, THE ACTIVATED SINTERING OF TUNGSTEN WITH GROUP-VIII ELEMENTS, Journal of the Electrochemical Society 110(7) (1963) 805-810.

[9] R. Coble, R. Cannon, Current paradigms in powder processing, Processing of crystalline ceramics, Springer1978, pp. 151-170.

[10] R.M. German, DIFFUSIONAL ACTIVATED SINTERING DENSIFICATION, MICROSTRUCTURE AND MECHANICAL-PROPERTIES, International Journal of Powder Metallurgy 19(4) (1983) 277-&.

[11] J.L. Johnson, R.M. German, Theoretical modeling of densification during activated solid-state sintering, Metallurgical and Materials Transactions a-Physical Metallurgy and Materials Science 27(2) (1996) 441-450.

[12] K.S. Hwang, H.S. Huang, Identification of the segregation layer and its effects on the activated sintering and ductility of Ni-doped molybdenum, Acta Materialia 51(13) (2003) 3915-3926.

[13] E.C. Skaar, Activated sintering in the calcium fluoride, sodium fluoride system, 1977.

[14] T.E. Oskina, K.B. Zaborenko, A.G. Krasnoperova, I.G. Melnikova, ACTIVATED SINTERING OF TIN DIOXIDE, Glass and Ceramics 34(7-8) (1977) 457-460.

[15] D.R. Clarke, ON THE EQUILIBRIUM THICKNESS OF INTERGRANULAR GLASS PHASES IN CERAMIC MATERIALS, Journal of the American Ceramic Society 70(1) (1987) 15-22.

[16] V.K. Gupta, D.H. Yoon, H.M. Meyer, J. Luo, Thin intergranular films and solid-state activated sintering in nickel-doped tungsten, Acta Materialia 55(9) (2007) 3131-3142.

[17] J. Luo, Stabilization of nanoscale quasi-liquid interfacial films in inorganic materials: A review and critical assessment, Critical Reviews in Solid State and Materials Sciences 32(1-2) (2007) 67-109.

[18] J. Luo, Liquid-like interface complexion: From activated sintering to grain boundary diagrams, Current Opinion in Solid State & Materials Science 12(5-6) (2008) 81-88.

[19] N. Zhou, Thermodynamic Modeling of Grain Boundaries Complexions and Developing Grain Boundary Complexion Diagrams for Multicomponent Metallic Systems, UC San Diego, 2017.

[20] A. EUGENE, D. OLEVSKY, V. DINA, FIELD-ASSISTED SINTERING: Science and Applications, SPRINGER2019.

[21] Z.A. Munir, D.V. Quach, M. Ohyanagi, Electric current activation of sintering: a review of the pulsed electric current sintering process, Journal of the American Ceramic Society 94(1) (2011) 1-19.

[22] D.V. Dudina, A.K. Mukherjee, Reactive spark plasma sintering: successes and challenges of nanomaterial synthesis, Journal of Nanomaterials 2013 (2013) 5.

[23] N. Saheb, Z. Iqbal, A. Khalil, A.S. Hakeem, N. Al Aqeeli, T. Laoui, A. Al-Qutub, R. Kirchner, Spark plasma sintering of metals and metal matrix nanocomposites: a review, Journal of Nanomaterials 2012 (2012) 18.

[24] M. Eriksson, Y. Liu, J. Hu, L. Gao, M. Nygren, Z. Shen, Transparent hydroxyapatite ceramics with nanograin structure prepared by high pressure spark plasma sintering at the minimized sintering temperature, Journal of the European Ceramic Society 31(9) (2011) 1533-1540.

[25] B.M. Moshtaghioun, A.L. Ortiz, D. Gómez-García, A. Domínguez-Rodríguez, Densification of B_4C nanopowder with nanograin retention by spark-plasma sintering, Journal of the European Ceramic Society 35(6) (2015) 1991-1998.

[26] B. Srinivasarao, K. Oh-Ishi, T. Ohkubo, K. Hono, Bimodally grained high-strength Fe fabricated by mechanical alloying and spark plasma sintering, Acta Materialia 57(11) (2009) 3277-3286.

[27] X. Deng, X. Wang, H. Wen, A. Kang, Z. Gui, L. Li, Phase transitions in nanocrystalline barium titanate ceramics prepared by spark plasma sintering, Journal of the American Ceramic Society 89(3) (2006) 1059-1064.

[28] B.-N. Kim, K. Hiraga, K. Morita, H. Yoshida, Spark plasma sintering of transparent alumina, Scripta Materialia 57(7) (2007) 607-610.

[29] J.F. Li, K. Wang, B.P. Zhang, L.M. Zhang, Ferroelectric and piezoelectric properties of fine-grained $Na_{0.5}K_{0.5}NbO_3$ lead-free piezoelectric ceramics prepared by spark plasma sintering, Journal of the American Ceramic Society 89(2) (2006) 706-709.

[30] M. Cologna, B. Rashkova, R. Raj, Flash Sintering of Nanograin Zirconia in < 5 s at 850 °C, Journal of the American Ceramic Society 93(11) (2010) 3556-3559.

[31] M. Cologna, A.L.G. Prette, R. Raj, Flash-Sintering of Cubic Yttria-Stabilized Zirconia at 750 °C for Possible Use in SOFC Manufacturing, Journal of the American Ceramic Society 94(2) (2011) 316-319.

[32] A. Gaur, V.M. Sglavo, Flash-sintering of MnCo2O4 and its relation to phase stability, Journal of the European Ceramic Society 34(10) (2014) 2391-2400.

[33] A. Karakuscu, M. Cologna, D. Yarotski, J. Won, J.S. Francis, R. Raj, B.P. Uberuaga, Defect Structure of Flash-Sintered Strontium Titanate, Journal of the American Ceramic Society 95(8) (2012) 2531-2536.

[34] Y.Y. Zhang, J.Y. Nie, J. Luo, Effects of phase and doping on flash sintering of TiO_2, Journal of the Ceramic Society of Japan 124(4) (2016) 296-300.

[35] X.M. Hao, Y.J. Liu, Z.H. Wang, J.S. Qiao, K.N. Sun, A novel sintering method to obtain fully dense gadolinia doped ceria by applying a direct current, Journal of Power Sources 210 (2012) 86-91.

[36] M. Cologna, J.S. Francis, R. Raj, Field assisted and flash sintering of alumina and its relationship to conductivity and MgO-doping, Journal of the European Ceramic Society 31(15) (2011) 2827-2837.

[37] E. Zapata-Solvas, S. Bonilla, P.R. Wilshaw, R.I. Todd, Preliminary investigation of flash sintering of SiC, Journal of the European Ceramic Society 33(13-14) (2013) 2811-2816.

[38] Y.Y. Zhang, J.I. Jung, J. Luo, Thermal runaway, flash sintering and asymmetrical microstructural development of ZnO and ZnO-Bi_2O_3 under direct currents, Acta Materialia 94 (2015) 87-100.

[39] R. Todd, E. Zapata-Solvas, R. Bonilla, T. Sneddon, P. Wilshaw, Electrical characteristics of flash sintering: thermal runaway of Joule heating, Journal of the European Ceramic Society 35(6) (2015) 1865-1877.

[40] Y.H. Dong, I.W. Chen, Onset Criterion for Flash Sintering, Journal of the American Ceramic Society 98(12) (2015) 3624-3627.

[41] M. Jongmanns, R. Raj, D. Wolf, Generation of Frenkel defects above the Debye temperature by proliferation of phonons near the Brillouin zone edge, New Journal of Physics 20(9) (2018) 093013.

[42] M. Schie, S. Menzel, J. Robertson, R. Waser, R.A. De Souza, Field-enhanced route to generating anti-Frenkel pairs in HfO_2, Physical review materials 2(3) (2018) 035002.

[43] Y.Y. Zhang, J.Y. Nie, J.M. Chan, J. Luo, Probing the densification mechanisms during flash sintering of ZnO, Acta Materialia 125 (2017) 465-475.

[44] S.W. Kim, S.J.L. Kang, I.W. Chen, Electro-sintering of yttria-stabilized cubic zirconia, Journal of the American Ceramic Society 96(5) (2013) 1398-1406.

[45] P.R. Cantwell, M. Tang, S.J. Dillon, J. Luo, G.S. Rohrer, M.P. Harmer, Grain boundary complexions, Acta Materialia 62 (2014) 1-48.

[46] S.J. Dillon, M. Tang, W.C. Carter, M.P. Harmer, Complexion: a new concept for kinetic engineering in materials science, Acta Materialia 55(18) (2007) 6208-6218.

[47] N.X. Zhou, Z.Y. Yu, Y.Y. Zhang, M.P. Harmer, J. Luo, Calculation and validation of a grain boundary complexion diagram for Bi-doped Ni, Scripta Materialia 130 (2017) 165-169.

[48] E.K. Akdogan, I. Savkliyildiz, H. Bicer, W. Paxton, F. Toksoy, Z. Zhong, T. Tsakalakos, Anomalous lattice expansion in yttria stabilized zirconia under simultaneous applied electric and thermal fields: A time-resolved in situ energy dispersive x-ray diffractometry study with an ultrahigh energy synchrotron probe, Journal of Applied Physics 113(23) (2013).

[49] S.K. Jha, H. Charalambous, H. Wang, X.L. Phuah, C. Mead, J. Okasinski, H. Wang, T. Tsakalakos, In-situ observation of oxygen mobility and abnormal lattice expansion in ceria during flash sintering, Ceramics International 44(13) (2018) 15362-15369.

[50] J.M. Lebrun, T.G. Morrissey, J.S.C. Francis, K.C. Seymour, W.M. Kriven, R. Raj, Emergence and Extinction of a New Phase During On-Off Experiments Related to Flash Sintering of 3YSZ, Journal of the American Ceramic Society 98(5) (2015) 1493-1497.

[51] Y.H. Dong, H.R. Wang, I.W. Chen, Electrical and hydrogen reduction enhances kinetics in doped zirconia and ceria: I. grain growth study, Journal of the American Ceramic Society 100(3) (2017) 876-886.

[52] Y.Y. Zhang, J. Luo, Promoting the flash sintering of ZnO in reduced atmospheres to achieve nearly full densities at furnace temperatures of < 120 °C, Scripta Materialia 106 (2015) 26-29.

[53] K.J.D. Mackenzie, R.K. Banerjee, M.R. Kasaai, EFFECT OF ELECTRIC-FIELDS ON SOLID-STATE REACTIONS BETWEEN OXIDES .1. REACTION BETWEEN CALCIUM AND ALUMINUM-OXIDES, Journal of Materials Science 14(2) (1979) 333-338.

[54] K.J.D. Mackenzie, M.J. Ryan, EFFECT OF ELECTRIC-FIELDS ON SOLID-STATE REACTIONS BETWEEN OXIDES. 3. INTER-DIFFUSION IN POLYCRYSTALLINE MAGNESIUM AND ALUMINUM-OXIDE PELLETS, Journal of Materials Science 16(3) (1981) 579-588.

[55] J.H. Han, D.Y. Kim, Effect of external electric field on the boundary migration of Al_2O_3 ceramics, Japan Inst Metals, Sendai, 2001.

[56] J.I. Choi, J.H. Han, D.Y. Kim, Effect of titania and lithia doping on the boundary migration of alumina under an electric field, Journal of the American Ceramic Society 86(4) (2003) 640-643.

[57] W. Rheinheimer, M. Fulling, M.J. Hoffmann, Grain growth in weak electric fields in strontium titanate: Grain growth acceleration by defect redistribution, Journal of the European Ceramic Society 36(11) (2016) 2773-2780.

[58] A.V. Virkar, J. Nachlas, A.V. Joshi, J. Diamond, Internal precipitation of molecular oxygen and electromechanical failure of zirconia solid electrolytes, Journal of the American Ceramic Society 73(11) (1990) 3382-3390.

[59] Y. Matus, L.C. De Jonghe, X.F. Zhang, S.J. Visco, C.P. Jacobson, Electrolytic damage in zirconia electrolytes, Solid Oxide Fuel Cells Viii (Sofc Viii) 2003(7) (2003) 209-213.

[60] F. Tietz, D. Sebold, A. Brisse, J. Schefold, Degradation phenomena in a solid oxide electrolysis cell after 9000 h of operation, Journal of Power Sources 223 (2013) 129-135.

[61] C. Graves, S.D. Ebbesen, S.H. Jensen, S.B. Simonsen, M.B. Mogensen, Eliminating degradation in solid oxide electrochemical cells by reversible operation, Nature Materials 14(2) (2015) 239-244.

[62] J.W. Jeong, J.H. Han, D.Y. Kim, Effect of electric field on the migration of grain boundaries in alumina, Journal of the American Ceramic Society 83(4) (2000) 915-918.

[63] J.I. Choi, J.H. Han, D.Y. Kim, Effect of titania and lithia doping on the boundary migration of alumina under an electric field, Journal of the American Ceramic Society 86(2) (2003) 347-350.

[64] H.R. Jin, S.H. Yoon, J.H. Lee, N.M. Hwang, D.Y. Kim, J.H. Han, Effect of external electric field on the grain-growth behavior of barium titanate, Journal of the American Ceramic Society 87(9) (2004) 1747-1752.

[65] W. Rheinheimer, J.P. Parras, J.H. Preusker, R.A. De Souza, M.J. Hoffmann, Grain growth in strontium titanate in electric fields: The impact of space-charge on the grain-boundary mobility, Journal of the American Ceramic Society 102(6) (2019) 3779-3790.

[66] Y.H. Dong, I.W. Chen, Oxygen potential transition in mixed conducting oxide electrolyte, Acta Materialia 156 (2018) 399-410.

Chapter 2. Liquid-like grain boundary complexion and sub-eutectic activated sintering in CuO-doped TiO_2

2.1. Introduction

Titania (TiO_2) has excellent electronic and optical properties that enable its applications in photovoltaic, sensing, and a variety of other types of devices (where some levels of low-temperature sintering are often involved) [1-3]. Furthermore, TiO_2 has excellent dielectric properties for possible applications in electronics; however, the high sintering temperatures of pure TiO_2, which are generally in the range of 1200-1400 °C [4], make it incompatible with the low-temperature co-fired technology [5] that requires the sintering temperature to be appreciably lower than the melting temperature of the metal conductors, such as Cu (T_m = 1083 °C) and Ag (T_m = 961 °C) [6]. Thus, researchers have made great efforts to lower the sintering temperature of TiO_2, *e.g.*, via using monodisperse TiO_2 powder [7] or making sol-gel films [8]. A more common and practical method is to add a small amount of sintering aids to lower the sintering temperature [9]. While CuO is perhaps one of the most effective sintering aid for promoting low-temperature densification of TiO_2 [10, 11], its exact underlying mechanisms remain elusive, which motivated this study.

It is well known that CuO doping can reduce the sintering temperatures of TiO_2 to ~850-950 °C, which was generally attributed to a liquid-phase sintering effect in prior studies [10, 12, 13]. However, Lu *et al* reported a computed eutectic temperature of 919 °C for the TiO_2-CuO system [14]. Recently, de la Rubia *et al*

suggested that the eutectic temperature is ~1000 °C via differential scanning calorimetry (DSC) and thermogravimetric (TG) analysis, in conjunction with hot-stage microscopy [15]. These results casted doubt on the previously hypothesized liquid-phase sintering mechanism for CuO-doped TiO_2, since the significant densification appeared to occur well below the eutectic temperature, though what is the exact/real eutectic temperature was still controversial prior to this study.

In this study, we conducted careful experiments to unequivocally showed that the low-temperature densification of CuO-doped TiO_2 is a case of sub-eutectic activated sintering, rather than the commonly believed liquid-phase sintering. First, we measured the eutectic temperature and composition of the CuO-TiO_2 system via calibrating the furnace and characterizing well-quenched specimens. Specifically, we showed that the eutectic reaction takes place between 1000 °C and 1020 °C in air and determined the eutectic composition to be ~ 83CuO:17TiO_2. Subsequently, we showed that enhanced densification can start below 700-800°C, well below the bulk eutectic temperature. Furthermore, we observed the stabilization of nanoscale liquid-like intergranular films (IGFs) well below the bulk eutectic temperature by high resolution transmission electron microscopy (HRTEM) and attributed the sub-eutectic activated sintering in CuO-TiO_2 to the enhanced mass transport in this nanoscale liquid-like complexion (*a.k.a.* 2-D interfacial phase) that is stabilized below the eutectic temperature at grain boundaries (GBs), analogous those reported previously for Bi_2O_3-doped ZnO [16] and Ni-doped W and Mo [17-19].

Furthermore, we have computed a binary phase diagram for the TiO_2-CuO system, which represents a major improvement from (and a correction of) the phase diagram available in literature. Subsequently, a GB λ diagram was also computed to represent the thermodynamic tendency for general GBs in CuO-doped TiO_2 to disorder, for the first time for any ceramic system. We adopted an interfacial thermodynamic model to quantitively explain the stabilization of liquid-like IGFs below the bulk eutectic temperature, and to further justify the temperature-dependence of the IGF thicknesses measured by HRTEM.

2.2. Experiments

To determine the eutectic temperature and composition, rutile-phase TiO_2 (99.9+%, purchased from US research Nanomaterials, Inc.) was mixed with CuO powder (99.999%, purchase from Sigma-Aldrich) in a mortar. The mixed powder was uniaxially compressed to pellets at 450 MPa. The surfaces of the pellets were slightly grinded to remove any contamination from the dies. The pellets were then placed in small sapphire crucibles (> 99.9% purity, purchased from AdValue Technology), annealed isothermally at desired temperatures (with a heating ramping rate of 5 °C/min before reaching the desired isothermal annealing temperature), and water quenched. Quenched samples were then sectioned, grinded, and polished.

Specimens for sintering experiments were made by either a dry mixing or a wet chemistry method. In the dry mixing method, 4 mol. % CuO powder were mixed with rutile-phase TiO_2. In the wet chemistry method, an appropriate amount of

$Cu(NO_3)_2 \cdot 2.5H_2O$ (99.99%, purchased from Sigma-Aldrich) was dissolved in DI water to make an aqueous Cu^{2+} solution. Subsequently, rutile TiO_2 nanopowder was impregnated in the Cu^{2+} solution. The mixtures were then dried in an oven at 85 °C for 12 hours. The dried powders were ground in a mortar for 10 minutes, followed by annealing in air at 500 °C for 1 hour (to decompose $Cu(NO_3)_2$ into CuO, which occurs at ~ 180°C). After annealing, the powders were ground for another 10 minutes. The final powders (made by the either method) were uniaxially pressed at ~200 MPa to make green pellets of 6.35 mm in diameter. The surfaces were slightly grinded to remove contamination from the dies. Green densities of the pellets were measured to be ~40%. Linear shrinkages of compacted pellets were measured by a dilatometer (DIL, NETZSCH Group) up to 1000 °C at a constant heating ramping rate of 5 °C/min in air.

In the second batch of sintering experiments, specimens were isothermally sintered in a muffle furnace (Thermolyne Furnace F6000, Thermo Scientific), for which the temperature profile was carefully calibrated using a second thermocouple before the experiments to ensure the accuracy of temperature controls and measurements (for accurately determining the eutectic temperature). This batch of sintered specimens were quenched in water to preserve the high-temperature GB structures for subsequent HRTEM characterization. The densities of specimens were measured using both the weight/dimension and the Archimedes method.

Microstructures and compositions were characterized by a field-emission, ultra-high-resolution scanning electron microscope (UHR SEM, FEI XL30)

operating at 10 kV, equipped with an Oxford energy-dispersive X-ray spectroscopy (EDS) analyzer. X-ray diffraction (XRD) experiments were conducted using a Rigaku Ultima IV diffractometer (Cu Kα radiation).

Transmission electron microscopy (TEM) samples were prepared using a focused ion beam (FIB, FEI Scios DualBeam). Atomic-level GB structures were characterized by HRTEM using a FEI Titan microscope operating at 300 kV.

2.3. Results

2.3.1. Determination of Eutectic Temperature and Composition

SEM images of CuO + 20 mol. % TiO_2 specimen (that was a near-eutectic composition selected for the initial experiment *vs.* the actual eutectic composition was subsequently measured to be ~ 83CuO:17TiO_2) after annealing at 1020 °C for 0.5 hour are shown in Fig. 2.1; here, a eutectic structure, in which the light-contrast rods were homogeneously embedded in a dark-contrast matrix, can be clearly seen. In contrast, Fig. 2.2 shows the microstructure and elemental mappings of a CuO + 20 mol. % TiO_2 (rutile) specimen after annealed at a slightly lower temperature of 1000 °C for 8 hours, where a similar eutectic structure clearly did not form. The corresponding EDS mappings revealed that the light-contrast phase is copper oxide, while the dark-contrast phase is TiO_2, with no apparent reaction and virtually no mutual (solid) solubilities. In addition to the SEM images, visual inspection of the specimens also clearly showed the specimen melt at 1020 °C but not at 1000 °C. These results (Fig. 2.1 *vs.* Fig. 2.2) undoubtedly suggested that the eutectic temperature of TiO_2-CuO is 1000 $\pm$ 10 °C.

The XRD patterns of the CuO + 20 mol. % TiO_2 specimens quenched from 1000 °C and 1020 °C, respectively, are shown in Fig. 2.3. Only the two equilibrium CuO and rutile TiO_2 phases were detected from specimens that were annealed at 1000 °C for 8 hours and water quenched. The CuO + 20 mol. % TiO_2 specimen annealed at 1020 °C melted (into a nearly-eutectic liquid so that we did not anneal it longer to prevent the spreading of the liquid and minimize its reaction with the Al_2O_3 crucible), the non-equilibrium Cu_2O and Cu_3TiO_4 phases, as well as the sapphire Al_2O_3 impurity phase, were found in the water-quenched specimen (where the crucible was quenched together with the eutectic liquid into the water).

Further quantitative EDS analysis from multiple measurements of the eutectic structures seen in SEM showed the average measured composition corresponded to a cation ratio of Cu: Ti = 4.95 ± 0.11, *i.e.*, the eutectic composition is ~17 mol. % TiO_2 + ~83 mol. % CuO.

2.3.2. Sub-Eutectic Activated Sintering

Fig. 2.4 shows the linear shrinkage *vs.* temperature curves of undoped and 4 mol. % CuO-doped TiO_2 (rutile) measured by dilatometry at a constant heating rate of 5 °C per minute. The doped powders were prepared by either a dry mixing or a wet chemistry method described in the “Experiments” section. At 1000 °C, undoped TiO_2 specimen had ~15% linear shrinkage. In contrast, CuO-doped TiO_2 specimens had ~32% and ~28% linear shrinkage, respectively, for specimens prepared by the wet chemistry and dry mixing methods, respectively. Both doped TiO_2 specimens had ~99% of the theoretical density after the sintering experiments

(including possible extra densification during the cooling in the furnace after the dilatometry experiments). These results clearly demonstrated that the addition of CuO effectively promoted the densification of rutile TiO_2 below the bulk eutectic temperature, where the significant enhanced densifications occurred at 200-300 °C below the bulk eutectic temperature. The specimen prepared by the wet chemistry method, where the doping was presumably more uniform, exhibited significant enhanced densifications at even lower temperatures (Fig. 2.4).

To further investigate the sintering mechanism, 4 mol. % CuO-doped TiO_2 specimens were isothermally annealed (sintered) at 800 °C, 850 °C, and 900 °C, respectively, for 8 hours and subsequently water-quenched. The microstructures of the fractured surfaces of the sintered specimens are shown in Fig. 2.5 and the measured grain sizes are shown in Fig. 2.6. Specifically, Figs. 2.5 (a-f) show the SEM images of sintered CuO-doped TiO_2 specimens that were prepared by the wet chemistry method. Low-magnification images show uniform structures and the average grain size increased substantially from 800 °C to 900 °C. Interestingly, a secondary phase (presumably CuO) appeared to wet some triple-grain junctions (with low dihedral angles that, in addition to the nanoscale IGFs at GBs, can also promote sintering and affect microstructural development, as reviewed and discussed by Castro and Gouvêa [20]) of the specimen sintered and quenched from 900 °C (Fig. 2. 5(f)), but not in those at lower temperatures. Figs. 2.5 (g-i) display high-magnification SEM images of the CuO-doped TiO_2 prepared by the dry mixing method, sintered at 800 °C, 850 °C, and 900 °C, respectively, for 8 hours, and subsequently water quenched. Substantial neck formation and growth

were evident in all sub-eutectic sintered specimens (Figs. 2.5 (d-i). Finally, we note that the grain growth followed similar trends for the specimens doped by the wet chemistry and dry mixing routes, both of which contained 4 mol. % CuO and were isothermally annealed at 800-900°C for 8 hours (Fig. 2.6).

2.3.3. Stabilization of Liquid-Like GB Complexion Below the Bulk Eutectic Temperature

Fig. 2.7 and Fig. 2.8 display the HRTEM images of representative GBs in 4 mol. % CuO-doped TiO_2 specimens that were equilibrated (by isothermal annealing for 8 hours) at 800 °C, 850 °C, and 900 °C, respectively, in a calibrated muffle furnace and subsequently water-quenched. In all cases, the GB planes were carefully oriented to be parallel with the incident electron beam to ensure edge-on conditions. Nanometer-thick, structurally disordered (liquid-like) IGFs were observed in all specimens quenched from 800 °C, 850 °C, and 900 °C after annealing for 8 hours, at all GBs that were examined. The measured individual and average thicknesses of the IGFs were listed in Table I. Specifically, the average measured thickness of the liquid-like IGFs formed at 800°C (and $\pm$ one standard deviation) was 0.70 ± 0.07 nm, which increased to 0.86 ± 0.06 nm for the IGFs formed at 850 °C and 0.98 ± 0.09 nm for the IGFs formed at 900°C. These nanoscale IGFs represent a liquid-like interfacial complexion that is thermodynamically stabilized at the general GBs below the bulk eutectic temperature; this stabilization will be quantitively justified by an interfacial

thermodynamic model in section 2.4.2 and its roles in activated sintering will be discussed in section 2.4.3.

2.4. Modeling and Discussion

2.4.1. The TiO_2-CuO Binary Phase Diagram and Bulk Thermodynamic Function

In 2001, a binary TiO_2-CuO phase diagram had been calculated via assuming that the liquid phase is an ideal solution, which produced an eutectic temperature of 919 °C [14], being substantially lower than the ~1000 °C eutectic temperature that was later suggested via DSC and TG analysis in 2012 [15] and largely confirmed more directly and accurately by the current study. That diagram reported in 2001 [14] represents the only TiO_2-CuO phase diagram available in literature and has been widely cited. The more accurate measurements of the eutectic temperature and composition obtained in this study, which were consistent with the independent DSC/TG study in 2012 [15], demand a further assessment (and correction) of that TiO_2-CuO phase diagram, which will also provide the thermodynamic function of the liquid phase that will be useful for the interfacial thermodynamic model presented and discussed in the following section.

To compute the binary phase diagram, we assume that CuO and TiO_2 are mutually immiscible in the solid states (since no detectable solid solubility was reported in literature, which was also verified by EDX analysis in the current study) and use the solid phases as the reference state. The free energy of the TiO_2-CuO liquid phase (referenced to the two bulk solid phases) is expressed as a Redlich-

Kister polynomial (n = 0 and 1 for a subregular solution):

$$\Delta G^{Liq} = X_{CuO}^{Liq}\Delta G_{CuO}^{Liq} + X_{TiO_2}^{Liq}\Delta G_{TiO_2}^{Liq} + RT\left(X_{CuO}^{Liq} ln X_{CuO}^{Liq} + X_{TiO_2}^{Liq} ln X_{TiO_2}^{Liq}\right) + \sum_{n=0,1} L_n \left(X_{CuO}^{Liq} - X_{TiO_2}^{Liq}\right)^n X_{CuO}^{Liq} X_{TiO_2}^{Liq} \quad (1)$$

where X_i^{Liq} is the bulk molar fraction of the i component (i = CuO, TiO_2) and L_n^{Liq} is the interaction parameters. ΔG_i^{Liq}, the bulk molar fraction and free energy of forming the liquid phase from the solid phase of the i component, can be derived as

$$\Delta G_i^{Liq} = (T_i^m - T)\Delta S_i^{melt} + \int_{T_i^m}^{T} \Delta C_{P(i)}\, dT - T\int_{T_i^m}^{T} \frac{\Delta C_{P(i)}}{T} dT \quad (2)$$

where T_i^m is the melting temperature, ΔS_i^{melt} is the molar entropy of fusion (melting), and $\Delta C_p = C_p^{Liq} - C_p^{Sol}$ is the molar heat capacity difference between solid and liquid phases. For the TiO_2-CuO system, these thermodynamic parameters of individual components (TiO_2 and CuO) were taken from Ref. [14], which were originally obtained from a CRC handbook [21]. Subsequently, we obtained the parameters $L_0 = 8.4\ \mathrm{kJ/mol}$ and $L_1 = -13.0\ \mathrm{kJ/mol}$ by solving two equations: $\Delta G^{Liq} = 0$ and $\frac{\partial \Delta G^{Liq}}{\partial X_{CuO}} = 0$ to match the experimentally-measured eutectic temperature (T^{Eutectic} = 1010 °C) and composition ($X_{CuO}^{Eutectic}$ = 0.832). Here, the liquid phase is a subregular solution (L_n = 0 for $n \geq 2$ in the Redlich-Kister polynomial). From the derived thermodynamic function (Eq. (1)), we calculated the binary (bulk) phase diagram for the TiO_2-CuO system, which is shown in Fig. 2.9.

We should further note that CuO reduces to Cu_2O at 1029 °C in one-atmosphere air [22] so that the above computation only represents the cases that

CuO would remain stable at high temperatures (achievable at higher P_{O_2}). Unfortunately, there is no data available for us to calculate the exact the TiO_2-CuO-Cu_2O pseudo-binary phase diagram in one-atmosphere air, but we sketch the possible transitions as the dotted lines in Fig. 2.9 based the Cu_2O-Cu_2O reduction temperature and the melting temperature of Cu_2O, which are the only known points in the TiO_2-CuO-Cu_2O phase diagram. Nonetheless, this Cu_2O-to-Cu_2O reduction occurring at 1029 °C should not affect the eutectic reaction at 1010 °C and the stabilization and temperature-dependence of sub-eutectic liquid-like GB complexion (to be discussed in the next section).

2.4.2. An Interfacial Thermodynamic Model and the Computed GB λ Diagram

The thermodynamic stability of nanoscale quasi-liquid IGFs (specifically) and GB complexions (in general) have been reviewed [23, 24]. Furthermore, GB λ diagrams have been computed and proven useful for predicting trends in activated sintering in (at least) several refractory alloys [25-31]. Here, we made a first successful attempt to extend the prior successes from metallic alloys [25-31] to a ceramic system.

At the length scale of 0.5-5 nm, a phenomenological interfacial thermodynamic model can be formulated for premelting-like IGFs in multicomponent ceramics by combining a sharp-interface model of premelting in unary systems [32] and the Clarke model for equilibrium-thickness IGFs [33, 34]. Here, an IGF in the TiO_2-CuO is treated as a confined liquid-like interfacial film (*a.k.a.* a specific 2-D interfacial phase) with modified thermodynamic properties.

The excess grand potential as a function of the film thickness (h) can be written as:

$$\sigma^{x}(h) = 2\gamma_{\mathrm{cl}} + \Delta G_{\mathrm{amorph}}^{(\mathrm{vol})} \cdot h + \sigma_{\text{short-range}}(h) + \sigma_{\mathrm{vdW}}(h) + \sigma_{\mathrm{elec.}}(h) + \ldots \quad (3)$$

where γ_{cl} is the crystal-liquid interfacial energy (that is well defined as $h \rightarrow +\infty$) and $\Delta G_{\mathrm{amorph}}^{(\mathrm{vol})}$ is the volumetric free energy for forming an undercooling liquid from the equilibrium solid phases. The last three terms are short-range, van der Waals (vdW) dispersion, and electrostatic interfacial interactions, which should all vanish as $h \rightarrow +\infty$ by definition. A premelting-like GB complexion can be stabilized below the bulk eutectic temperature if the energy penalty for forming an undercooled quasi-liquid film (interfacial phase) of thickness h is overcompensated by the reduction in the total (effective) interfacial energy:

$$-\Delta\gamma \cdot f(h) > \Delta G_{amorph}^{(vol)} h \quad (4)$$

where

$$\Delta\gamma \equiv 2\gamma_{\mathrm{cl}} - \sigma^{x}(0) \quad (5)$$

and $f(h)$ is a dimensionless interfacial coefficient (that varies from $f(0) = 0$ to $f(+\infty) = 1$ by definition, but not necessarily monotonically), defined as:

$$f(h) = 1 + \frac{\left[\sigma_{\text{short-range}}(h) + \sigma_{\mathrm{vdW}}(h) + \sigma_{\mathrm{elec.}}(h) + \ldots\right]}{\Delta\gamma} \quad (6)$$

The equilibrium thickness, h_{EQ}, corresponds to the minimum of Eq. (3), which implies:

$$\begin{cases} \left.\dfrac{d\sigma^{x}(h)}{dh}\right|_{h=h_{EQ}} = 0 \\ \left.\dfrac{d^{2}\sigma^{x}(h)}{dh^{2}}\right|_{h=h_{EQ}} > 0 \end{cases}. \tag{7}$$

Based on the thermodynamic criterion for stabilizing a sub-eutectic, liquid-like, GB complexion (Eq. (4)), we again adopt (and, in the next step, quantify) a thermodynamic parameter, λ, to represent the thermodynamic tendency for general GBs to disorder, following earlier studies of metallic alloys [25-31], which is expressed as:

$$\lambda \equiv \frac{-\Delta\gamma}{\Delta G_{\text{amorph}}^{(\text{vol})}}, \tag{8}$$

To quantify values of λ, ΔG_{amorph}^{vol}, the volumetric free energy penalty of forming an undercooling liquid below eutectic temperature, is expressed as:

$$\Delta G_{amorph}^{vol} \approx \Delta G_{amorph}^{mol} / \left[(1 - X_{CuO}^{IGF}) V_{m(TiO_2)} + X_{CuO}^{IGF} V_{m(CuO)}\right] \tag{9}$$

where X_{CuO}^{IGF} is the average IGF composition and $\Delta G_{amorph}^{mol} = \Delta G^{Liq}(X_{CuO}^{IGF})$, which can be calculated using Eq. (1) and the thermodynamic function and data obtained in the prior section for the TiO_2-CuO liquid phase. Here, the most common and convenient way is to select the X_{CuO}^{IGF} that maximizes λ, as discussed in prior studies of metallic alloys [25-31].

To quantify $\Delta\gamma$, $\sigma^{x}(0) \equiv \gamma_{GB}^{(0)}$, the average general GB energy of pure TiO_2 (with no adsorption), was measured in a prior experiment to be 0.87 J/m^2 [35]. Analogous to both a “macroscopic-atoms” model [36, 37] and a lattice model [38] (with modifications), we estimate the average interfacial energy for the crystal-

liquid interface between a pure TiO_2 solid and a TiO_2-CuO binary liquid using the following expression:

$$\gamma_{cl} = \frac{\Delta H_{TiO_2}^{melt}}{\kappa m_1^{-1} V_m^{2/3}} + \frac{\Omega_{CuO-TiO_2}^{Liq}}{\kappa m_1^{-1} V_m^{2/3}} (X_{CuO}^{IGF})^2 \quad (10)$$

where the two terms represent the enthalpic (fusion) and chemical (interaction) contributions, respectively, to the crystal-liquid interfacial energy. Here, $\Delta H_{TiO_2}^{melt}$ is the molar enthalpy (latent heat) of melting, $\Omega_{CuO-TiO_2}^{Liq} = L_0$ is the regular-solution parameter for the liquid phase, V_m is the molar volume of TiO_2, κ is a geometric factor ($\kappa \equiv A_m/V_m^{2/3}$, where A_m is the area of one mole of molecules spread as a monolayer [38]), and m_1 is the fraction of bonds across the crystal-liquid interface. The value of κm_1^{-1} in Eq. (10) depends on the lattice structure and orientation of the interface and we use $\kappa m_1^{-1} = C_0 \approx 4.5 \times 10^8$ to represent the average of different orientations [39] to represent IGFs formed at the average general GBs.

Subsequently, we computed λ values and plotted them in the bulk TiO_2-CuO phase diagram to construct a GB λ diagram for CuO-doped TiO_2, as shown in Fig. 2.10, similar to the GB λ diagrams constructed in prior studies for several metallic alloys [25-31]. In the sub-eutectic two-phase region, the computed λ increases with increasing temperature, suggesting increasing thermodynamic tendency for average general GBs to disorder that should result in increasing densification rates, consistent with both the intuition and experiments.

A more rigorous and accurate assessment of IGF thickness (h_{EQ}) *vs.* temperature requires the quantitative information about the short-range, vdW

dispersion, electrostatic, and any other interfacial interactions in Eq. (3), which is unfortunately not available for the current case of TiO_2-CuO as well as virtually all other ceramic systems. However, we may adopt a simplified model to justify the observed temperature-dependent IGF thicknesses in the intermediate temperature region (to be defined and discussed subsequently), as follows. First, prior analyses showed that the vdW dispersion interaction, which is always attractive for the IGFs, will be overwhelmed by the ΔG_{amorph}^{vol} term that represents a significantly higher attractive pressure than the vdW dispersion pressure at $\Delta T \equiv T - T^{\text{Eutectic}} \geq 100$ °C [24, 40]; thus, the vdW dispersion interaction can be neglected well below the eutectic temperature. Moreover, either the short-range or electrostatic interaction can be approximated with an exponentially-decaying form (and only one of them likely dominates in a specific ceramic system). Thus, in a simplified model, we can adopt an exponentially-decaying interfacial potential, $f(h) = 1 - \exp(-h/\xi)$, so that Eq. (3) can be rewritten and simplified to:

$$\Delta\sigma(h) \equiv \sigma^x(h) - \sigma^x(0) = \Delta\gamma \cdot f(h) + \Delta G_{amorph}^{(vol)} \cdot h = \Delta\gamma \cdot \left[1 - \exp(-h/\xi)\right] + \Delta G_{amorph}^{(vol)} \cdot h \quad (11a)$$

where ξ is a coherent length [27]. Eq. (11a) can also be rewritten into a dimensionless form:

$$\frac{\Delta\sigma(h)}{-\Delta\gamma} = \frac{h}{\lambda} + \exp(-h/\xi) - 1. \quad (11b)$$

Minimizing Eq. (11b) with respective to *h* produces the equilibrium IGF thickness:

$$h_{EQ} = \xi \ln(\lambda/\xi). \quad (12)$$

We should further make two notes. First, Eq. (12) is obtained via assuming a fixed

average film composition that maximizes λ in Eq. (8). Alternatively, we may minimize Eq. (11a) with respective to both h and X_{CuO}^{IGF}. Our numerical analysis showed negligible differences between the calculated "$h_{EQ.}$ *vs. T*" curves using the two approaches, so we choose the simpler approach [by using Eq. (12)]. Second, this simplified model [Eq. (11) and Eq. (12)] can only be used for the intermediate temperature region. On one hand, at higher temperatures ($T \sim T^{Eutectic}$), the divergence of h_{EQ} predicted from this model should be limited by the attractive vdW dispersion interaction. On the other hand, at lower temperatures, this continuum model is no longer valid when $h_{EQ} < \sim 0.5$ nm because it does not consider the discrete nature of ion sizes and bond lengths. Nonetheless, this simplified model can be used to justify the measured temperature-dependent IGF thicknesses in the intermediate temperature region of 800-900 °C for the current case, which is the range of interest for activated sintering.

Specifically, Fig. 2.11 plots the means and standard deviations of IGF thicknesses measured by HRTEM from specimens equilibrated at 800 °C, 850 °C, and 900 °C, along with the computed "$h_{EQ.}$ *vs. T*" curves for three different selections of the coherent length, ξ. The computed "$h_{EQ.}$ *vs. T*" curve with ξ = 0.38 nm produced the best fit to the experimental data, while the sensitivity of the different selections of ξ was also tested. Although we do not have the knowledge of the exact value of the coherent length, the value that produced the best fit (~0.38 nm) is about twice of the O-Cu bond length or the size of a Cu-O_n polyhedral unit, which appears to be reasonable. Thus, this rather simplified model can justify the stabilization of liquid-like GB complexions below the eutectic temperature as well

as the temperature-dependent interfacial widths (the measured "$h_{EQ.}$ *vs. T*") observed by HRTEM.

Lastly, we should also recognize the possibility that some of these IGFs exhibit discrete (instead of continuous) thickness (to form Dillon-Harmer GB complexions [23, 41]) for certain specific GBs, *e.g.*, some special GBs with low-index grain surfaces, as shown in a prior study for a (001) // (100) GB in a (CuO + SiO_2) doped TiO_2 bicrystal specimen [41]. The origin of the discrete thicknesses and the formation of Dillon-Harmer GB complexions can be explained in the same interfacial thermodynamic framework discussed above via incorporating (adding) an oscillatory structural interaction (as a result of a fixed, finite, atomic size using a hard-sphere approximation) in Eq. (3) or the interfacial coefficient $f(h)$ [31, 41-43].

2.4.3. Further Discussion of Activated Sintering Mechanisms and Beyond

The current study measured the eutectic temperature of the TiO_2-CuO system to be 1010 ± 10 °C in air, which was higher than that reported in 2001 [14], but similar to that suggested by a DSC and TG study in 2012 [15]. This warrantees our re-assessment and a correction of the TiO_2-CuO phase diagram reported in Ref. [14] in 2001 based our measured bulk eutectic temperature and composition to compute an improved (corrected) TiO_2-CuO phase diagram in Fig. 2.8; this assessment also provided the thermodynamic function for justifying the stabilization of a sub-eutectic liquid-like GB complexion, which leads to enhanced interfacial mass transport and subsequently activated sintering.

The combination of our experimental results undoubtedly demonstrated that the enhanced sintering of CuO-doped TiO_2 occurred in the sub-eutectic region, starting at >300 °C below the bulk eutectic temperature. Thus, this study clearly disapproved the theory that the enhanced sintering in CuO-doped TiO_2 at ~850-950 °C is due to liquid-phase sintering, that was widely assumed in prior studies [10, 12, 13]. Instead, this study unequivocally demonstrated, via a combination of HRTEM and thermodynamic modeling, that the addition of CuO promoted the formation of a liquid-like GB complexion in TiO_2 well below the bulk eutectic temperature, which provides a fast mass transport pathway to enhance sub-eutectic densification. Similar solid-state activated sintering behaviors and mechanisms have been observed/identified for several ceramic (Bi_2O_3-doped ZnO [16]) and metallic (Ni-doped W and Mo [17-19]) systems.

We should also recognize and further discuss alternative mechanisms that may enhance sintering and grain growth/coarsening below the eutectic temperatures. Specifically, a most recent study by Wu, Dholabhai, Uberuaga, and Castro showed that the reduction of Mn cations from 3+ to 2+ in Mn-doped CeO_2 can result in significant coarsening [44]. In the current case, CuO can also be reduced to Cu_2O at 1029 °C [22] (with some partial reduction starts at ~1000 °C as shown in an earlier study [15]), whereas the enhanced densification can occur at much lower temperatures (as low as 700-900°C; Figs. 4 and 5) without substantial coarsening (Fig. 2.6).

The thermodynamic stabilization of nanometer-thick quasi-liquid IGFs below eutectic temperature in CuO-doped TiO_2 has been well justified by

estimating relative interfacial energies via both experimental data and a statistical model as well as quantifying free-energy penalty for forming undercooled liquids using CALPHAD data. Subsequently, an interfacial thermodynamic model is used to justify the temperature-dependent interfacial width.

Following the earlier successes of constructing GB λ diagrams to predict useful trends in high-temperature GB disordering and to subsequently forecast activated sintering behaviors (and potentially other materials properties such as creep resistance) in several W- and Mo based metallic alloys [25-31] (as well as more rigorous computed GB complexion diagrams with well-defined transition lines, such as that for Bi-doped Ni in a most recent report [45]), this study made a first successful attempt to extend the model and method to compute the first GB λ diagram for a ceramic system (CuO-doped TiO_2). In future studies, similar or more rigorous “GB diagrams” should be developed for other ceramic systems, which can have broad applications. This is in part because this class of nanoscale IGFs are more ubiquitous and technologically-important for ceramics than metals in general. Furthermore, it is worth noting that nanometer-thick IGFs investigated in this study only represent one of several types of GB complexions discovered recently [23, 46-48]; such GB complexions (*a.k.a.* interfacial phases that are thermodynamically 2-D) exist ubiquitously in both metallic and ceramic materials, where they can often critically influence or even control a board range of transport, mechanical, and physical properties [23, 25, 27, 43, 46, 49-66] beyond sintering.

2.5. Conclusions

The eutectic temperature of the CuO-TiO_2 system has been determined to be 1010 ± 10 °C and the eutectic composition was measured to be ~17TiO_2:83CuO (or ~17 mol. % TiO_2 + ~83 mol. % CuO). Based on the measured eutectic temperature and composition, we computed the binary TiO_2-CuO phase diagram (representing a significant improvement from, and essentially a correction of, the phase diagram available in literature) and formulated the relevant thermodynamic function. A combination of dilatometry measurements and isothermal sintering experiments unequivocally demonstrated the occurrence of activated sintering in CuO-doped TiO_2 at as low as >300 °C below the bulk eutectic temperature. HRTEM characterization of well-quenched specimens further revealed the formation of nanometer-thick, liquid-like IGFs. The enhanced mass transport in this premelting-like complexion explained the activated (enhanced) sintering observed in this system. We further calculated a GB λ diagram, for the first time for any ceramic system, to represent the thermodynamic tendency for general GBs in CuO-doped TiO_2 to disorder and used an interfacial thermodynamic model to quantitively explain and justify the stabilization of nanometer-thick, liquid-like IGFs below the bulk eutectic temperature as well as the temperature-dependent IGF thicknesses measured by HRTEM. In future studies, similar or different (more rigorous and sophisticated) types of GB diagrams should be computed for other ceramic materials, which can potentially have broad scientific and technological impacts.

Chapter 2, in part, is a reprint of the material “Liquid-Like Grain Boundary Complexion and Sub-Eutectic Activated Sintering in CuO-Doped TiO_2”, J. Nie, J.M. Chan, M. Qin, N. Zhou, J. Luo, as it appears in Acta Materialia, 2017, 130, 329. The dissertation author was the primary investigator and author of this paper.

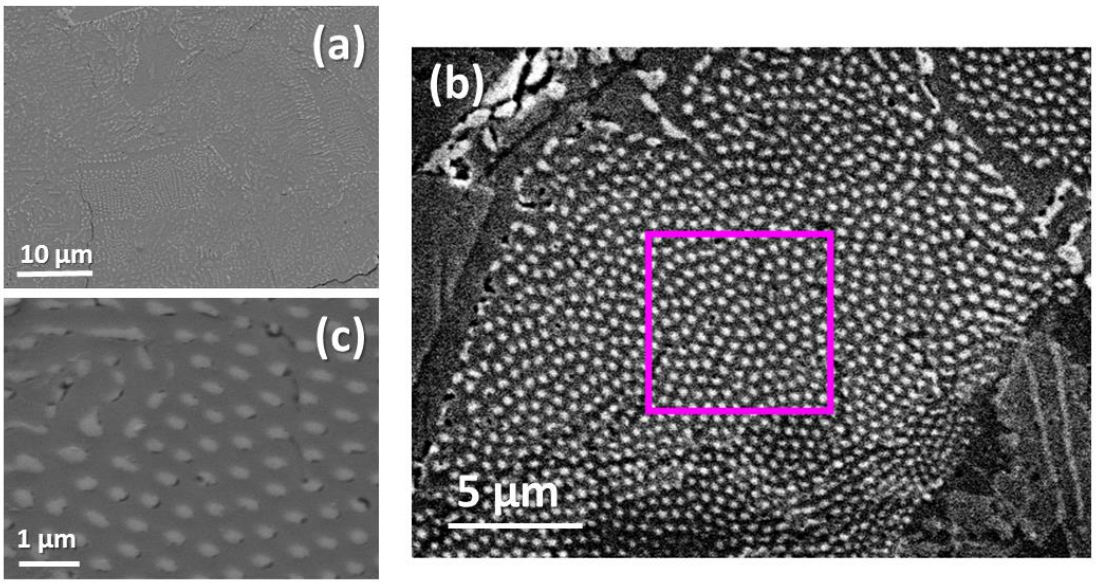

Figure 2.1 SEM images of an 80 mol. % CuO + 20 mol. % TiO_2 specimen isothermally annealed at 1020°C for 0.5 hour and water-quenched, showing the formation of a eutectic structure. A quantitative composition analysis of the region highlighted in (b) was performed to measure the eutectic composition (to be ~ 83CuO:17TiO_2).

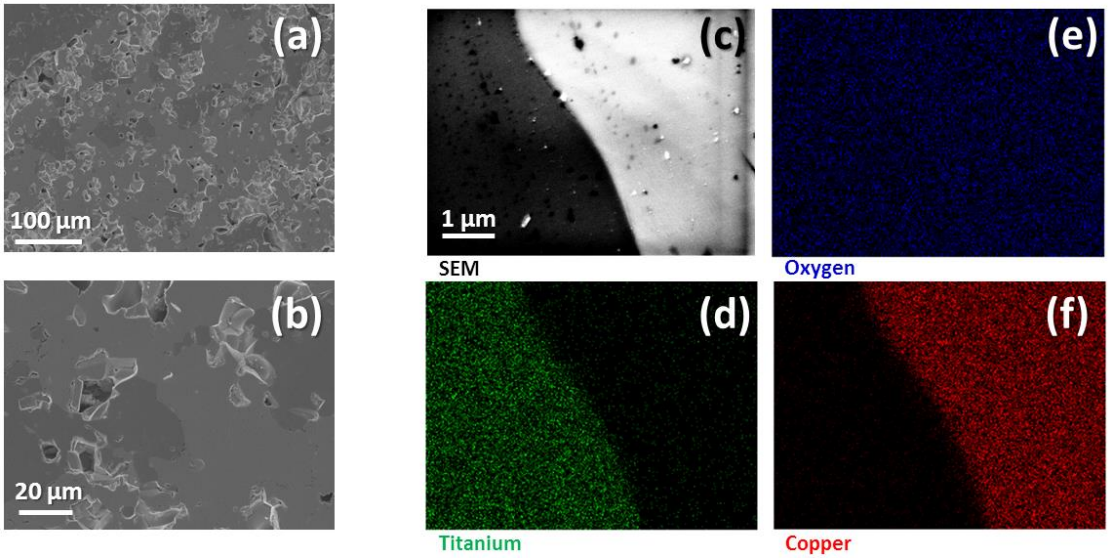

Figure 2.2 (a-c) SEM images and (d-f) EDS elemental maps of titanium, copper, and oxygen of an 80 mol. % CuO + 20 mol. % TiO_2 specimen that was isothermally annealed at 1000°C for 8 hours and water-quenched, where a eutectic structure is lacking. The specimens were made by a dry mixture powders; large particles of CuO remained and the originally-smaller TiO_2 particles sintered, whereas no indication of any reaction was evident.

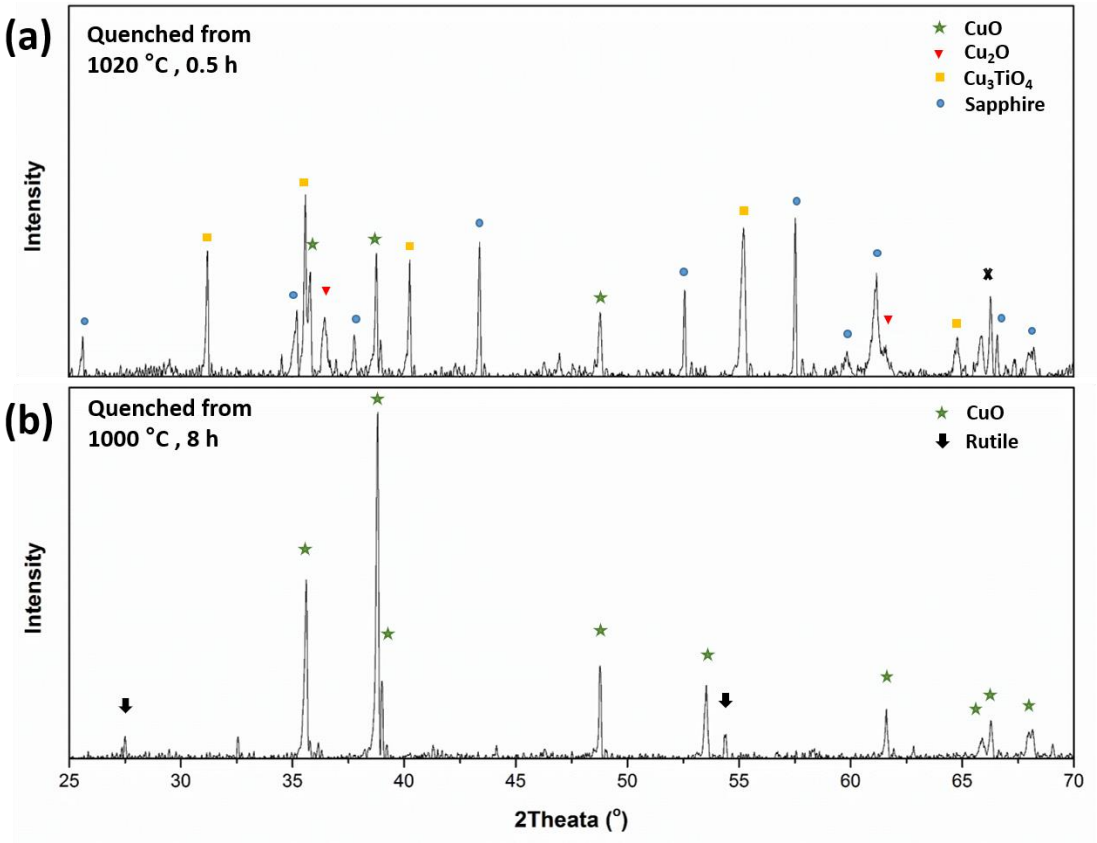

Figure 2.3 X-ray diffraction patterns of 80 mol. % CuO + 20 mol. % TiO_2 specimens isothermally annealed and quenched from (a) 1000°C and (b) 1020°C, respectively.

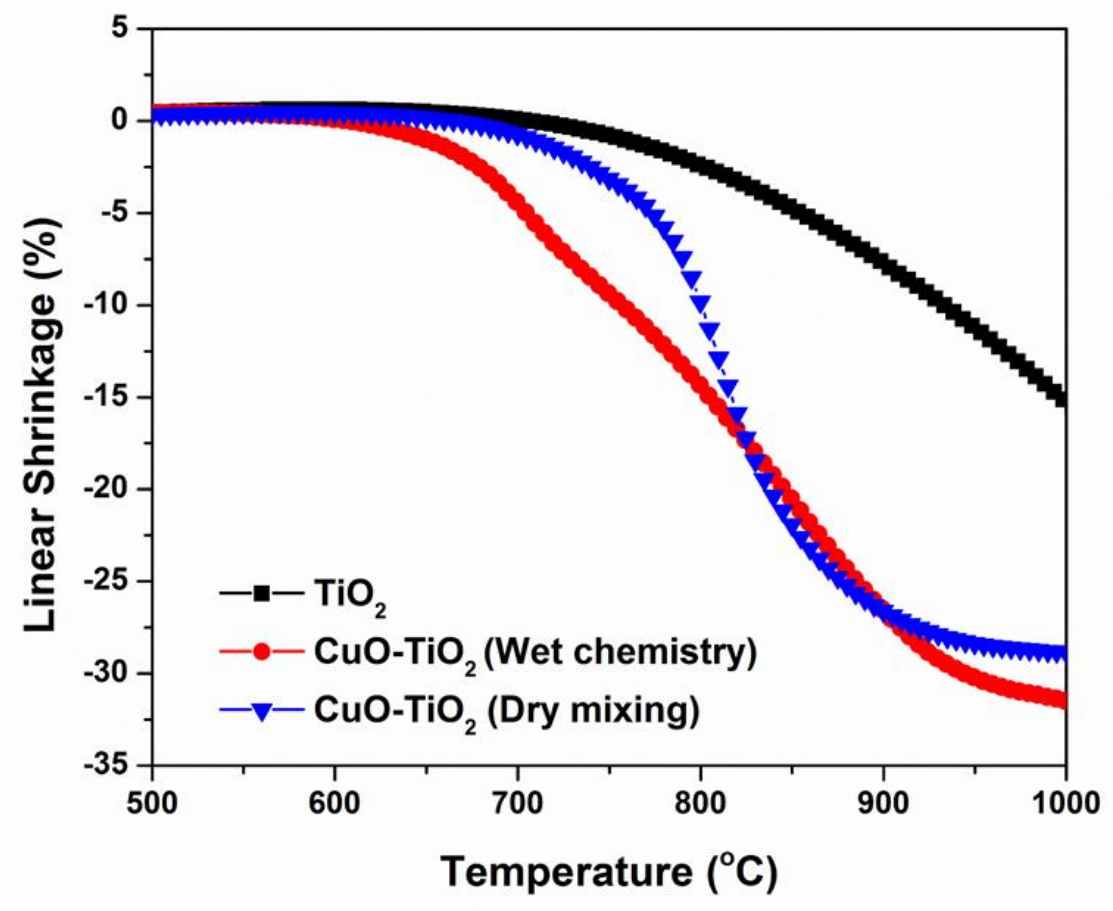

Figure 2.4 Linear shrinkage *vs.* temperature curves of pure TiO_2 and 4 mol. % CuO-doped TiO_2 prepared by two different methods (via wet chemistry and dry mixing routes). All powders were uniaxially pressed at 200 MPa and measured using a dilatometer with a constant ramping rate of 5°C per minute.

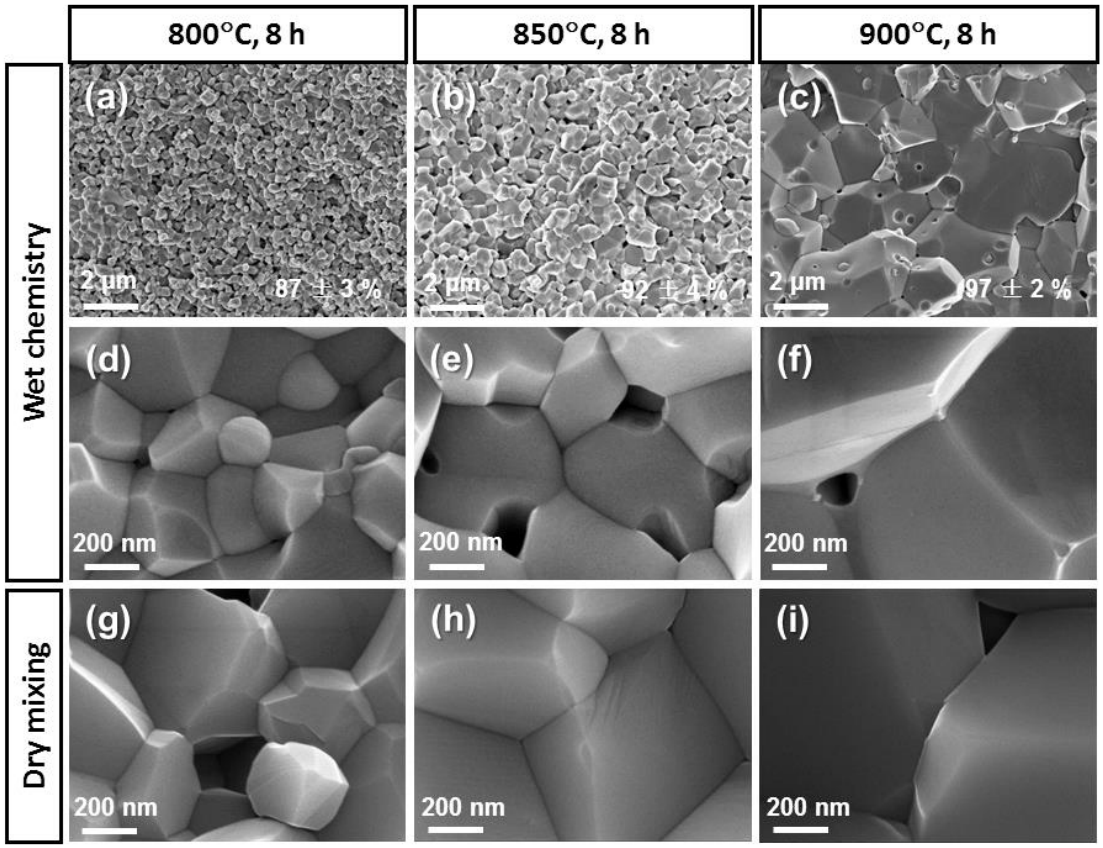

Figure 2.5 (a) SEM images of 4 mol. % CuO-doped TiO_2 prepared by two different methods via wet chemistry and dry mixing routes, respectively, isothermally annealed at 800°C, 850°C, and 900°C, respectively, for 8 hours, and water-quenched.

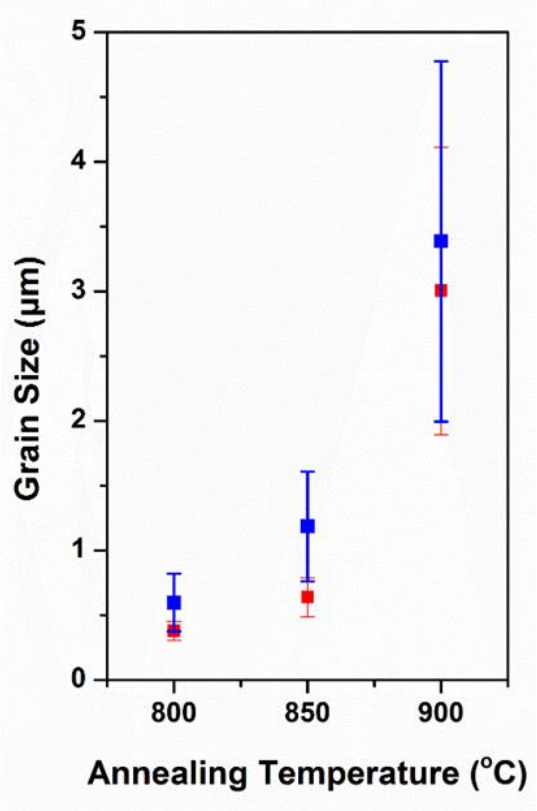

Figure 2.6 Measured grain sizes of 4 mol. % CuO-doped TiO_2 specimens, made by the wet chemistry (red) and dry mixing (blue) routes, isothermally annealed at 800°C, 850°C, and 900°C, respectively, for 8 hours, and water-quenched. The grain growth behaviors are similar for specimens doped by two different methods.

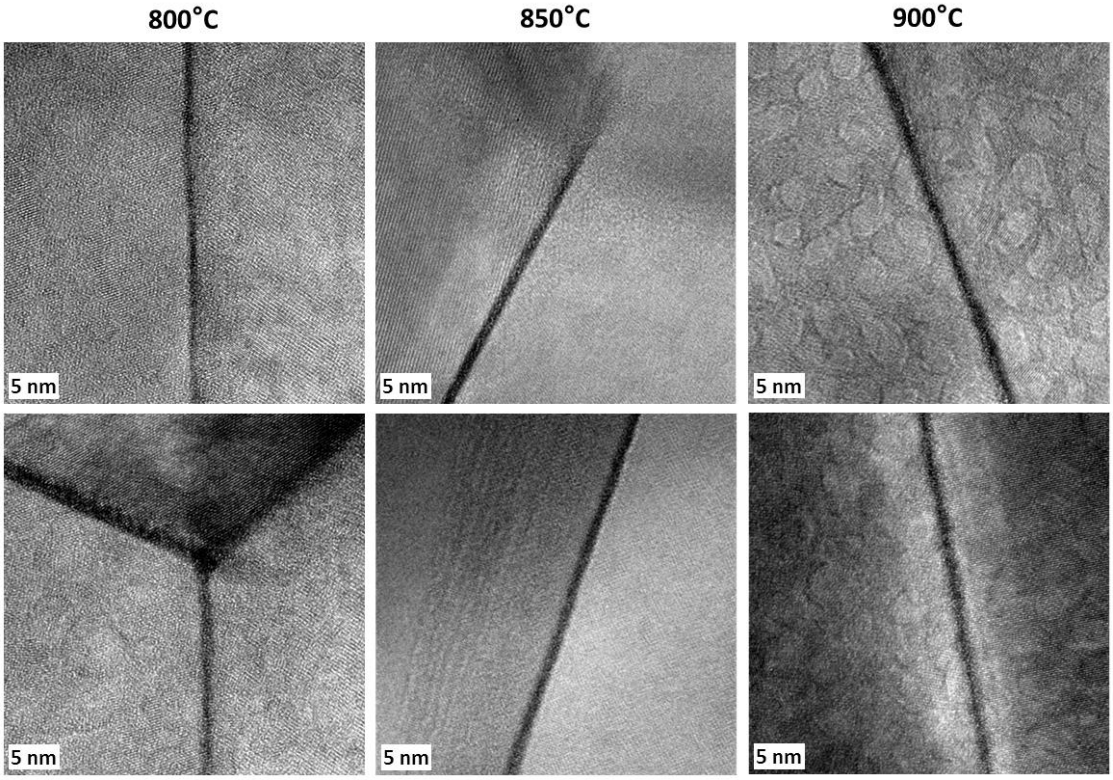

Figure 2.7 HRTEM images of 4 mol. % CuO-doped TiO_2 specimens isothermally annealed at 800°C, 850°C, and 900°C, respectively, for 8 hours and water-quenched.

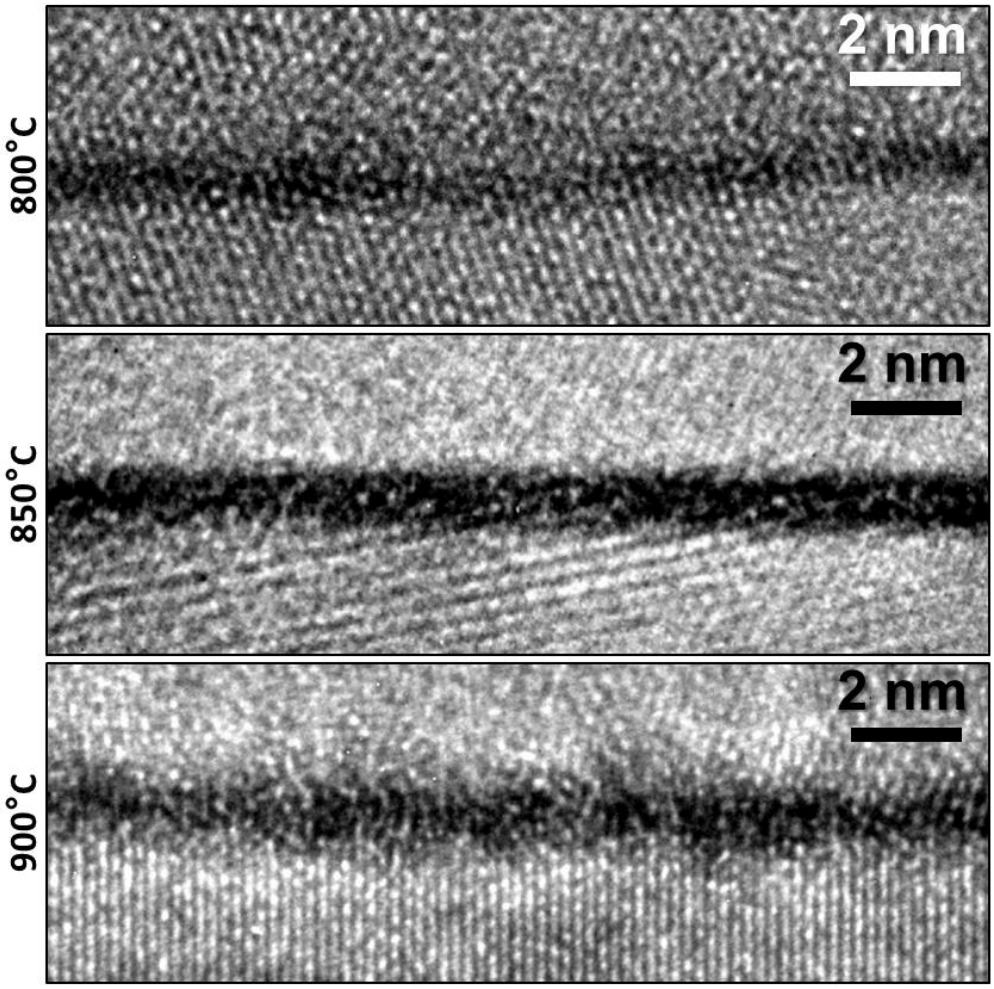

Figure 2.8 HRTEM images of 4 mol. % CuO-doped TiO_2 specimens equilibrated and quenched at 800°C, 850°C, and 900°C, respectively, at a higher magnification.

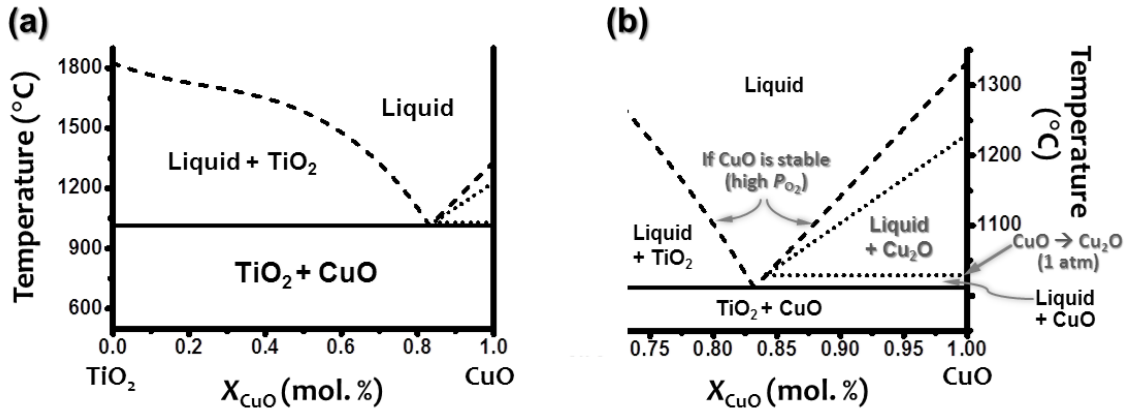

Figure 2.9 Computed TiO_2–CuO phase diagram of (a) the full composition range and (b) an enlarged section of the CuO-rich region. It should be noted that CuO is reduced to Cu_2O at 1029℃ in air [22] and CuO would remain stable at higher temperatures only at higher P_{O2}. Due to the absence of the Cu_2O-TiO_2 thermodynamic data, we can only calculate the TiO_2–CuO phase diagram. The dotted lines represent the possible transition lines in air with the CuO–Cu_2O transformation, while dashed lines represent the calculated phase transformation lines for the TiO_2–CuO system assuming no reduction at high temperatures.

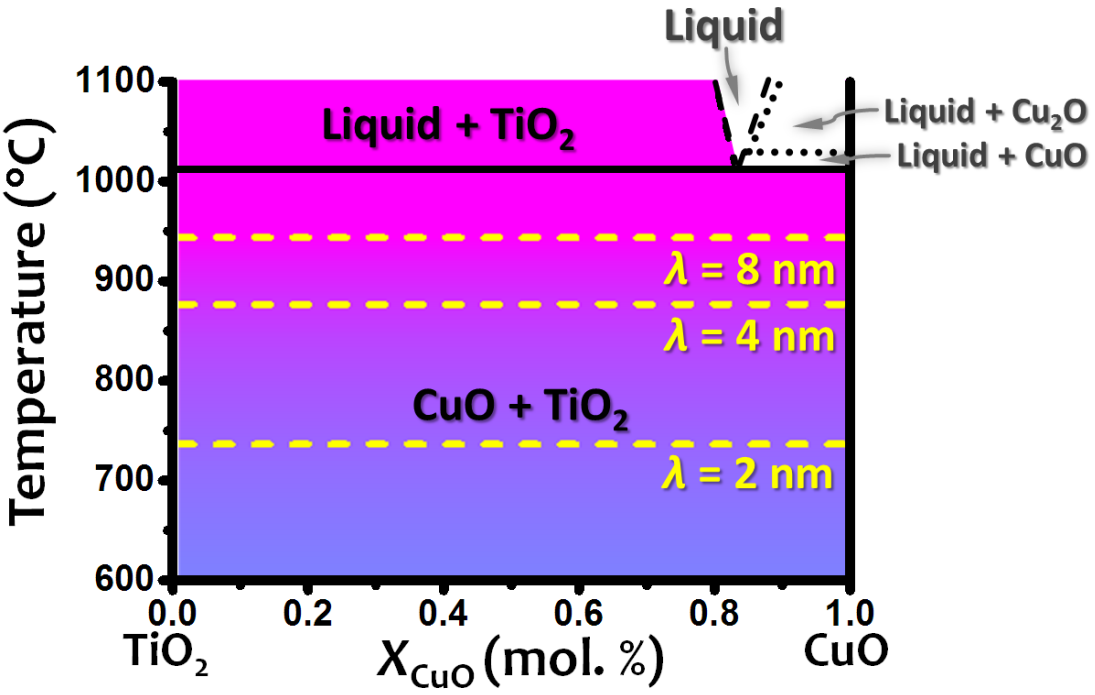

Figure 2.10 A computed GB λ diagram, where the dash lines represent λ = 2 nm, 4 nm, and 8 nm, respectively, and the color represent the relative thermodynamic tendency for the average general GBs in CuO-doped TiO_2 to disorder.

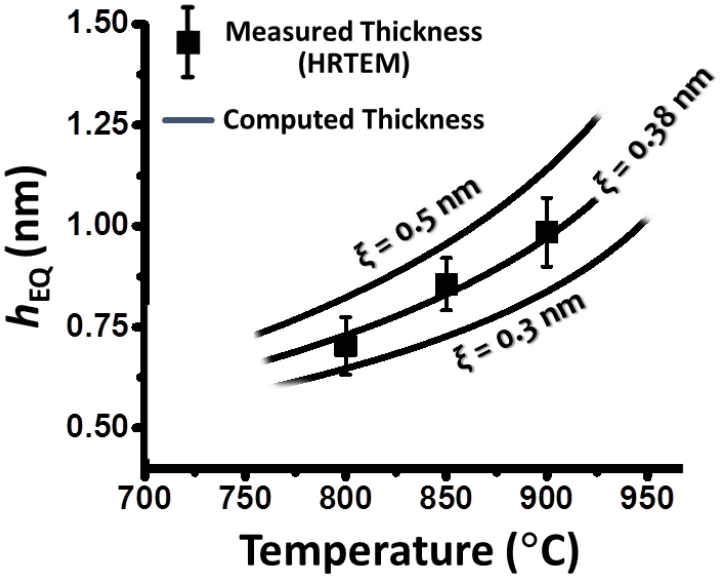

Figure 2.11 The average IGF thicknesses *vs.* equilibration temperatures measured by HRTEM. The three solid lines represent the computed equilibrium thickness ($h_{EQ.}$) as functions of temperature with three different coherence lengths (ξ = 0.3 nm, 0.38 nm, and 0.5 nm, respectively, where ξ = 0.38 nm represents the best fit with the experimental data).

Table 2.1 Measured IGF thicknesses of 4 mol. % CuO-doped TiO_2 specimens equilibrated (isothermally annealed for 8 h) at 800°C, 850°C, and 900°C for 8 hours and water-quenched. Three general GBs were measured for each of three specimens. For each of the nine GBs, the IGF thicknesses were measured at 10 different locations; the mean and standard deviations (that represent the uniformities of IGF thicknesses along the individual GBs) were reported.

Specimens	800°C			850°C			900°C		
Measured Thickness of Individual IGFs (nm)	GB #1	GB #2	GB #3	GB #1	GB #2	GB #3	GB #1	GB #2	GB #3
	0.68 ± 0.05	0.69 ± 0.04	0.75 ± 0.10	0.89 ± 0.05	0.82 ± 0.07	0.86 ± 0.06	1.01 ± 0.07	0.92 ± 0.07	1.03 ± 0.07
Mean ± 1 St. Dev. (nm)	0.70 ± 0.07			0.86 ± 0.06			0.98 ± 0.09		

References

[1] M. Gratzel, Photoelectrochemical cells, Nature 414(6861) (2001) 338-344.

[2] R. Asahi, T. Morikawa, T. Ohwaki, K. Aoki, Y. Taga, Visible-light photocatalysis in nitrogen-doped titanium oxides, Science 293(5528) (2001) 269-271.

[3] X. Chen, S.S. Mao, Titanium dioxide nanomaterials: Synthesis, properties, modifications, and applications, Chemical Reviews 107(7) (2007) 2891-2959.

[4] F.M. Meng, Influence of sintering temperature on semi-conductivity and nonlinear electrical properties of TiO_2-based varistor ceramics, Materials Science and Engineering B-Solid State Materials for Advanced Technology 117(1) (2005) 77-80.

[5] L. Golonka, Technology and applications of low temperature cofired ceramic (LTCC) based sensors and microsystems, Bull Polish Acad Sci Tech Sci 54(2) (2006).

[6] M.T. Sebastian, H. Jantunen, Low loss dielectric materials for LTCC applications: a review, International Materials Reviews 53(2) (2008) 57-90.

[7] E.A. Barringer, H.K. Bowen, FORMATION, PACKING, AND SINTERING OF MONODISPERSE TIO_2 POWDERS, Journal of the American Ceramic Society 65(12) (1982) C199-C201.

[8] K.N.P. Kumar, K. Keizer, A.J. Burggraaf, T. Okubo, H. Nagamoto, S. Morooka, DENSIFICATION OF NANOSTRUCTURED TITANIA ASSISTED BY A PHASE-TRANSFORMATION, Nature 358(6381) (1992) 48-51.

[9] S.-H. Yoon, D.-W. Kim, S.-Y. Cho, K.S. Hong, Phase analysis and microwave dielectric properties of LTCC TiO_2 with glass system, Journal of the European Ceramic Society 23(14) (2003) 2549-2552.

[10] J.C. Chang, Y.F. Chen, J.H. Jean, Low-fire processing and dielectric properties of TiO_2 with MnO_x-CuO, Japanese Journal of Applied Physics Part 1-Regular Papers Short Notes & Review Papers 43(7A) (2004) 4267-4268.

[11] M. Valant, D. Suvorov, R.C. Pullar, K. Sarma, N.M. Alford, A mechanism for low-temperature sintering, Journal of the European Ceramic Society 26(13) (2006) 2777-2783.

[12] D.W. Kim, T.G. Kim, K.S. Hong, Low-firing of CuO-doped anatase, Materials Research Bulletin 34(5) (1999) 771-781.

[13] D.W. Kim, B. Park, J.H. Chung, K.S. Hong, Mixture behavior and microwave dielectric properties in the low-fired TiO_2-CuO system, Japanese Journal of

Applied Physics Part 1-Regular Papers Short Notes & Review Papers 39(5A) (2000) 2696-2700.

[14] F.H. Lu, F.X. Fang, Y.S. Chen, Eutectic reaction between copper oxide and titanium dioxide, Journal of the European Ceramic Society 21(8) (2001) 1093-1099.

[15] M.A. de la Rubia, J.J. Reinosa, P. Leret, J.J. Romero, J. de Frutos, J.F. Fernandez, Experimental determination of the eutectic temperature in air of the CuO-TiO_2 pseudobinary system, Journal of the European Ceramic Society 32(1) (2012) 71-76.

[16] J. Luo, H.F. Wang, Y.M. Chiang, Origin of solid-state activated sintering in Bi_2O_3-doped ZnO, Journal of the American Ceramic Society 82(4) (1999) 916-920.

[17] R.M. German, DIFFUSIONAL ACTIVATED SINTERING DENSIFICATION, MICROSTRUCTURE AND MECHANICAL-PROPERTIES, International Journal of Powder Metallurgy 19(4) (1983) 277-&.

[18] K.S. Hwang, H.S. Huang, Identification of the segregation layer and its effects on the activated sintering and ductility of Ni-doped molybdenum, Acta Materialia 51(13) (2003) 3915-3926.

[19] J.M. Yang, S.M. Jeng, S.Y. Chang, Fracture behavior of directionally solidified $Y_3Al_5O_{12}$/Al_2O_3 eutectic fiber, Journal of the American Ceramic Society 79(5) (1996) 1218-1222.

[20] Z.M. Zhao, L. Zhang, H.B. Bai, J. Zheng, J.J. Wang, Y. Fu, Fabrication of nano-micron Al_2O_3-ZrO_2 ceramic eutectic composites from the melts by the SHS metallurgical process, in: W. Pan, J.H. Gong, C.C. Ge, J.F. Li (Eds.), High-Performance Ceramics Iii, Pts 1 and 22005, pp. 1053-1056.

[21] V.S. Stubican, R.C. Bradt, EUTECTIC SOLIDIFICATION IN CERAMIC SYSTEMS, Annual Review of Materials Science 11 (1981) 267-297.

[22] J. Llorca, V.M. Orera, Directionally solidified eutectic ceramic oxides, Progress in Materials Science 51(6) (2006) 711-809.

[23] E. Jud, C.B. Huwiler, L.J. Gauckler, Sintering analysis of undoped and cobalt oxide doped ceria solid solutions, Journal of the American Ceramic Society 88(11) (2005) 3013-3019.

[24] E. Jud, Z. Zhang, W. Sigle, L.J. Gauckler, Microstructure of cobalt oxide doped sintered ceria solid solutions, Journal of Electroceramics 16(3) (2006) 191-197.

[25] H.J. Kleebe, M.K. Cinibulk, R.M. Cannon, M. Ruhle, STATISTICAL-ANALYSIS OF THE INTERGRANULAR FILM THICKNESS IN SILICON-NITRIDE CERAMICS, Journal of the American Ceramic Society 76(8) (1993) 1969-1977.

[26] S. Primdahl, A. Tholen, T.G. Langdon, MICROSTRUCTURAL EXAMINATION OF A SUPERPLASTIC YTTRIA-STABILIZED ZIRCONIA - IMPLICATIONS FOR THE SUPERPLASTICITY MECHANISM, Acta Metallurgica Et Materialia 43(3) (1995) 1211-1218.

[27] S.Y. Chung, S.J.L. Kang, Intergranular amorphous films and dislocations-promoted grain growth in $SrTiO_3$, Acta Materialia 51(8) (2003) 2345-2354.

[28] H.D. Ackler, Y.M. Chiang, Model experiment on thermodynamic stability of retained intergranular amorphous films, Journal of the American Ceramic Society 80(7) (1997) 1893-1896.

[29] J. Luo, V.K. Gupta, D.H. Yoon, H.M. Meyer, Segregation-induced grain boundary premelting in nickel-doped tungsten, Applied Physics Letters 87(23) (2005).

[30] V.K. Gupta, D.H. Yoon, H.M. Meyer, J. Luo, Thin intergranular films and solid-state activated sintering in nickel-doped tungsten, Acta Materialia 55(9) (2007) 3131-3142.

[31] J. Luo, Stabilization of nanoscale quasi-liquid interfacial films in inorganic materials: A review and critical assessment, Critical Reviews in Solid State and Materials Sciences 32(1-2) (2007) 67-109.

[32] J.F. Shackelford, Y.-H. Han, S. Kim, S.-H. Kwon, CRC materials science and engineering handbook, CRC press2016.

[33] X.M. Shi, J. Luo, Developing grain boundary diagrams as a materials science tool: A case study of nickel-doped molybdenum, Physical Review B 84(1) (2011).

[34] N.X. Zhou, J. Luo, Developing grain boundary diagrams for multicomponent alloys, Acta Materialia 91 (2015) 202-216.

[35] R.H.R. Castro, B.B. Wang, The Hidden Effect of Interface Energies in the Polymorphic Stability of Nanocrystalline Titanium Dioxide, Journal of the American Ceramic Society 94(3) (2011) 918-924.

[36] N. Eustathopoulos, M.G. Nicholas, B. Drevet, Wettability at high temperatures, Elsevier1999.

[37] H. Bakker, Enthalpies in alloys, Miedema's semi-empirical model, Trans. Tech. Publications (1998) 1-78.

[38] J. Luo, X.M. Shi, Grain boundary disordering in binary alloys, Applied Physics Letters 92(10) (2008) 3.

[39] H. Nishiura, R.O. Suzuki, K. Ono, L.J. Gauckler, Experimental phase diagram in the Ag-Cu_2O-CuO system, Journal of the American Ceramic Society 81(8) (1998) 2181-2187.

Chapter 3. Flash Sintering Activated by Bulk Phase and Grain Boundary Complexion Transformations

3.1. Introduction

Flash sintering, a novel sintering technology invented by Professor Raj and his colleagues [1, 2], has attracted significant scientific and technological interests. Because the densification can occur in seconds at much reduced furnace temperatures, the flash sintering technology has a great potential for significant time, cost, and energy savings. Flash sintering has been applied to various materials, including yttria-stabilized zirconia (YSZ), SiC, $BaTiO_3$, CeO_2, $MgAl_2O_4$, and ZnO [3-13]. Fundamental studies have been conducted to probe the cause of the flash initiation [8, 14-18], the mechanisms of rapid densification [8, 19, 20], and the effects of electric fields on phase transformation and microstructural evolution [8, 21-26]. Flash sintering is a multi-physics process that involves ultrafast temperature rise (often on the order of 100 °C/s), electric field effects, and far-from-equilibrium rapid microstructure evolution; thus, a diversifying spectrum of phenomena can occur [8, 9, 11, 24-37].

Sintering aids are often used to promote densification at reduced temperatures in conventional sintering via forming a small amount of liquid phases (in so-called “liquid-phase sintering”) [38-40] or nanoscale premelting like intergranular films (IGFs) (in so-called solid-state “activated sintering” that can occur below the bulk solidus curve) [41-50]. In a broader perspective, recent studies showed that grain boundary complexions (a.k.a. interfacial phases that are

thermodynamically two dimensional) [51] can often form and affect the sintering processing (e.g., lowering the onset of sintering via forming premelting like IGFs [41, 42, 44-46]), microstructural evolution [51-55], and the final mechanical, electrical, and thermal properties [51, 56, 57]. The possible roles of such grain boundary complexions in flash sintering have been discussed by Todd *et al*. [58] and Harmer *et al*. [52], but have been neither confirmed nor systematically investigated experimentally. This motivated us to dope ZnO with Bi_2O_3, which is known to promote the formation of premelting like IGFs (below the eutectic temperature, $T_{eutectic}$) and/or a small fraction of a wetting liquid phase (above the $T_{eutectic}$) to enhance conventional sintering [41, 59], to investigate their possible roles in the flash sintering in this current study.

Several independent studies carried out at UCSD [15], Oxford [14], and U. Penn. [16] collectively demonstrated that natural thermal runaways can trigger flash sintering. Here, we used “natural” thermal runaway to refer to the case that results from an Arrhenius increasing of the specimen conductivity with increasing temperature. Quantitative models have also been developed to show that predicted thermal runaway temperatures are consistent with the observed flash initiation temperatures in a broad range of materials examined [14-16, 19, 60-62]. Yet, these successes do not rule out the alternative possibilities that, in certain systems, the occurrence of another physical phenomenon, e.g., an avalanche of nonequilibrium defects or a bulk phase transformation or an interfacial phase-like (complexion) transformation, can result in a sudden increase in the specimen conductivity to subsequently trigger flash sintering. In such a case, a “forced”

(instead of “natural”) thermal runaway will be a secondary (instead of the primary) cause that induces the flash sintering. Here, we report, for the first time to our knowledge, such a case in Bi_2O_3-doped ZnO.

Specifically, this current study investigated and compared Bi_2O_3 *vs.* Al_2O_3 doping effects on the flash sintering of ZnO. In 0.5 mol. % Bi_2O_3-doped ZnO, we found that bulk/interfacial transformations could rapidly increase the specimen conductivity nonlinearly (above the linear Arrhenius extrapolation) to initiate flash sintering with low and median initial applied electric fields ($E_{initial}$). At a low $E_{initial}$ of 100 V/cm, the flash sintering was triggered when the estimated specimen temperature was near the bulk eutectic temperature (~740 °C). Interestingly, increasing $E_{initial}$ to 300 V/cm further activated the flash sintering at a sub-eutectic specimen temperature through the enhanced interfacial conductivity in the nanometer-thick IGFs (i.e., a quasi-liquid complexion thermodynamically stabilized at grain boundaries below the bulk eutectic temperature). Moreover, a high $E_{initial}$ of 800 V/cm resulted in a natural thermal runaway, prior to the formation of the premelting like grain-boundary complexion. In contrast, Al_2O_3 doping increased the conductivity of ZnO to promote flash sintering via reducing the natural thermal runaway temperature. We showed that this series of diversifying and scientifically interesting observations can be fully elucidated within one consistent physics-based theoretical framework and quantitively explained related models.

In addition, Al_2O_3 has higher solid solubilities in ZnO than Bi_2O_3 [63-66] to form a substantial amount of aliovalent $Al_{Zn}^{\bullet}$ defects. Here, we further discovered

fast field-induced migration of aliovalent $Al_{Zn}^{\bullet}$ cations during the flash sintering, which represents an electric field effect on far-from-equilibrium, rapid microstructural evolution occurred in the flash sintering.

3.2. Experimental

3.2.1. Materials synthesis and Sintering

ZnO powder (>99.99% purity, Sigma Aldrich) and 0.5 mol. % of Bi_2O_3 powder (≥99.8% purity, 90-210 nm particle size; Sigma Aldrich) were mixed in an yttria-stabilized zirconia vial with a small amount of isopropyl alcohol. All powders were subsequently planetary ball milled for 10 hours, dried in an oven at 80 °C for 12 hours, and calcined at 600 °C for two hours inside an alumina crucible on a Pt foil in air. The 1.6 mol. % (1 wt. %) Al_2O_3-doped ZnO powder (99.95+% purity, ~15 nm particle size) was purchased from US Research Nanomaterials, Inc.

The powders were uniaxially pressed at ~300 MPa to form a pellet with a dimension of a ¼-inch diameter and ~1-mm thickness. Platinum was sputtered on both sides of the green specimens using a Denton Discovery 18 Sputter. The sides of the sputtered specimens were slightly grounded by SiC papers after sputtering.

Flash sintering experiments were conducted with an initial electric field of 100 V/cm, 300 V/cm, or 800 V/cm. The applied voltage was kept at constant while ramping the furnace at a constant heating rate of 5 °C per minute until a flash occurred, at which point the system was switched from the voltage-control to a current-control mode with a preset maximum current limit of 1 A (corresponding to the maximum current density of ~39 mA/mm^2). The electric power source and

furnace were shut down 30 seconds after the occurrence of the flash. The specimens were cooled within the furnace. More details about the equipment set up and the experiments can be found in an earlier publication [19].

In addition to monitoring the specimen conductivity (prior to the start of the flash) in all flash sintering experiments, the conductivity of a ZnO + 0.5 mol. % Bi_2O_3 green specimen was measured in the same equipment setup using a high-precision digital multimeter (Tektronix DMM 4050, Beaverton, OR, USA) when the temperature was increased from room temperature to 1200 °C at 5 °C/min (identical to the ramp rate used in the flash sintering experiments) to assess the specimen conductivity in a large temperature range with a high accuracy.

3.2.2. Material characterization

The flash-sintered specimens were characterized by using an ultra-high-resolution scanning electron microscope (UHR SEM, FEI, Hillsboro, OR) equipped with energy dispersive X-ray spectroscopy (EDX, Oxford Instrument, UK). Transmission electron microscopy (TEM) specimens were prepared by using a Scios Dual Beam FIB/SEM system (FEI, Hillsboro, OR). High-resolution TEM (HRTEM) characterization of the grain boundary structures was conducted by using a JEOL 2800 microscope operated at 200 kV. In addition to flash-sintered specimens described above, a ZnO + 0.5 mol. % Bi_2O_3 specimen was equilibrated at 700 °C for 24 hours in air and then air quenched to room temperature for TEM characterization. Specifically, HRTEM was used to characterize the liquid-like IGFs

formed in both (equilibrated) isothermally-annealed and (presumably non-equilibrium) flash-sintered specimens for comparison.

3.3. Results and Discussion

3.3.1. Doping Effects on the Conductivity and Flash Sintering: Al_2O_3 *vs.* Bi_2O_3

The measured conductivity (in a logarithmic scale) *vs.* the reciprocal of the estimated absolute specimen temperature curves for undoped, Bi_2O_3-doped, and Al_2O_3-doped ZnO green specimens (i.e., un-sintered but compacted powder pellets; noting that the doped powders had been annealed/homogenized at 600 °C for two hours) are shown in Fig. 3.1. These conductivity measurements were conducted for the low-temperature regime before sintering would take place. Here, the difference between the specimen and furnace temperatures (that is small typically before the flash) was estimated by the black body radiation model [75].

On the one hand, Al_2O_3 doping increased the conductivity of ZnO (Fig. 3.1), which is well known (as Al_2O_3-doped ZnO is a transparent conductor). On the other hand, Bi_2O_3 doping decreased the conductivity of ZnO in this low-temperature region (Fig. 3.2; noting that the conductivity would increase abruptly near and above the bulk eutectic temperature, which will be discussed later and shown in Fig. 3.6(a)). Consistently, Al_2O_3 doping promoted, while Bi_2O_3 doping suppressed, the flash sintering, as shown in Fig. 3.2 and Table 1.

Fig. 3.2 shows the dissipating electric power density versus furnace temperature in these three specimens, where the initial electric field was set at 300 V/cm and current limit was set at 1 A (~39 mA/mm^2). The onset flash sintering

temperature (furnace T_F) in undoped ZnO was 628 °C; it decreased to (T_F =) 570 °C for Al_2O_3-doped ZnO because of the increased conductivity, while it increased to (T_F =) 696 °C for Bi_2O_3-doped ZnO because of the reduced conductivity (Fig. 3.2 *vs.* Fig. 3.1).

The relative densities of the flash-sintered undoped, Bi_2O_3-doped, and Al_2O_3-doped ZnO specimens (with the identical processing parameters of I_{max} = 1 A and $E_{initial}$ = 300 V/cm) were measured to be 97.2%, 89.2%, and ~69%, respectively. Since the focus here is to examine the doping effects on the flash initiation, particularly the possible influences of bulk phase transformation and grain boundary phase-like complexion transition, we kept the same flash conditions for undoped, Bi_2O_3-doped, and Al_2O_3-doped ZnO for a fair comparison (instead of optimizing the conditions individually for achieving high densities for each case). Consequently, the Al_2O_3-doped ZnO specimen has a low relative density because the specimen has a significantly higher conductivity in comparison with the other two, thereby resulting in a lower steady-state specimen temperature during flash sintering. By increasing the current limit I_{max} (from 1 A) to 4 A, however, Al_2O_3-doped ZnO can also be flash-sintered to ~97% of the theoretical density.

3.3.2. Undoped and Al_2O_3-doped ZnO: Natural Thermal Runways

Following our prior procedure [15], the relationship between the temperature-dependent conductivity of the green (compacted powder) specimens was fitted into an empirical Arrhenius equation $\sigma(T) = \sigma_0 e^{-\frac{Q}{kT}}$, where k is the Boltzmann constant, Q is the activation energy, and σ_0 is a pre-exponential

constant, for each case. The linear regressions of $\log(\sigma)$ *vs.* 1/*T* (Fig. 3.1) for undoped and Al_2O_3-doped ZnO produced activation energies of 1.02 eV and 1.53 eV, respectively, where the linear correlation coefficients R^2 are higher than 99% in both cases. The $\log(\sigma)$ *vs.* 1/*T* curve is less linear for the 0.5 mol. % Bi_2O_3-doped ZnO specimen in this temperature region (Fig. 3.1), where a linear regression gave an R^2 of ~94% with the best fitted activation energy of 1.81 eV. The nonlinearity for the Bi_2O_3-doped ZnO increases further at higher temperatures, which will be discussed later.

The Arrhenius temperature-dependent conductivity function $\sigma(T)$, which is an extrapolation of the measurements of the un-sintered specimen at low temperatures, was subsequently used to predict the thermal runaway condition following a model that we proposed previously [14, 15]. Here, a balance between the heat generation from Ohmic (Joule) heating and heat dissipation from blackbody radiation determines the specimen temperature:

$$\sigma(T_S)E^2V_S = A_S\varepsilon\sigma_{Stefan}(T_S^4 - T_F^4), \quad (1)$$

where E (= $E_{initial}$) is the electric field, V_S is the volume of the specimen, and T_S and T_F are the specimen (S) and furnace (F) temperatures, respectively, $\sigma(T_S)$ is the specimen conductivity, A_S is the surface area of the specimen, ε is the emissivity, and σ_{Stefan} is the Stefan–Boltzmann constant. A coupled thermal and electric runaway predicted from the Arrhenius extrapolation of the specimen conductivities measured at low temperatures (referred to as a “natural thermal runaway” for brevity hereafter) will take place if there is more heat generated with increasing

temperature than that can be dissipated:

$$E^2 \left.\frac{d\sigma}{dT}\right|_{T_S} \frac{V_S}{A_S} > 4\varepsilon\sigma_{Stefan} T_S^3 \ , \qquad (2)$$

Noting that we divide both sides of Eq. (1) by A_S so that all specimen related parameters are on the left side in Eq. (2).

Eq. (2) suggests a graphical construction method to find the natural thermal runaway condition, as schematically illustrated in Fig. 3.3. Here, the intersection point of differential heat generation and dissipation rates (both normalized to per unit the specimen surface area, A_S), which are the left and right sides of Eq. (2), determines the specimen temperature (T_S) that produces a natural thermal runaway. Subsequently, the corresponding furnace temperature (T_F) can be calculated based on the black body radiation model.

Via this model and the associated graphical construction method (Fig. 3.3), the furnace temperatures at the natural thermal runaways for undoped and Al_2O_3-doped ZnO specimens ($E_{initial}$ = 300 V/cm) were determined to 628 °C and 564 °C, respectively, using $\sigma(T)$ functions extrapolated from the measured conductivities data shown in Fig. 3.1. Experimentally, we observed onset flash temperatures to be 628 °C for undoped ZnO and 570 °C for Al_2O_3-doped ZnO, respectively. The differences are small (0 °C and 6 °C, respectively). Thus, we conclude the flash sintering in undoped and Al_2O_3-doped ZnO specimens was triggered by natural thermal runaways.

For the Bi_2O_3-doped ZnO specimen at the same $E_{initial}$ = 300 V/cm, this model would predict a natural runaway temperature (T_F = 740 °C) from a simple

Arrhenius extrapolation of the specimen conductivities measured at low temperatures. However, this predicted natural runaway temperature of T_F = 740 °C is 44 °C higher than the observed onset flash temperature (696 °C). This discrepancy is caused by the formation of premelting like IGFs in Bi_2O_3-doped ZnO, as we will discuss subsequently in §3.5.

3.3.3. Field-Driven Fast Migration of Aliovalent Cations

Fig. 3.4 shows the microstructure of the flash-sintered Al_2O_3-doped ZnO specimen. Notably, aluminum (Al) enriched “white” particles accumulated in the negative electrode (cathode) side (Fig. 3.4(e)).

Specifically, the enlarged cross-sectional SEM images in Fig. 3.4(e) *vs.* Fig. 3.4(c) reveal “white” particles near the negative electrode (cathode), which are absent in the positive electrode (anode). EDX analyses (Fig. 3.4(f) *vs.* Fig. 3.4(g)) further showed that these “white” particles are Al enriched. The compositions of these white particles were measured to be ~54% O, ~24% Al, and ~22% of Zn. The actual Al content can be even higher considering the possible beam spreading as the particles are sub-micrometer sizes. In comparison, the composition for the normal “dark” particles was measured by EDX to be ~49% O, ~3% Al, and ~ 48% Zn, which is close to our nominal powder composition (1.6 mol. % Al_2O_3 doped ZnO). Presumably, the white particles are a Zn-Al-O compound, most likely the spinel-structured $ZnAl_2O_4$ [64], that precipitated during the flash sintering and/or when the specimen was cooled down.

The specimen temperature during the steady-state stage of the flash

sintering was estimated to be 930 °C. It is known that Al_2O_3 has ~0.3 mol. % solubility in ZnO to form charged $Al_{Zn}^{\bullet}$ defects in the temperature range of 850 to 1200 °C [64]. Thus, we hypothesize that the applied electric field/current moved charged $Al_{Zn}^{\bullet}$ defects from the positive to the negative electrode side during the flash sintering, which subsequently precipitated as Al-enriched compound particles near the negative electrode side. This represents a new discovery of ultrafast, field-driven, asymmetrical microstructural evolution during the flash sintering. It is remarkable that this whole process occurred within ~30 seconds.

An asymmetrical microstructure was also observed for the flash-sintered 0.5 mol. % Bi_2O_3-doped ZnO sample. Fig. 3.5 shows the cross-sectional SEM images of flash-sintered Bi_2O_3-doped ZnO ($E_{initial}$ = 300 V/cm). The average grain size at the negative electrode (cathode) was measured to be 448 ± 28 nm, which approximately doubles that measured for positive electrode (anode) side (212 ± 16 nm).

On the one hand, Bi_2O_3 has a much lower solubility in ZnO (< 0.05 mol. %), which differs from Al_2O_3. Thus, the field-driven migration of substitutional aliovalent cations, such as that observed for Al_2O_3-doped ZnO, was not observable here in Bi_2O_3-doped ZnO due to the limited solid solubility. On the other hand, it is known that the ZnO-Bi_2O_3 solid-liquid two-phase material (above the eutectic temperature) can be used as oxygen ion transport membranes [76], where the intergranular Bi_2O_3-enriched liquid phase serves as oxygen ionic conductor. Thus, during the flash sintering of Bi_2O_3-doped ZnO, the high current density and electric field can

induce strong polarization of oxygen defects, which may lead to the asymmetrical microstructure observed (Fig. 3.4). Further investigation should be conducted to probe the detailed underlying mechanism of the observed enhanced grain growth at the cathode side in Bi_2O_3-doped ZnO.

Electric field induced asymmetric microstructure has also been observed in polycrystalline or bi-crystal $SrTiO_3$ [67-70], $BaTiO_3$,[71, 72], and YSZ [73, 74]. Electromigration of point defects has been proposed or experimentally characterized in these materials. In this work, bulk point defect ($Al_{Zn}^{\bullet}$) was unequivocally characterized to reveal the fast migration during flash sintering, which is similar to the Electromigration of oxygen ion and oxygen vacancies in $SrTiO_3$ and YSZ. However, the possibility of grain boundary oxygen defects polarization and their effects on microstructure evolution need further investigation

3.3.4. Bi_2O_3-doped ZnO under Low $E_{initial}$: Bulk Eutectic Induced Flash

In addition to the natural thermal runaways that can be predicted from the Arrhenius extrapolation of the measured conductivities of the green specimen, here we report a second possibility that the occurrence of a bulk eutectic reaction could trigger flash sintering in 0.5 mol. % Bi_2O_3-doped ZnO via causing a sudden increase in the specimen conductivity (in the eutectic liquid), as a temperature lower than the predicted natural thermal runaway.

Specifically, when a low $E_{initial}$ of 100 V/cm is applied, the specimen temperature for a natural thermal runaway predicted from an Arrhenius extrapolation from the measured conductivities of the green specimen would be

1005 °C (Fig. 3.6(b)). However, flash sintering initiated at the estimated specimen temperature T_S = 742 °C (Fig. 3.7), which is about the bulk eutectic temperature (~740 °C). Presumably, the formation of the Bi_2O_3-enriched, ionic, eutectic liquid caused a sudden increase in the specimen conductivity, thereby triggering the flash sintering via a "forced" thermal runaway.

To confirm the above hypothesis, the electrical conductivity of a 0.5 mol. % Bi_2O_3-doped ZnO specimen was measured when the specimen was heated from room temperature to 1200 °C, and subsequently cooled down. The measured $\log(\sigma)$ *vs.* $1/T$ curves are shown in Fig. 3.6(a). During the heating, a conductivity transition (i.e., an abrupt increase in measured conductivity) was observed between 690 °C and 840 °C, which is presumably due to the bulk eutectic reaction (that forms a conducting Bi_2O_3-based mixed conducting liquid [77]) and associated formation of Bi_2O_3-enriched, liquid-like, nanoscale IGFs at ZnO grain boundaries (Fig. 3.8) [41, 65]. During the cooling, the $\log(\sigma)$ vs $1/T$ curve mostly remained linear (as the Bi_2O_3-enriched IGFs retained to room temperature). The corresponding predicted T_S (for three different $E_{initial}$'s) from the natural thermal runaway model (Fig. 3.6(b)) were labeled in Fig. 3.6(a). These predictions were from the Arrhenius extrapolation (the dash line in Fig. 3.6(a)) of the conductivities of the green specimen (prior to the occurrence of a conductivity transition). Thus, the natural thermal runaways predicted from the Arrhenius extrapolation did not account for the effect of this conductivity transition.

We should further note that conductivity transition shown in Fig. 3.6(a) was measured during furnace heating (at 5 °C/min) and the actual conductivity

transition profile should also depend on the heating rate, which was much faster in the flash sintering and should also depend on $E_{initial}$.

When a low $E_{initial}$ of 100 V/cm was applied, the specimen experienced a significant increase of conductivity (~ 10 times higher above the Arrhenius extrapolation) before the onset of flash at T_S = 742 °C, which triggered a "forced" thermal runway that is > 250 °C lower than predicted T_S for a natural thermal runaway (from an Arrhenius extrapolation). Thus, the experimental observation (and the discrepancy between the onset flash and the natural thermal runaway predicted from an Arrhenius extrapolation) can be fully understood. In this case, the bulk eutectic reaction at ~740 °C triggered a "forced" thermal runaway, and a flash event thereafter, via forming a conducting, Bi_2O_3-enriched, ionic liquid.

3.3.5. Bi_2O_3-doped ZnO under Intermediate $E_{initial}$: Interfacial Transition Induced Flash

Moreover, we observed that further increasing $E_{initial}$ initiated flash sintering at a sub-eutectic specimen temperature. When $E_{initial}$ was 300 V/cm, the estimated T_S for onset flash in the experiment was 696 °C (Fig. 3.7(a)); noting the stability is lost at > 696 °C as shown in Fig. 3.7(a), coincident with a sudden rise in the specimen conductivity as shown in Fig. 3.6(a). This observed onset flash specimen temperature is > 40 °C lower than the bulk eutectic temperature, but the specimen conductivity started to increase sharply beyond the linear Arrhenius extrapolation line at this temperature as shown in Fig. 3.6(a); here, we should note 696 °C is the nominal specimen temperature for the onset flash, which is defined as the middle

point in Fig. 3.7(a); the actual onset flash occurred in a short time period where the specimen temperature further increased beyond the middle point of T_S = 696 °C, after which the specimen temperature increased abruptly as shown in Fig. 3.6(a), before losing the stability to trigger the flash sintering. This was presumably resulted from the enhanced interfacial conductivity in the nanometer-thick, Bi_2O_3-based, liquid-like IGFs that are known to form a below the bulk eutectic temperature [41] (i.e., a premelting like complexion thermodynamically stabilized at ZnO grain boundaries).

It is interesting to note that this moderate increase in the interfacial conductivity of the specimen was insufficient to trigger a flash at the low $E_{initial}$ of 100 V/cm, but it became significant when $E_{initial}$ was increased to 300 V/cm. Presumably, a higher $E_{initial}$ requires a less significant non-linear increase in the specimen conductivity to trigger flash sintering via a “forced” thermal runaway. This is consistent with that the predicted T_S for a natural thermal runaway was 801 °C at 300 V/cm, much lower than the 1005 °C at 100 V/cm (Fig. 3.6(b)). Experimentally, we observed that the flash sintering initiated at 742 °C (approximately the bulk eutectic temperature) at the low $E_{initial}$ of 100 V/cm, but at a sub-eutectic temperature (696 °C) at the median $E_{initial}$ of 300 V/cm (Fig. 3.7).

To confirm the above hypothesis directly, we conducted further experiments to directly characterize the grain boundary structures responsible for the increased interfacial conductivity below bulk eutectic temperature in two types of specimens, which are discussed below.

First, a 0.5 mol. % Bi_2O_3-doped ZnO specimen was isothermally annealed

at 700 °C (40 °C below the bulk eutectic temperature) and air-quenched to preserve the grain boundary structures. Fig. 3.8(b) shows TEM and HRTEM images of Bi-enriched, liquid-like IGFs that are stabilized at ZnO grain boundaries, even below the bulk eutectic temperature. The IGFs formed in the specimen equilibrated at 700 °C were measured to be ~2 nm thick in this study. Prior studies already showed that the formation of such sub-eutectic, premelting like IGFs can enhance sintering [41, 45]. In this study, the formation of these Bi_2O_3-enriched, liquid-like, nanoscale IGFs presumably increased the interfacial conductivity below the bulk $T_{eutectic}$ to trigger the flash sintering under the intermediate $E_{initial}$ of 300 V/cm.

Second, we further confirmed the ultra-fast formation of liquid-like IGFs during flash sintering directly. Specifically, we quenched a 0.5 mol. % Bi_2O_3-doped ZnO specimen after being flash sintered for 20 seconds. Fig. 3.9 shows two low-magnification and three high-magnification TEM images of the grain boundaries in this flash-sintered specimen. The liquid-like IGFs observed in the flash-sintered specimen are relatively thinner than those observed in the specimen equilibrated at 700 °C. Presumably, these liquid-like IGFs did not form at a thermodynamic equilibrium due to the ultrafast flash sintering process. Nonetheless, this result directly confirmed that such liquid-like IGFs could form very quickly (in <20 seconds) during the flash sintering, which is indeed interesting.

3.3.6. Bi_2O_3-doped ZnO under High $E_{initial}$: A Natural Thermal Runaway

If the above explanations and hypotheses (discussed in §3.4 and §3.5) are

correct, we should be able to further increase $E_{initial}$ to allow the occurrence of a natural thermal runaway prior to the bulk eutectic reaction and interfacial premelting like transition. Indeed, we were able to confirm this prediction by our experiment. When we further increased $E_{initial}$ to 800 V/cm, our model predicted a natural thermal runaway at a specimen temperature T_S = 677 °C (>70 °C below the bulk eutectic temperature), as shown in Fig. 3.6(b). Indeed, we observed that the onset flash took place at an estimated specimen T_S of 670 °C in our experiment (Fig. 3.7).

This agreement finally confirmed that the experimental observations of all five cases (un-doped and Al_2O_3-doped ZnO at $E_{initial}$ = 300 V/cm, as well as Bi_2O_3-doped ZnO at $E_{initial}$ =100, 300, and 800 V/cm, respectively) can be fully explained within one consistent theoretical framework.

3.4. Conclusions

We investigated Al_2O_3 *vs.* Bi_2O_3 doping effects on the flash sintering of ZnO. On the one hand, Al_2O_3 doping increased the specimen conductivity to promote flash sintering. The onset flash occurred as natural thermal runaway in both un-doped and Al_2O_3-doped ZnO at $E_{initial}$ of 300 V/cm. We also made a new observation of ultrafast field-induced migration of aliovalent cations during the flash sintering of Al_2O_3-doped ZnO.

On the other hand, Bi_2O_3 doping decreased the specimen conductivity to delay the occurrence of flash sintering to higher temperatures, while it also led to a eutectic reaction and associated premelting-like grain boundary transition that

can abruptly increase the specimen conductivity with increasing temperature. Consequently, the onset flash was initiated by a bulk eutectic reaction at a low $E_{initial}$ of 100 V/cm and by premelting like grain boundary transition at an intermediate $E_{initial}$ of 300 V/cm, respectively, in 0.5 mol. % Bi_2O_3-doped ZnO. When we further increased $E_{initial}$ to 800 V/cm, a natural thermal runaway still took place before the occurrence of interfacial and bulk transformation, as predicted by the Arrhenius extrapolation.

Notably, we demonstrated that all five cases discussed above can be fully explained within one consistent theoretical framework.

Most significantly, this study has uncovered, for the first time to our knowledge, the possibility that a bulk phase transformation and/or interfacial (phase-like) complexion transformation can trigger flash sintering (via “forced,” instead of natural, thermal runaway). This new discovery thus suggests a new direction to tailor the flash sintering process.

Chapter 3, in part, is a reprint of the material “Flash Sintering Activated by Bulk Phase and Grain Boundary Complexion Transformations” in preparation, Y. Zhang, J. Nie, and Jian Luo. Part of the AZO experiments was carried out by Dr. Yuanyao Zhang. The dissertation author was the primary investigator and author of this paper.

Table 3.1 Summary of the key results for the flash sintering of undoped, Al_2O_3-doped, and Bi_2O_3-doped ZnO. The thermal runaway conditions were predicted from the Arrhenius extrapolation of the conductivities measured at low temperatures from the (un-sintered) green specimens. The predicted natural thermal runaway conditions are consistent with the experimentally-observed onset flash temperatures for undoped and Al_2O_3-doped ZnO. For Bi_2O_3-doped ZnO, the occurrence of a bulk phase (eutectic) transformation and an associated interfacial phase-like (premelting type complexion) transformation can cause a nonlinear rise in the specimen conductivity, thereby triggering a "forced" runaway (prior to the occurrence of a natural thermal runaway) at the initial electric field of 100 or 300 V/cm. At a higher initial field of 800 V/cm, a natural thermal runaway still took place before the occurrence of interfacial and bulk transformation. All observations of five cases can be fully explained within one consistent theoretical framework.

Specimens	Initial Electric Field $E_{initial}$ (V/cm)	Activation Energy for Low-T Conductivity (eV)	R^2	Predicted Thermal Runaway Specimen $T_S \rightarrow$ Estimated Furnace T_F		Observed Onset Flash Furnace T_F $\rightarrow$ Estimated Specimen T_S		The Cause for the Onset Flash
				T_S (°C)	T_F (°C)	T_F (°C)	T_S (°C)	
Un-doped ZnO	300	1.02	> 0.99	777	~628	628	747	Natural Thermal Runaway
1.6 mol. % Al_2O_3-doped ZnO	300	1.53	> 0.99	610	~564	570	607	Natural Thermal Runaway
0.5 mol. % Bi_2O_3-doped ZnO	300	1.89	0.94	801	~740	689	~696	GB Transition $\rightarrow$ Runaway
	100	1.81	0.9	1005	~960	734	~742	~ Bulk Eutectic $\rightarrow$ Runaway
	800	1.79	0.99	677	~607	613	~670	Natural Thermal Runaway

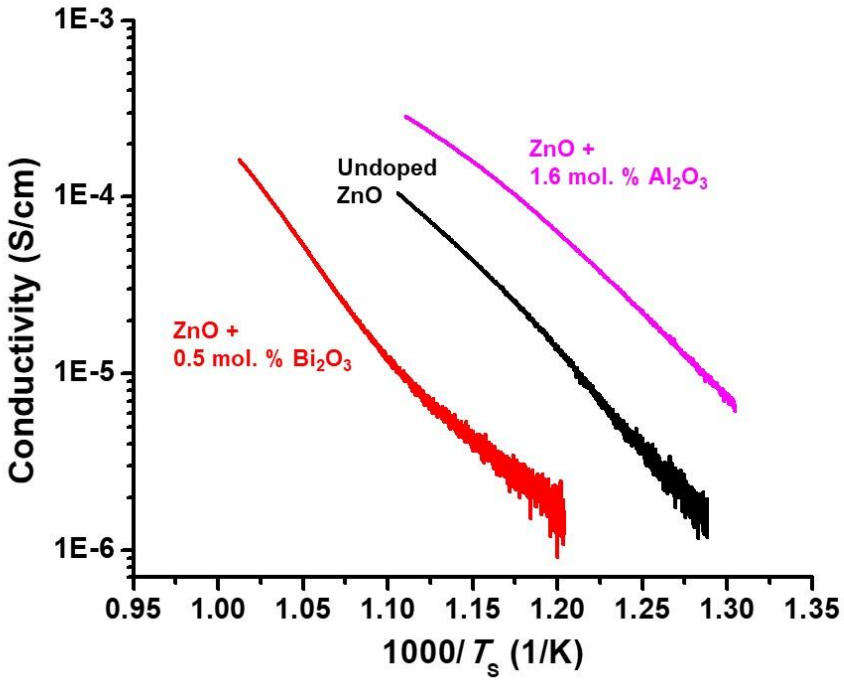

Figure 3.1 Logarithmic measured electric conductivity *vs.* the reciprocal of the absolute specimen temperature curves for undoped, 0.5 mol. % Bi_2O_3-doped, and 1.6 mol. % Al_2O_3-doped ZnO green specimens.

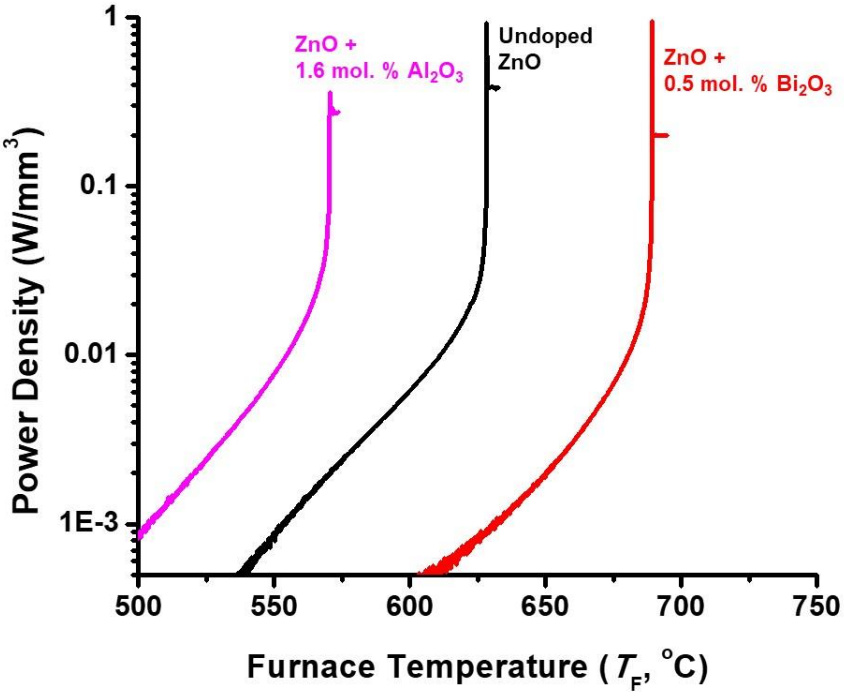

Figure 3.2 Measured dissipating electric power density (in a logarithmic scale) *vs.* furnace temperature curves for the flash sintering of undoped ZnO, 0.5 mol. % Bi_2O_3 doped ZnO, and 1.6 mol. % Al_2O_3-doped ZnO (AZO), where the initial electric field was set to be 300 V/cm and the maximum current limit was set to 1 A ($J_{max} \approx$ 39 mA/mm^2).

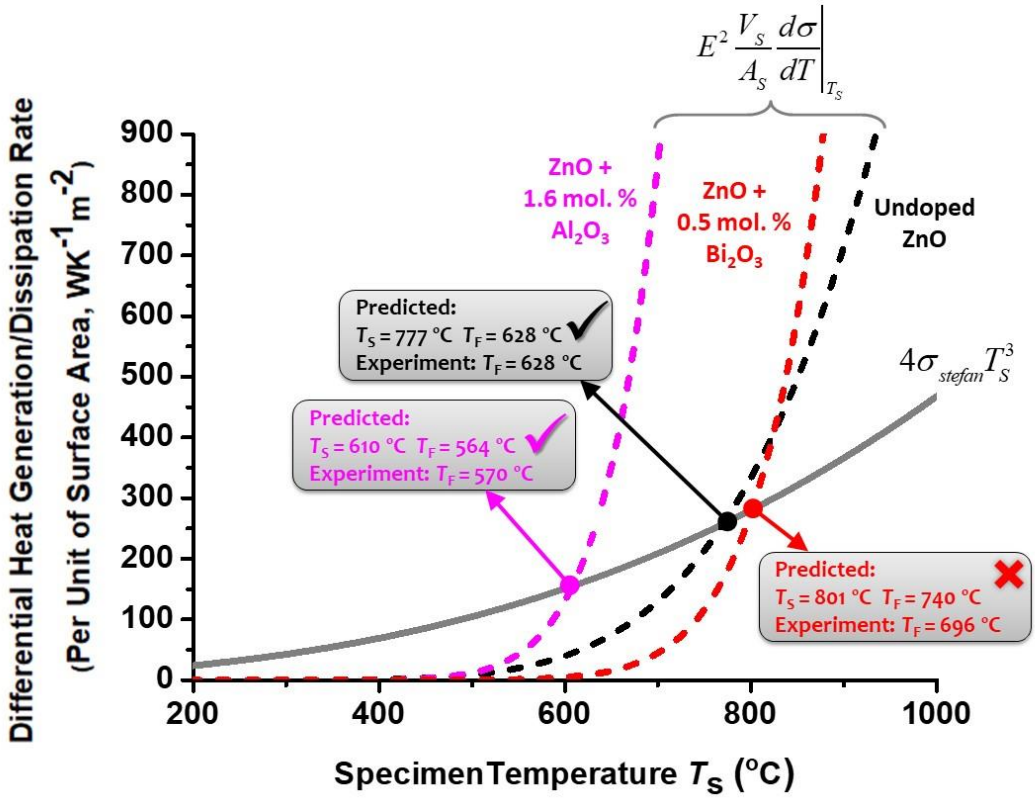

Figure 3.3 Calculated differential heat generation and dissipation rates (normalized to per unit surface area) *vs.* specimen temperature curves for undoped, 0.5 mol. % Bi_2O_3-doped, and 1.6 mol. % Al_2O_3-doped ZnO specimens. The initial electric field was set to be 300 V/cm in each case. The thermal runaway condition can be determined by the intersection of differential heat generation and dissipation rates. The predicted thermal runaway temperatures are consistent with the observed onset flash temperatures for undoped and Al_2O_3-doped ZnO, but not for the Bi_2O_3-doped ZnO. A further investigation offers a clear explanation for the apparent discrepancy in the latter case; the natural thermal runaway predicted from the Arrhenius extrapolation of specimen conductivities measured at low temperatures would occur at a specimen temperature of 801 °C for the Bi_2O_3-doped ZnO; however, a flash actually occurred at a lower specimen temperature near the ZnO-Bi_2O_3 eutectic temperature of 740 °C, where there was an abrupt increase in the specimen conductivity (beyond the Arrhenius extrapolation) as shown in Fig. 3.6(a).

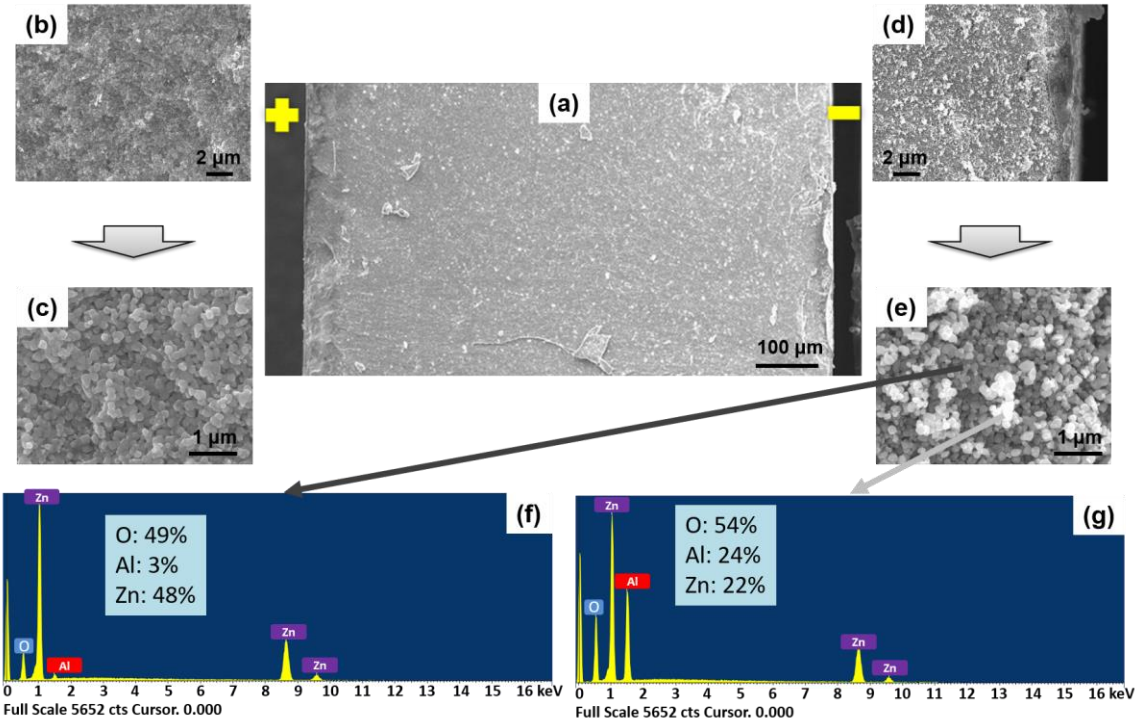

Figure 3.4 (a) Cross-sectional SEM image of Al_2O_3-doped ZnO, along with enlarged SEM images at the (b, c) anode and (d, e) cathode sides. (f, g) EDX quantitative elemental analyses of the “dark particles” and the “white particles”. The compositional analysis clearly showed these “white particles” are Al-enriched. Most “white particles” enriched in Al were observed at the cathode side.

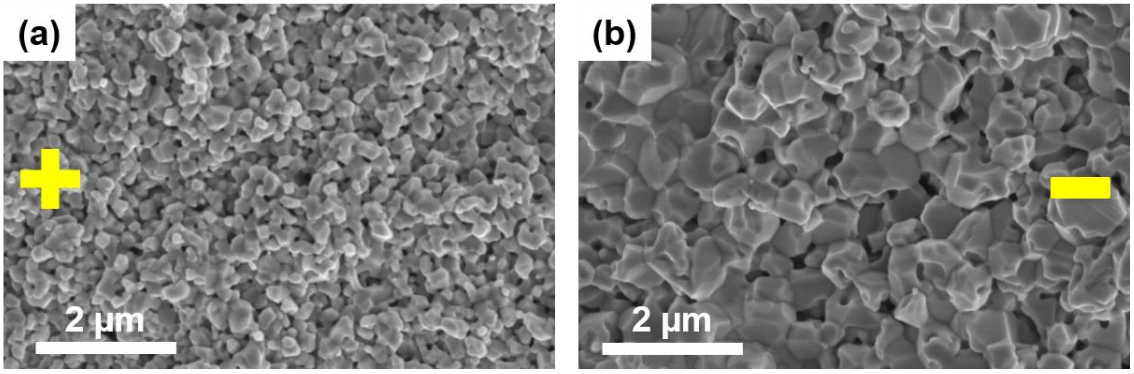

Figure 3.5 Cross-sectional SEM images at (a) anode and (b) cathode sides of a flash-sintered Bi_2O_3-doped ZnO specimen, where the initial electric field ($E_{initial}$) was set to be 300 V/cm and the maximum current limit was set to 1 A ($J_{max} \approx 39$ mA/mm^2).

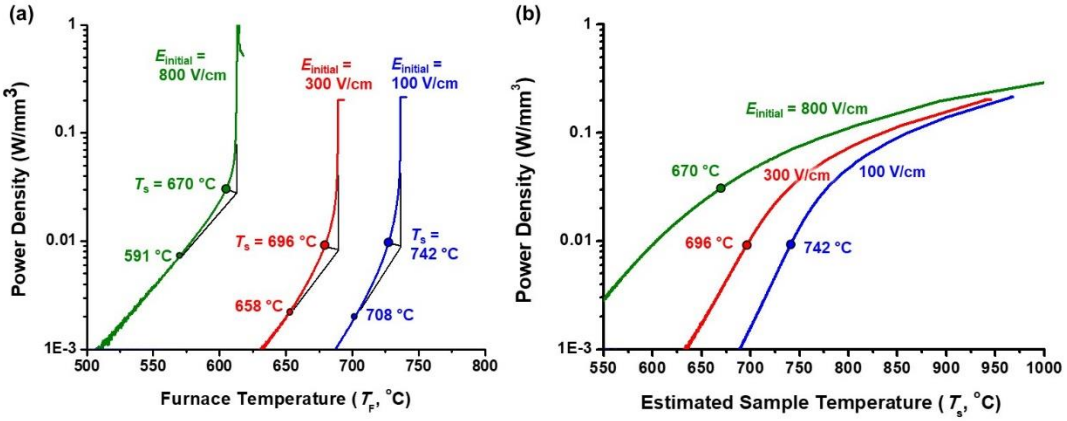

Figure 3.6 (a) Measured dissipating electric power density *vs.* (a) furnace temperature and (b) estimated specimen temperature curves for the flash sintering of 0.5 mol. % Bi_2O_3-doped ZnO specimens, where the initial electric field ($E_{initial}$) was set to be 100, 300, and 800 V/cm, respectively. For each case, two estimated specimen temperatures (T_S) are labelled: the start of the nonlinearity in the power density *vs.* furnace temperature curve and turning (middle) point as determined by an angle bisector of two tangent lines. The estimated T_S at the latter (turning points) are considered as the observed specimen temperatures at the onset flash, which are also labeled in panel (b) as well as Fig. 3.7 (a).

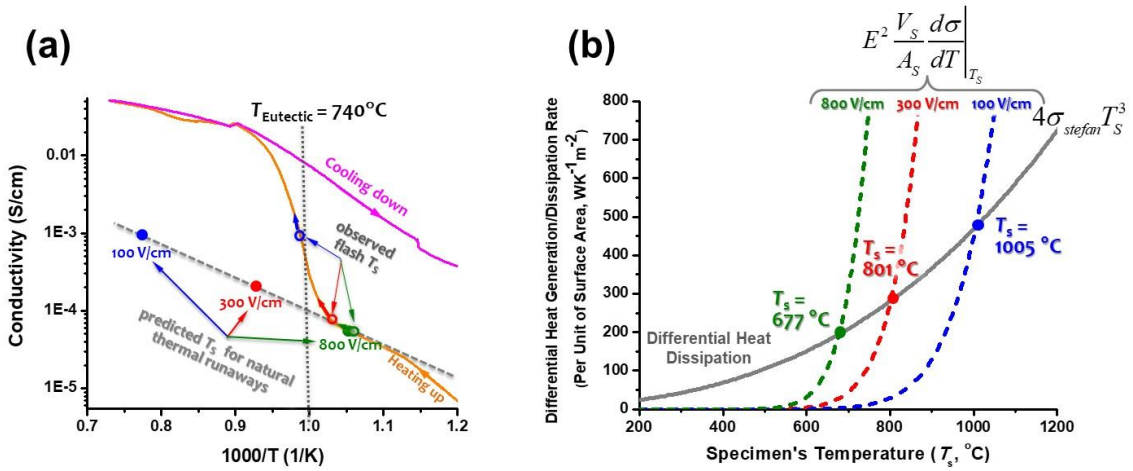

Figure 3.7 (a) Measured electric conductivity (in logarithmic scale) *vs.* the reciprocal absolute specimen temperature curves for a green specimen of ZnO + 0.5 mol. % Bi_2O_3 heated from room temperature to 1200 °C (the orange line) at a ramp rate of 5 °C/min, and subsequently cooled down (the pink line). The predicted specimen temperatures (T_S) at natural thermal runaways from the Arrhenius extrapolation from the measured low-temperature conductivities for $E_{initial}$ = 100, 300, and 800 V/cm, respectively, are indicated by the solid discs; the estimated specimen temperatures at the onset flash ("observed flash T_S") are also marked as open circles with arrows. (b) Calculated differential heat generation and dissipation rates (all normalized to per unit surface area) *vs.* specimen temperature curves for the flash sintering of ZnO + 0.5 mol. % Bi_2O_3 specimens with the initial electrical fields of 100, 300, and 800 V/cm, respectively. The thermal runaway conditions predicted from the Arrhenius extrapolations of specimen conductivities measured at low temperatures are determined by the intersections of differential heat generation and dissipation rates. Such predicted thermal runaway temperatures are higher than the experimental observed onset flash temperatures for $E_{initial}$ = 100 V/cm and 300 V/cm because of the nonlinear rise in specimen conductivity near the eutectic temperature. When we further increased $E_{initial}$ to 800 V/cm, the predicted thermal runaway occurred at T_S ~670 °C, before the nonlinear increase of the specimen conductivity, which agrees with the observed onset flash temperature.

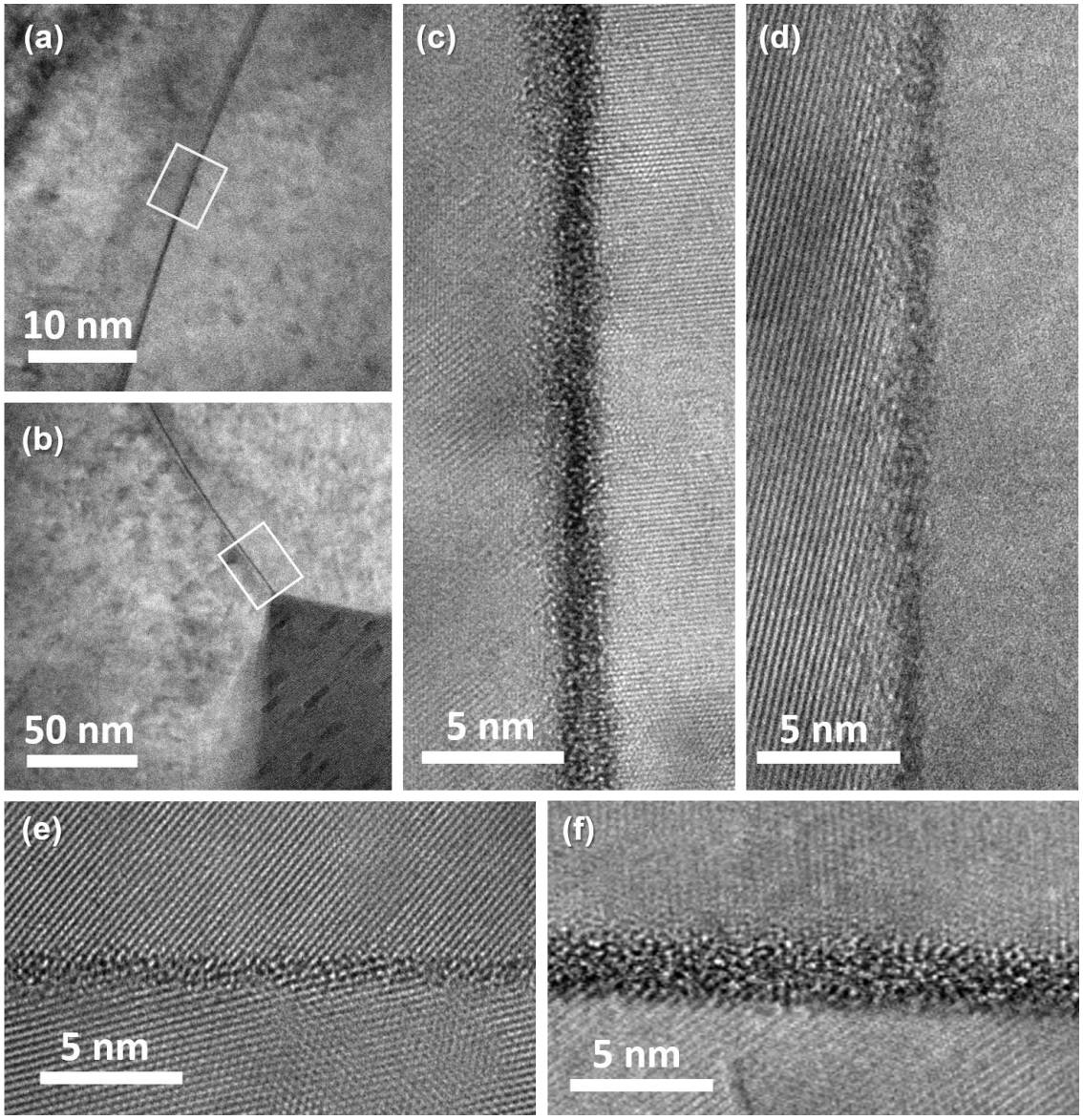

Figure 3. 8 (a - e) HRTEM images of a ZnO + 0.5 mol. % Bi_2O_3 specimen after flash sintered for 20 seconds where the initial electric field ($E_{initial}$) was set to be 300 V/cm and the maximum current limit was set to 1 A ($J_{max} \approx 39$ mA/mm^2). (c – e) High magnification grain boundary images, in which (c) and (d) correspond to the locations labelled in (a) and (b) respectively. (f) HRTEM image of a ZnO + 0.5 mol. % Bi_2O_3 specimen annealed at 700 °C and quenched in air as a reference, showing the formation of liquid-like Bi_2O_3-enriched intergranular film (IGF) stabilized at the ZnO grain boundary below the bulk eutectic temperature ($T_{eutectic}$ = 740 °C) where the bulk liquid is not yet stable, which explains the moderate increase of conductivity below the bulk eutectic temperature. IGFs also formed during flash sintering even in 20 seconds showing its fast kinetic.

References

[1] M. Cologna, B. Rashkova, R. Raj, Flash Sintering of Nanograin Zirconia in < 5 s at 850 °C, Journal of the American Ceramic Society 93(11) (2010) 3556-3559.

[2] M. Cologna, A.L. Prette, R. Raj, Flash-sintering of cubic yttria-stabilized zirconia at 750 °C for possible use in SOFC manufacturing, Journal of the American Ceramic Society 94(2) (2011) 316-319.

[3] M. Cologna, A.L.G. Prette, R. Raj, Flash-Sintering of Cubic Yttria-Stabilized Zirconia at 750 °C for Possible Use in SOFC Manufacturing, Journal of the American Ceramic Society 94(2) (2011) 316-319.

[4] E. Zapata-Solvas, S. Bonilla, P.R. Wilshaw, R.I. Todd, Preliminary investigation of flash sintering of SiC, Journal of the European Ceramic Society 33(13-14) (2013) 2811-2816.

[5] X.M. Hao, Y.J. Liu, Z.H. Wang, J.S. Qiao, K.N. Sun, A novel sintering method to obtain fully dense gadolinia doped ceria by applying a direct current, Journal of Power Sources 210 (2012) 86-91.

[6] R. Muccillo, E.N.S. Muccillo, M. Kleitz, Densification and enhancement of the grain boundary conductivity of gadolinium-doped barium cerate by ultra fast flash grain welding, Journal of the European Ceramic Society 32(10) (2012) 2311-2316.

[7] C. Schmerbauch, J. Gonzalez-Julian, R. Roder, C. Ronning, O. Guillon, Flash Sintering of Nanocrystalline Zinc Oxide and its Influence on Microstructure and Defect Formation, Journal of the American Ceramic Society 97(6) (2014) 1728-1735.

[8] J. Luo, The scientific questions and technological opportunities of flash sintering: From a case study of ZnO to other ceramics, Scripta Materialia 146 (2018) 260-266.

[9] M. Yu, S. Grasso, R. McKinnon, T. Saunders, M.J. Reece, Review of flash sintering: materials, mechanisms and modelling, Advances in Applied Ceramics 116(1) (2017) 24-60.

[10] M. Biesuz, V.M. Sglavo, Flash sintering of ceramics, Journal of the European Ceramic Society (2018).

[11] R. Todd, Flash sintering of ceramics: a short review, Proceedings of the IV Advanced Ceramics and Applications Conference, Springer, 2017, pp. 1-12.

[12] B. Yoon, D. Yadav, S. Ghose, R. Raj, Reactive flash sintering: MgO and α-Al_2O_3 transform and sinter into single-phase polycrystals of $MgAl_2O_4$, Journal of the American Ceramic Society 102(5) (2019) 2294-2303.

[13] X. Vendrell, D. Yadav, R. Raj, A.R. West, Influence of flash sintering on the ionic conductivity of 8 mol. % yttria stabilized zirconia, Journal of the European Ceramic Society 39(4) (2019) 1352-1358.

[14] R.I. Todd, E. Zapata-Solvas, R.S. Bonilla, T. Sneddon, P.R. Wilshaw, Electrical characteristics of flash sintering: thermal runaway of Joule heating, Journal of the European Ceramic Society 35(6) (2015) 1865-1877.

[15] Y. Zhang, J.I. Jung, J. Luo, Thermal runaway, flash sintering and asymmetrical microstructural development of ZnO and ZnO-Bi_2O_3 under direct currents, Acta Materialia 94 (2015) 87-100.

[16] Y.H. Dong, I.W. Chen, Onset Criterion for Flash Sintering, Journal of the American Ceramic Society 98(12) (2015) 3624-3627.

[17] J.G.P. da Silva, H.A. Al-Qureshi, F. Keil, R. Janssen, A dynamic bifurcation criterion for thermal runaway during the flash sintering of ceramics, Journal of the European Ceramic Society 36(5) (2016) 1261-1267.

[18] Y.Y. Zhang, J.Y. Nie, J. Luo, Effects of phase and doping on flash sintering of TiO_2, Journal of the Ceramic Society of Japan 124(4) (2016) 296-300.

[19] Y.Y. Zhang, J.Y. Nie, J.M. Chan, J. Luo, Probing the densification mechanisms during flash sintering of ZnO, Acta Materialia 125 (2017) 465-475.

[20] W. Ji, B. Parker, S. Falco, J.Y. Zhang, Z.Y. Fu, R.I. Todd, Ultra-fast firing: Effect of heating rate on sintering of 3YSZ, with and without an electric field, Journal of the European Ceramic Society 37(6) (2017) 2547-2551.

[21] S.K. Jha, J.M. Lebrun, R. Raj, Phase transformation in the alumina-titania system during flash sintering experiments, Journal of the European Ceramic Society 36(3) (2016) 733-739.

[22] Y. Zhang, J. Luo, Promoting the flash sintering of ZnO in reduced atmospheres to achieve nearly full densities at furnace temperatures of < 120 °C, Scripta Materialia 106 (2015) 26-29.

[23] J.M. Lebrun, R. Raj, A First Report of Photoemission in Experiments Related to Flash Sintering, Journal of the American Ceramic Society 97(8) (2014) 2427-2430.

[24] B. Yoon, D. Yadav, R. Raj, E.P. Sortino, S. Ghose, P. Sarin, D. Shoemaker, Measurement of O and Ti atom displacements in TiO_2 during flash sintering experiments, Journal of the American Ceramic Society 101(5) (2018) 1811-1817.

[25] D. Kok, D. Yadav, E. Sortino, S.J. McCormack, K.P. Tseng, W.M. Kriven, R. Raj, M.L. Mecartney, α-Alumina and spinel react into single-phase high-alumina spinel in < 3 seconds during flash sintering, Journal of the American Ceramic Society (2018).

[26] S.K. Jha, X.L. Phuah, J. Luo, C.P. Grigoropoulos, H. Wang, E. García, B. Reeja-Jayan, The effects of external fields in ceramic sintering, Journal of the American Ceramic Society 102(1) (2019) 5-31.

[27] J.M. Lebrun, C.S. Hellberg, S.K. Jha, W.M. Kriven, A. Steveson, K.C. Seymour, N. Bernstein, S.C. Erwin, R. Raj, In-situ measurements of lattice expansion related to defect generation during flash sintering, Journal of the American Ceramic Society 100(11) (2017) 4965-4970.

[28] R. Raj, Analysis of the Power Density at the Onset of Flash Sintering, Journal of the American Ceramic Society 99(10) (2016) 3226-3232.

[29] K. Naik, S.K. Jha, R. Raj, Correlations between conductivity, electroluminescence and flash sintering, Scripta Materialia 118 (2016) 1-4.

[30] C.E.J. Dancer, Flash sintering of ceramic materials, Materials Research Express 3(10) (2016) 102001.

[31] L.B. Caliman, R. Bouchet, D. Gouvea, P. Soudant, M.C. Steil, Flash sintering of ionic conductors: The need of a reversible electrochemical reaction, Journal of the European Ceramic Society 36(5) (2016) 1253-1260.

[32] C. McLaren, W. Heffner, R. Tessarollo, R. Raj, H. Jain, Electric field-induced softening of alkali silicate glasses, Applied Physics Letters 107(18) (2015) 184101.

[33] J.-M. Lebrun, T.G. Morrissey, J.S.C. Francis, K.C. Seymour, W.M. Kriven, R. Raj, Emergence and Extinction of a New Phase During On-Off Experiments Related to Flash Sintering of 3YSZ, Journal of the American Ceramic Society 98(5) (2015) 1493-1497.

[34] K.S. Naik, V.M. Sglavo, R. Raj, Flash sintering as a nucleation phenomenon and a model thereof, Journal of the European Ceramic Society 34(15) (2014) 4063-4067.

[35] J.-M. Lebrun, R. Raj, A First Report of Photoemission in Experiments Related to Flash Sintering, Journal of the American Ceramic Society 97(8) (2014) 2427-2430.

[36] P. Kumar MK, D. Yadav, J.M. Lebrun, R. Raj, Flash sintering with current rate: A different approach, Journal of the American Ceramic Society 102(2) (2019) 823-835.

[37] W. Rheinheimer, X.L. Phuah, H. Wang, F. Lemke, M.J. Hoffmann, H. Wang, The role of point defects and defect gradients in flash sintering of perovskite oxides, Acta Materialia 165 (2019) 398-408.

[38] W.D. Kingery, DENSIFICATION DURING SINTERING IN THE PRESENCE OF A LIQUID PHASE .1. THEORY, Journal of Applied Physics 30(3) (1959) 301-306.

[39] W.D. Kingery, M.D. Narasimhan, DENSIFICATION DURING SINTERING IN THE PRESENCE OF A LIQUID PHASE .2. EXPERIMENTAL, Journal of Applied Physics 30(3) (1959) 307-310.

[40] R. German, P. Suri, S. Park, Review: liquid phase sintering, Journal of Materials Science 44(1) (2009) 1-39.

[41] J. Luo, H.F. Wang, Y.M. Chiang, Origin of solid-state activated sintering in Bi2O3-doped ZnO, Journal of the American Ceramic Society 82(4) (1999) 916-920.

[42] V.K. Gupta, D.H. Yoon, H.M. Meyer, J. Luo, Thin intergranular films and solid-state activated sintering in nickel-doped tungsten, Acta Materialia 55(9) (2007) 3131-3142.

[43] J.L. Johnson, R.M. German, Theoretical modeling of densification during activated solid-state sintering, Metallurgical and Materials Transactions a-Physical Metallurgy and Materials Science 27(2) (1996) 441-450.

[44] J.Y. Nie, J.M. Chan, M.D. Qin, N.X. Zhou, J.A. Luo, Liquid-like grain boundary complexion and sub-eutectic activated sintering in CuO-doped TiO_2, Acta Materialia 130 (2017) 329-338.

[45] J. Luo, Developing Interfacial Phase Diagrams for Applications in Activated Sintering and Beyond: Current Status and Future Directions, Journal of the American Ceramic Society 95(8) (2012) 2358-2371.

[46] X.M. Shi, J. Luo, Developing grain boundary diagrams as a materials science tool: A case study of nickel-doped molybdenum, Physical Review B 84(1) (2011) 14.

[47] N. Zhou, J. Luo, Developing grain boundary diagrams for multicomponent alloys, Acta Materialia 91 (2015) 202-216.

[48] X. Shi, J. Luo, Grain boundary wetting and prewetting in Ni-doped Mo, Applied Physics Letters 94(25) (2009) 251908.

[49] J. Luo, X. Shi, Grain boundary disordering in binary alloys, Applied Physics Letters 92(10) (2008) 101901.

[50] J. Luo, V. Gupta, D. Yoon, H. Meyer III, Segregation-induced grain boundary premelting in nickel-doped tungsten, Applied Physics Letters 87(23) (2005) 231902.

[51] P.R. Cantwell, M. Tang, S.J. Dillon, J. Luo, G.S. Rohrer, M.P. Harmer, Overview No. 152: Grain boundary complexions, Acta Materialia 62 (2014) 1-48.

[52] A.R. Krause, P.R. Cantwell, C.J. Marvel, C. Compson, J.M. Rickman, M.P. Harmer, Review of grain boundary complexion engineering: Know your boundaries, Journal of the American Ceramic Society 102(2) (2019) 778-800.

[53] S.J. Dillon, M.P. Harmer, Demystifying the role of sintering additives with "complexion", Journal of the European Ceramic Society 28(7) (2008) 1485-1493.

[54] S.J. Dillon, M. Tang, W.C. Carter, M.P. Harmer, Complexion: A new concept for kinetic engineering in materials science, Acta Mater. 55(18) (2007) 6208-6218

[55] S.J. Dillon, M.P. Harmer, Multiple Grain Boundary Transitions in Ceramics: A Case Study of Alumnia, Acta Materialia 55 (2007) 5247-5254.

[56] J. Luo, Stabilization of Nanoscale Quasi-Liquid Interfacial Films in Inorganic Materials: A Review and Critical Assessment, Critical Reviews in Solid State and Material Sciences 32(1-2) (2007) 67-109.

[57] W.D. Kaplan, D. Chatain, P. Wynblatt, W.C. Carter, A review of wetting versus adsorption, complexions, and related phenomena: the rosetta stone of wetting Journal of Materials Science 48 (2013) 5681-5717.

[58] J.Y. Zhang, F.C. Meng, R.I. Todd, Z.Y. Fu, The nature of grain boundaries in alumina fabricated by fast sintering, Scripta Materialia 62(9) (2010) 658-661.

[59] X.M. Shi, J. Luo, Developing grain boundary diagrams as a materials science tool: A case study of nickel-doped molybdenum, Physical Review B 84(1) (2011).

[60] Y.H. Dong, I.W. Chen, Predicting the Onset of Flash Sintering, Journal of the American Ceramic Society 98(8) (2015) 2333-2335.

[61] Y. ZHANG, J. NIE, J. LUO, Effects of phase and doping on flash sintering of TiO 2, Journal of the Ceramic Society of Japan 124(4) (2016) 296-300.

[62] Y. Zhang, J. Luo, Promoting the flash sintering of ZnO in reduced atmospheres to achieve nearly full densities at furnace temperatures of <120 °C, Scripta Materialia 106 (2015) 26-29.

[63] M. Kim, S. Lai, R.M. Laine, Combinatorial Nanopowder Synthesis Along the ZnO-Al_2O_3 Tie Line Using Liquid-Feed Flame Spray Pyrolysis, Journal of the American Ceramic Society 94(10) (2011) 3308-3318.

[64] H. Serier, M. Gaudon, M. Menetrier, Al-doped ZnO powdered materials: Al solubility limit and IR absorption properties, Solid State Sciences 11(7) (2009) 1192-1197.

[65] G.M. Safronov, V.N. Batog, T.V. Stepanyuk, P.M. Fedorov, Equilibrium diagram of the bismuth oxide-zinc oxide system, Russian Journal of Inorganic Chemistry 16(3) (1971) 460-461.

[66] J. Luo, Y.M. Chiang, Wetting and prewetting on ceramic surfaces, Annual Review of Materials Research 38 (2008) 227-249.

[67] L.A. Hughes, K. van Benthem, Effects of electrostatic field strength on grain-boundary core structures in $SrTiO_3$, Journal of the American Ceramic Society 102(8) (2019) 4502-4510.

[68] W. Rheinheimer, J.P. Parras, J.H. Preusker, R.A. De Souza, M.J. Hoffmann, Grain growth in strontium titanate in electric fields: The impact of space-charge on the grain-boundary mobility, Journal of the American Ceramic Society 102(6) (2019) 3779-3790.

[69] L.A. Hughes, M. Marple, K. van Benthem, Electrostatic fields control grain boundary structure in $SrTiO_3$, Applied Physics Letters 113(4) (2018).

[70] W. Rheinheimer, X.L. Phuah, H. Wang, F. Lemke, M.J. Hoffmann, H.Y. Wang, The role of point defects and defect gradients in flash sintering of perovskite oxides, Acta Materialia 165 (2019) 398-408.

[71] H.R. Jin, S.H. Yoon, J.H. Lee, N.M. Hwang, D.Y. Kim, J.H. Han, Effect of external electric field on the grain growth of barium titanate in N_2 atmosphere, Journal of Materials Science-Materials in Electronics 16(11-12) (2005) 749-752.

[72] H.R. Jin, S.H. Yoon, J.H. Lee, N.M. Hwang, D.Y. Kim, J.H. Han, Effect of external electric field on the grain-growth behavior of barium titanate, Journal of the American Ceramic Society 87(9) (2004) 1747-1752.

[73] Y.H. Dong, H.R. Wang, I.W. Chen, Electrical and hydrogen reduction enhances kinetics in doped zirconia and ceria: I. grain growth study, Journal of the American Ceramic Society 100(3) (2017) 876-886.

[74] Y. Dong, I.W. Chen, Electrical and hydrogen reduction enhances kinetics in doped zirconia and ceria: II. Mapping electrode polarization and vacancy condensation in YSZ, Journal of the American Ceramic Society 101(3) (2018) 1058-1073.

[75] R. Raj, Joule heating during flash-sintering, Journal of the American Ceramic Society 32(10) (2012) 2293-2301.

[76] I. Kul'bakin, V. Belousov, S. Fedorov, A. Vorobiev, Solid/melt ZnO-Bi_2O_3 composites as ion transport membranes for oxygen separation from air, Materials Letters 67(1) (2012) 139-141.

[77] V.V. Belousov, Oxygen-permeable membrane materials based on solid or liquid Bi_2O_3, Mrs Communications 3(4) (2013) 225-233.

Chapter 4. Water-assisted flash sintering: Flashing ZnO at room temperature to achieve ~ 98% density in seconds

4.1. Introduction

On one hand, Raj and co-workers reported an innovative “flash sintering” technology in 2010 to use applied electric fields/currents to trigger fast densification at low furnace temperatures [1], which has been successfully applied to a broad range of ceramics [1-15] (as being recently reviewed by Yu *et al.* [16]). Low furnace temperatures and fast densification rates make flash sintering an energy-saving and cost-effective method to consolidate ceramics. A further pursuit of even lower onset flash temperatures was made by increasing the initial applied electric field ($E_{initial}$); specifically, the onset flash temperature of 8 mol. % Y_2O_3 stabilized ZrO_2 was lowered to 390 °C with a high $E_{initial}$ of 2250 V/cm [17], but only moderate densification (*i.e.*, ~8.5% linear shrinkage) was achieved [17]. Another prior work demonstrated that a reduced atmosphere (Ar + 5% H_2) can significantly lower the flash temperature of ZnO to <120 °C (via increasing the specimen conductivity to trigger a thermal runaway at a lower temperature, as supported by a quantitative model [4, 5, 18]) with an applied $E_{initial}$ of 500 V/cm [18]. Yet, a further reduction of the flash temperature could not be achieved (*e.g.*, even with a higher $E_{initial}$ of 1000 V/cm [18]), presumably because the reduced atmosphere cannot interact with the specimen effectively at <100 °C. Thus, a scientifically-interesting and technologically-attractive goal of triggering the flash sintering at room

temperature without any external furnace heating had remained unattainable, which motivated the current study.

On the other hand, ceramic researchers have observed enhanced or suppressed sintering rates of MgO [19], CaO [20], anatase TiO_2 [21], SnO_2 [22], ZnO [23], and doped Al_2O_3 [24] in the presence of water vapor. Recently, Randall and co-workers developed an innovative “cold sintering process (CSP)” to densify ceramics under 250 °C with the assistance of water or aqueous solutions under the pressure of several hundreds of MPa [25, 26], which has been successfully applied to $BaTiO_3$ [27], ZrO_2 [28, 29], ZnO [30], $NaNO_2$ and KH_2PO_4 [31], and V_2O_5 based ceramic-polymer composites [32]. Perhaps more relevantly, Guillon and co-workers recently discovered enhanced densification by adding water in nanocrystalline ZnO specimens sintered by the spark plasmas sintering/field-assisted sintering technology (SPS/FAST) [33, 34].

The above inspiring studies on electric field/current and water assisted sintering collectively motivated us to propose, and subsequently validate with experiments on the ZnO model system, a new water-assisted flash sintering (WAFS) method. In this study, we demonstrated that WAFS can reduce the onset flash of the ZnO powder specimen to room temperature and subsequently achieve ~98% of the theoretical density in 30 s.

4.2. Experiments

4.2.1. Materials Synthesis and Sintering

A >99.99% purity ZnO powder, purchased from Sigma Aldrich, was mixed with 0.5 wt. % binder (2 wt. % PVA in DI water), uniaxially pressed at ~300 MPa to form green pellets of *D* (diameter) = 6.4 mm and *H* (height) = 1.0 mm, and subsequently baked at 500 °C for 1 h to burn out the binder. The average grain sizes in the green pellets were measured to be ~120 nm, and the relative densities were measured to be 54.8 ± 0.4%. The Pt electrodes were sputtered on both side of surfaces and specimens were loaded into a horizontal quartz tube to connect with a Pt/Cu wire system (that has a negligible total resistance as compared with that of the ZnO specimen under all experimental conditions) for applying electric fields/currents. Flash sintering experiments were conducted in wet Ar + 5 mol. % H_2, by flowing the gas through a conical flask containing DI water at room temperature (as schematically shown in the graphical abstract). The system was purged with the flowing wet gas for 1 h before conducting flash sintering experiments. The specimen resistance was recorded during this period using a multimeter (DMM 4050, Tektronix Inc.). Subsequently, the flash sintering experiments were conducted at room temperature using a DC power supply (Sorensen XHR 150-7, Ametek Programmable Power Inc.) with initial electric fields $E_{initial}$ = 200, 150, and 100 V/cm, respectively. The power supply was automatically switched to a current-control mode after the flash once the current reach a preset maximum current of I_{max} = 2.4 A (corresponding to a nominal current density of $J \approx 75$ mA/mm^2, calculated without considering the densification of the specimen) for all flash sintering experiments. The electric power supply was shut off 30 s after the onset of flash sintering.

4.2.2. Materials Characterizations

Specimen densities were measured by the Archimedes method (for dense specimens) and/or via measuring the dimension and weight. The microstructures were characterized using a field emission scanning electron microscope (FE SEM, Philips XL30). Grain sizes were measured from polished specimens using a standard intercept method.

4.3. Results

Fig. 4.1 (a) shows the specimen conductivity *vs.* time curve of a ZnO green pellet after flowing with wet Ar + 5% H_2. The specimen conductivity increased steeply by more than four orders of magnitude from 3×10^{-7} S/cm to 7×10^{-3} S/cm in the first ~20 min after purging with the wet gas, presumably due to water absorption, and reached a steady state, approaching ~0.01 S/cm. To further understand the effects of absorbed water, we conducted an additional experiment to measure the conductivities of ZnO powder pellets in both dry and wet flowing Ar + 5% H_2 in a tube furnace with a constant heating rate of 20 °C/min (after first flowing for 1 h at room temperature to achieve the steady state). It is interesting to note from Fig. 4.1(b) that the conductivity of the specimen in wet flowing gas is almost constant and higher than that of the dry specimen until ~350 °C, at which temperature the conductivity of the dry specimen increases to the same level. This suggests that the water effects can persist at least to ~350 °C in the powder specimen at the heating rate of 20 °C/min and probably to even higher temperatures with two to

three orders of magnitude higher heating rates in flash sintering [5], which may help sustain the WAFS after the onset of a flash.

Fig. 4.2 shows the electric fields, currents, power densities, specimen conductivities, and estimated specimen temperatures (T_S) from a blackbody radiation model [4] during 30 s of the WAFS of three ZnO specimens with the initial electric field of $E_{initial}$ = 100, 150, and 200 V/cm, respectively. At the low $E_{initial}$ of 100 V/cm, a flash started gradually after an incubation period of ~5 s; at the intermediate $E_{initial}$ of 150 V/cm, a flash started intermediately. In both cases, the power densities (Fig. 4.2(c)) and estimated specimen temperatures (Fig. 4.2(e)) first increased but subsequently dropped to steady states, which were due to the increasing specimen conductivities (Fig. 4.2(d)) that generated less power in the constant-current mode. Consequently, the specimens reached the steady-state temperatures of 800-900 °C after ~10 s in these two cases, which did not lead to substantial densification/sintering. In contrast, with a high $E_{initial}$ = 200 V/cm, the power density immediately reached, and subsequently sustained at, a higher level of ~ 0.6 W/mm^3 to sustain the specimen temperature at >1100 °C (Fig. 4.2(e)) to enable fast densification. Consistently, the specimen with $E_{initial}$ = 200 V/cm achieved ~98.3 $\pm$ 0.7 % relative density after WAFS for 30 s with a measured average grain size of 1.83 ± 0.30 μm (Fig. 4.3(a)). The Intragranular pores embedded in the large grains are also evidence of the ultrafast grain growth. In contrast, the specimen with $E_{initial}$ = 100 V/cm essentially did not densify/sinter appreciably (Fig. 4.3(b)) because of the lower steady-state specimen temperature of ~850 °C (Fig. 4.2(e)).

The observation that densification only occurred when the $E_{initial}$ was above a critical threshold (Fig. 4.2 and Fig. 4.3) suggested the existence of bifurcation [35] in kinetic pathways after the flash events. In other words, the final steady states set (constrained) by the preset experimental condition of I_{max} = 2.4 A can be satisfied by two specimen states: a low-temperature (~850 °C) un-sintered (powder) specimen with a higher conductivity (~0.3 S/cm, which is presumably due to high surface conductivity) *vs.* a high-temperature (~1100 °C) sintered specimen with lower bulk conductivity (~0.1 S/cm). When $E_{initial}$ was sufficiently high (*e.g.*, 200 V/cm), the high initial power generation and the associated high temperature increasing rate led to the densification pathway and latter state of a dense, bulk specimen; otherwise, the specimen would remain un-sintered (as a powder specimen with high surface conduction) at the lower $E_{initial}$ of 100 or 150 V/cm.

In addition to triggering the flash at room temperature by substantially increasing the specimen conductivity, water could also help the mass transport as demonstrated by the water assisted SPS/FAST of ZnO that was substantial at ~250-400 °C [33, 34]. The water effects on transport could be effective in the initial stage of WAFS (before drying); Fig. 4.1(b) suggests that the water effects can persist to at least ~350 °C at the heating rate of 20 °C/min and they can persist to higher temperatures during flash sintering where the heating rate is on the order of 100 °C/s [5]; furthermore, such effects can be more pronouncing with a high $E_{initial}$ that leads to extremely high initial heating and densification rates. Nonetheless, it is still difficult to determine how significant the water in fact enhanced the mass transport of ZnO, if any, in the current case of WAFS.

4.4. Conclusions

In summary, a new WAFS method was proposed for the first time. Using ZnO as a model system, this study successfully demonstrated that WAFS can start at room temperature to achieve ~98% relative density in 30 s in wet Ar + 5% H_2. This method can potentially be extended to consolidate other ceramic systems to achieve fast densification at extremely low furnace temperatures or, ideally, room temperature. Furthermore, this study suggests significant technological opportunities for energy and cost savings via exploiting and investigating new ceramic processing science through the interplay of water, electric fields/currents, and ultrafast heating rates.

Chapter 4, in part, is a reprint of the publication “Water-assisted flash sintering: Flashing ZnO at room temperature to achieve ~ 98% density in seconds”, J. Nie, Y. Zhang, J.M. Chan, R. Huang, and J. Luo, as it appears in Scripta Materialia, 2018, 142, 79. The dissertation author was the primary investigator and author of this paper.

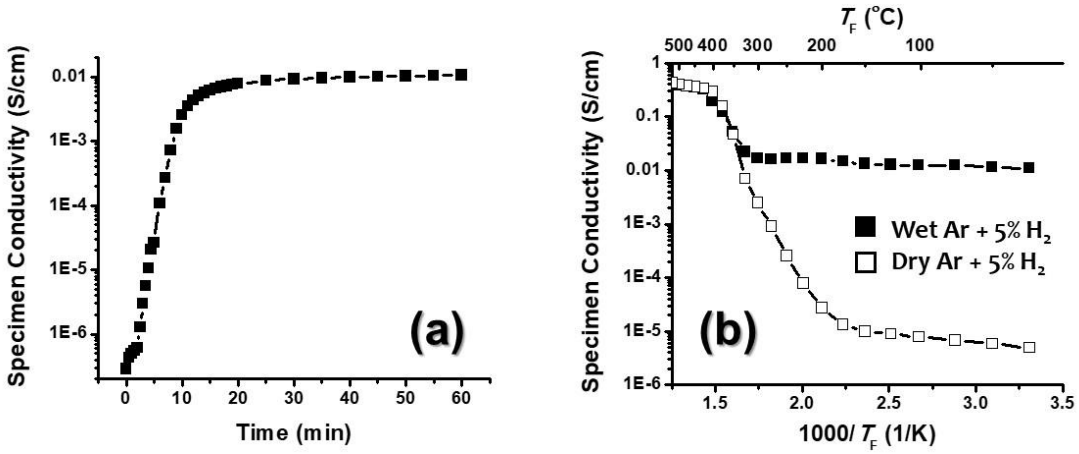

Figure 4.1 (a) Specimen conductivity *vs.* time curve of a ZnO green pellet in flowing wet Ar + 5% H_2. (b) Specimen conductivity *vs.* temperature curves measured from two ZnO specimens in dry and wet Ar + 5% H_2, respectively, in a furnace that was heated at a constant ramping rate of 20 °C/min.

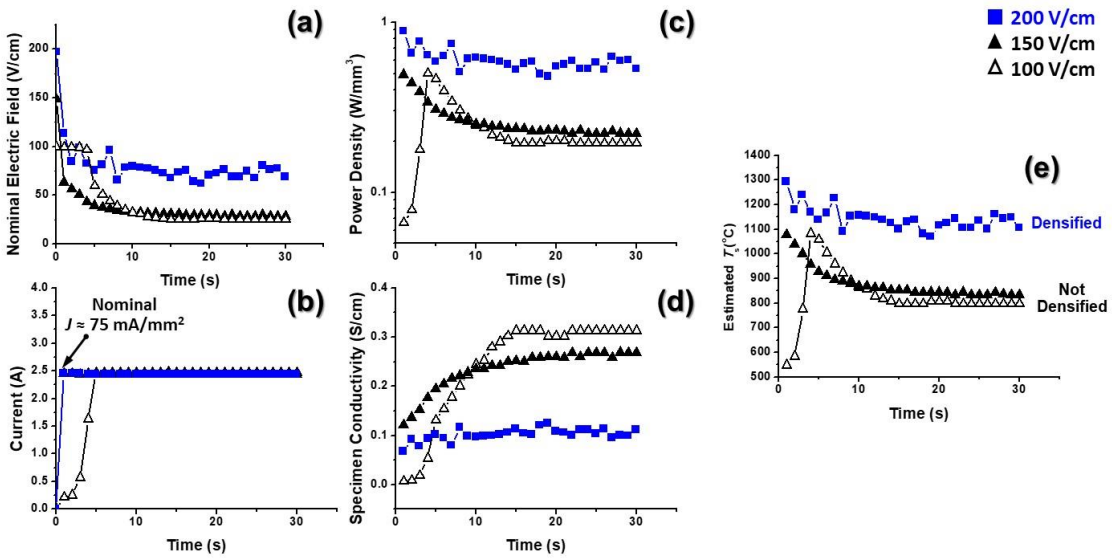

Figure 4.2 The (a) nominal electric field, (b) current, (c) power density, (d) specimen conductivity, and (e) estimated specimen temperature (T_S) of ZnO *vs.* time curves during water-assisted flash sintering (WAFS) of three ZnO specimens with $E_{initial}$ = 100, 150, and 200 V/cm.

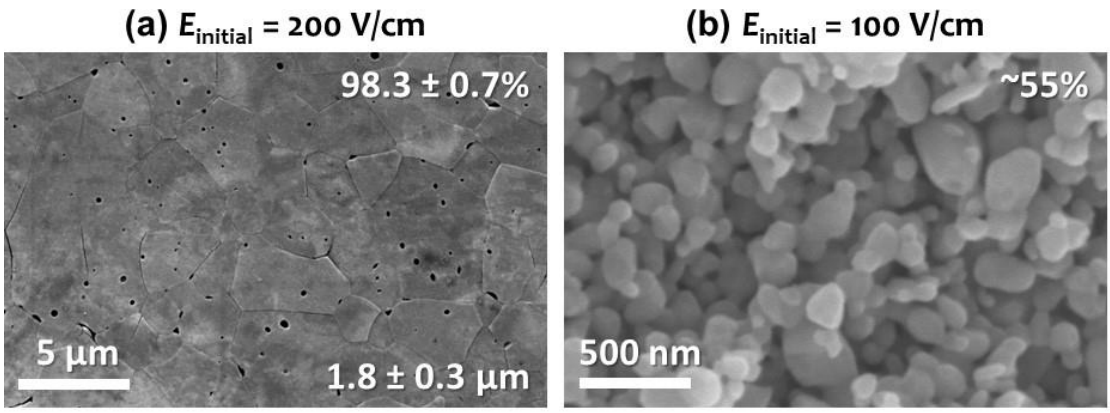

Figure 4.3 SEM micrographs of (a) a polished cross section of a flash-sintered ZnO specimen with $E_{initial}$ = 200 V/cm and (b) a fractured surface of a specimen with $E_{initial}$ = 100 V/cm.

References

[1] M. Cologna, B. Rashkova, R. Raj, Flash Sintering of Nanograin Zirconia in < 5 s at 850 °C, Journal of the American Ceramic Society 93(11) (2010) 3556-3559.

[2] M. Cologna, A.L. Prette, R. Raj, Flash-Sintering of Cubic Yttria-Stabilized Zirconia at 750 °C for Possible Use in SOFC Manufacturing, Journal of the American Ceramic Society 94(2) (2011) 316-319.

[3] H. Yoshida, Y. Sakka, T. Yamamoto, J.-M. Lebrun, R. Raj, Densification behaviour and microstructural development in undoped yttria prepared by flash-sintering, Journal of the American Ceramic Society 34(4) (2014) 991-1000.

[4] Y.Y. Zhang, J.I. Jung, J. Luo, Thermal runaway, flash sintering and asymmetrical microstructural development of ZnO and ZnO-Bi_2O_3 under direct currents, Acta Mater. 94 (2015) 87-100.

[5] Y.Y. Zhang, J.Y. Nie, J.M. Chan, J. Luo, Probing the densification mechanisms during flash sintering of ZnO, Acta Mater. 125 (2017) 465-475.

[6] C. Schmerbauch, J. Gonzalez-Julian, R. Röder, C. Ronning, O. Guillon, Flash sintering of nanocrystalline zinc oxide and its influence on microstructure and defect formation, Journal of the American Ceramic Society 97(6) (2014) 1728-1735.

[7] Y.Y. Zhang, J.Y. Nie, J. Luo, Effects of phase and doping on flash sintering of TiO_2, J. Ceram. Soc. Jpn. 124(4) (2016) 296-300.

[8] S.K. Jha, R. Raj, The Effect of Electric Field on Sintering and Electrical Conductivity of Titania, Journal of the American Ceramic Society 97(2) (2014) 527-534.

[9] A. Karakuscu, M. Cologna, D. Yarotski, J. Won, J.S. Francis, R. Raj, B.P. Uberuaga, Defect Structure of Flash-Sintered Strontium Titanate, Journal of the American Ceramic Society 95(8) (2012) 2531-2536.

[10] A. Gaur, V.M. Sglavo, Densification of $La_{0.6}Sr_{0.4}Co_{0.2}Fe_{0.8}O_3$ ceramic by flash sintering at temperature less than 100 °C, Journal of Materials Science 49(18) (2014) 6321-6332.

[11] A.L. Prette, M. Cologna, V. Sglavo, R. Raj, Flash-sintering of Co_2MnO_4 spinel for solid oxide fuel cell applications, Journal of Power Sources 196(4) (2011) 2061-2065.

[12] E. Zapata-Solvas, S. Bonilla, P. Wilshaw, R. Todd, Preliminary investigation of flash sintering of SiC, Journal of the European Ceramic Society 33(13) (2013) 2811-2816.

[13] S. Grasso, T. Saunders, H. Porwal, B. Milsom, A. Tudball, M. Reece, Flash spark plasma sintering (FSPS) of α and β SiC, Journal of the American Ceramic Society (2016).

[14] S. Grasso, T. Saunders, H. Porwal, O. Cedillos-Barraza, D.D. Jayaseelan, W.E. Lee, M.J. Reece, Flash spark plasma sintering (FSPS) of pure ZrB_2, Journal of the American Ceramic Society 97(8) (2014) 2405-2408.

[15] J. Nie, Y. Zhang, J.M. Chan, S. Jiang, R. Huang, J. Luo, Two-step flash sintering of ZnO: Fast densification with suppressed grain growth, Scripta Materialia 141 (2017) 6-9.

[16] M. Yu, S. Grasso, R. McKinnon, T. Saunders, M.J. Reece, Review of flash sintering: materials, mechanisms and modelling, Advances in Applied Ceramics 116(1) (2017) 24-60.

[17] J.A. Downs, V.M. Sglavo, Electric Field Assisted Sintering of Cubic Zirconia at 390 °C, Journal of the American Ceramic Society 96(5) (2013) 1342-1344.

[18] Y.Y. Zhang, J. Luo, Promoting the flash sintering of ZnO in reduced atmospheres to achieve nearly full densities at furnace temperatures of < 120 °C, Scr. Mater. 106 (2015) 26-29.

[19] P.J. Anderson, P.L. Morgan, EFFECTS OF WATER VAPOUR ON SINTERING OF MGO, Transactions of the Faraday Society 60(4975) (1964) 930-&.

[20] R.H. Borgwardt, CALCIUM-OXIDE SINTERING IN ATMOSPHERES CONTAINING WATER AND CARBON-DIOXIDE, Ind. Eng. Chem. Res. 28(4) (1989) 493-500.

[21] J.L. Hebrard, P. Nortier, M. Pijolat, M. Soustelle, INITIAL SINTERING OF SUBMICROMETER TITANIA ANATASE POWDER, Journal of the American Ceramic Society 73(1) (1990) 79-84.

[22] L. Perazolli, J.A. Varela, E.R. Leite, E. Longo, Effect of atmosphere on the sintering and grain growth of tin oxide, Advanced Powder Technology 299-3 (1999) 134-140.

[23] J.A. Varela, O.J. Whittemore, E. Longo, PORE-SIZE EVOLUTION DURING SINTERING OF CERAMIC OXIDES, Ceram. Int. 16(3) (1990) 177-189.

[24] J.P. Angle, P.E.D. Morgan, M.L. Mecartney, Water Vapor-Enhanced Diffusion in Alumina, Journal of the American Ceramic Society 96(11) (2013) 3372-3374.

[25] J. Guo, S.S. Berbano, H.Z. Guo, A.L. Baker, M.T. Lanagan, C.A. Randall, Cold Sintering Process of Composites: Bridging the Processing Temperature Gap of Ceramic and Polymer Materials, Advanced Functional Materials 26(39) (2016) 7115-7121.

[26] J. Guo, H.Z. Guo, A.L. Baker, M.T. Lanagan, E.R. Kupp, G.L. Messing, C.A. Randall, Cold Sintering: A Paradigm Shift for Processing and Integration of Ceramics, Angewandte Chemie International Edition 55(38) (2016) 11457-11461.

[27] H.Z. Guo, A. Baker, J. Guo, C.A. Randall, Protocol for Ultralow-Temperature Ceramic Sintering: An Integration of Nanotechnology and the Cold Sintering Process, ACS Nano 10(11) (2016) 10606-10614.

[28] H.Z. Guo, T.J.M. Bayer, J. Guo, A. Baker, C.A. Randall, Cold sintering process for 8 mol. % Y_2O_3-stabilized ZrO_2 ceramics, Journal of the European Ceramic Society 37(5) (2017) 2303-2308.

[29] H.Z. Guo, J. Guo, A. Baker, C.A. Randall, Cold sintering process for ZrO_2-based ceramics: significantly enhanced densification evolution in yttria-doped ZrO_2, Journal of the American Ceramic Society 100(2) (2017) 491-495.

[30] S. Funahashi, J. Guo, H.Z. Guo, K. Wang, A.L. Baker, K. Shiratsuyu, C.A. Randall, Demonstration of the cold sintering process study for the densification and grain growth of ZnO ceramics, Journal of the American Ceramic Society 100(2) (2017) 546-553.

[31] H.Z. Guo, A. Baker, J. Guo, C.A. Randall, Cold Sintering Process: A Novel Technique for Low-Temperature Ceramic Processing of Ferroelectrics, Journal of the American Ceramic Society 99(11) (2016) 3489-3507.

[32] J. Guo, H.Z. Guo, D.S.B. Heidary, S. Funahashi, C.A. Randall, Semiconducting properties of cold sintered V_2O_5 ceramics and Co-sintered V_2O_5-PEDOT:PSS composites, Journal of the European Ceramic Society 37(4) (2017) 1529-1534.

[33] B. Dargatz, J. Gonzalez-Julian, M. Bram, P. Jakes, A. Besmehn, L. Schade, R. Roder, C. Ronning, O. Guillon, FAST/SPS sintering of nanocrystalline zinc

oxide-Part I: Enhanced densification and formation of hydrogen-related defects in presence of adsorbed water, Journal of the European Ceramic Society 36(5) (2016) 1207-1220.

[34] B. Dargatz, J. Gonzalez-Julian, M. Bram, Y. Shinoda, F. Wakai, O. Guillon, FAST/SPS sintering of nanocrystalline zinc oxide-Part II: Abnormal grain growth, texture and grain anisotropy, Journal of the European Ceramic Society 36(5) (2016) 1221-1232.

[35] J.G.P. da Silva, H.A. Al-Qureshi, F. Keil, R. Janssen, A dynamic bifurcation criterion for thermal runaway during the flash sintering of ceramics, Journal of the European Ceramic Society 36(5) (2016) 1261-1267.

Chapter 5. Two-step flash sintering of ZnO: Fast densification with suppressed grain growth

5.1. Introduction

In 2000, Chen and Wang developed an innovative two-step sintering method to inhibit the final-stage grain growth that would normally occur when the relative density is above ~90% [1]. In two-step sintering, a green specimen was first heated to a higher temperature, T_1, to reach a critical relative density, followed by holding at a lower temperature, T_2 ($T_2 < T_1$), in the second step for a prolonged time to achieve a high relative density while suppressing the final-stage rapid grain growth. This method has been successfully applied to various ceramic materials, including undoped/doped Y_2O_3 [1, 2], $BaTiO_3$ [3, 4], ZnO [5], Al_2O_3 [6], and SiC [7]. Yet, there are several technical challenges for the application of two-step sintering. For example, a prolonged holding time in the second step, *e.g.*, up to 20 hours in the case of conventional two-step sintering of ZnO [5], is typically required. Moreover, the short holding duration in the first step and (sometimes) desired fast cooling from the first to second step [2, 3, 8] may lead to large relative deviations of the exact specimen temperatures from the targeted profiles. Inspired by a novel flash sintering method developed by Raj and co-workers in 2010 [9], here we proposed and subsequently demonstrated a new two-step flash sintering (TSFS) method to achieve comparable results as those demonstrated in conventional two-step sintering of ZnO [5] in as short as ~5 minutes; this represents a >200 times reduction in the sintering time [5], thereby implying not only convenient electronic

controls (with ultrafast heating and cooling rates) but also a great potential for energy and cost savings with a drastically improved efficiency.

Flash sintering enabled fast densification at low furnace temperatures, which have been successfully applied to Y_2O_3-stablized ZrO_2 [9, 10], Y_2O_3 [11], ZnO [12-14], TiO_2 [15, 16], $SrTiO_3$ [17, 18], and other oxide [19-21] as well as non-oxide [22-25] ceramics. In most systems, the flash starts as a thermal runaway, where quantitative models [12, 13, 15, 26-28] have been developed and tested. At least for ZnO, fast densification is related to ultrahigh heating rates (~200 °C/s) since a recent study demonstrated that rapid thermal annealing with comparable heating profiles can achieve similar densification and grain growth rates [13]. However, rapid final-stage grain growth also occurred in flash sintering in a similar fashion as those observed in conventional sintering, albeit a much shorter time scale [13]. In this study, we further proposed a new TSFS method to substantially reduce the final-stage grain growth as compared with the conventional (one-step) flash sintering and subsequently demonstrated its feasibility using a model system (ZnO).

5.2. Experiments

5.2.1. Materials synthesis and Sintering

A ZnO powder (99.95% purity, purchased from US Research Nanomaterials, Inc.) was mixed with 0.5 wt. % binder (PVA in DI water). The mixtures were uniaxially pressed at ~300 MPa to form green pellets of the dimension: *D* (diameter) = 6.4 mm and *H* (height) = 2.8 mm. Green pellets were

baked at 500 °C for 1 hour to burn out the binder. After burning the binder, the average grain size in the green pellets was measured to be 36 ± 2 nm and the bulk densities were measured to be 57.3 ± 0.8%. The specimen surfaces were sputtered with platinum as electrodes using a Denton Discovery 18 Sputtering System. The sides of the sputtered specimens were ground using SiC papers. For flash sintering experiments, specimens were loaded into a modified dilatometer (DIL 402 PC, Netzsch, Boston, MA, USA) equipped with Pt electrodes and circuit (for applying electric fields/currents) and flowed with argon at a constant rate of 33 mL/min. The system was purged with argon for one hour before heating up to 500 °C at a constant rate of 5 °C/min. Subsequently, the flash sintering experiments were conducted isothermally at 500 °C, where a programmable DC power supply (DLM300-10, Ametek Inc., San Diego, CA, USA) was used to apply electric fields/currents.

All flash sintering experiments were conducted at an isothermal furnace temperature of 500 °C in this study (instead of a constant ramping rate as in most other flash sintering experiments, so that it can be better compared with TSFS experiments), where a flash typically started ~20-30 s after applying the constant (initial) electric field of 150 V/cm. The electric field was kept a constant (150 V/cm in this case), until the specimen current reached a preset limit and the power supply was switched from a voltage-control to a current-control mode. For conventional (one-step) flash sintering, the current limit (I_{max}) was kept at 3 A (corresponding to a nominal current density of $J_{max} \approx 95$ mA/mm^2, calculated from the initial specimen dimension; noting that the actual J_{max} increases with time due the densification of

specimen) for a duration of 2 s, 6 s, 15 s, and 30 s, respectively, after the onset of flash. For TSFS, the current limit was set to I_1 = 3 A (nominal $J_1 \approx 95$ mA/mm^2) for a fixed duration of 6 s (3 A $\times$ 6 s) in the first step and subsequently reduced to I_2 = 2 A (nominal $J_2 \approx 63$ mA/mm^2) and kept for a duration of 150 s or 300 s. After flash sintering, both the electric power and the furnace were shut down and the specimens were cooled down in the furnace; the flowing argon was shut off after the specimen cooled to room temperature.

5.2.2. Material characterization

After the completion of flash sintering experiments, the specimen densities were calculated via measuring dimensions and weights; the Archimedes method was also used, if the relativity densities were greater than 90%. Microstructures of flash sintered specimens were characterized using a field-emission ultra-high resolution environmental scanning electron microscope (UHR-SEM, FEI XL30) operating at 10 kV. Grain sizes were measured from SEM micrographs of fractured surfaces using a standard intercept method.

5.3. Results and Discussion

The grain size *vs.* relative density curves for both conventional (one-step) flash sintering and TSFS are shown in Fig. 5.1. Representative microstructures of the fractured surfaces of six sintered specimens are shown in Fig. 5.2. Here, the grain sizes and densities were measured from specimens that were cooled down to room temperature, where the effects of the densification and grain growth during the cooling were also included.

In conventional one-step flash sintering experiments, the relative density increased from ~57% in the green specimen to ~72% in the 3 A $\times$ 2 s sintered specimen, while the grain size increased from 36 ± 2 nm in the green specimen to 214 ± 18 nm in the sintered specimen. Increasing the flash sintering duration from 2 s to 6 s, the relative density increased substantially to ~90%, while the grain size increased only moderately to 267 ± 30 nm, in the 3 A $\times$ 6 s sintered specimen. Further increasing the flash sintering duration, the relative density increased to ~95% with a substantial grain growth to 1.18 ± 0.14 μm in the 3 A $\times$ 15 s sintered specimen; the relative density and grain size, respectively, reached ~97.6% and 1.75 ± 0.16 μm, respectively, in the 3 A $\times$ 30 s sintered specimen. Here, the observed rapid final-stage grain growth (when the relative density was above ~90%) is consistent with results measured from both conventional flash sintering, as well as rapid thermal annealing, of ZnO conducted in air [13] and it agrees with what is expected from the classical sintering theory.

The linear shrinkage was also measured *in situ* by dilatometry for flash sintering of ZnO at 500 °C in argon ($E_{initial}$ =150 V/cm and I_{max}), where electric power was shut off at 30 s after the onset flash (Fig. 5.3). The specimen densified to ~93% in 30 s after the onset of flash as measured by *in-situ* dilatometry. The final density was measured using the Archimedes method to be 97.6% (close to that calculated from the measured linear shrinkage at 60 s). This measured linear shrinkage *vs.* time curve was used as a guide to select the duration for the first step of the TSFS experiments to be 6 s, at which time the specimen reached ~81% of the theoretical density, since a prior study of conventional two-step sintering of

ZnO suggested that the first step should reach to >78% of theoretical density [5]. Noting the measured relative density of the 3 A × 6 s sintered specimen was ~90%, which included the contribution of densification during the cooling.

In the TSFS (*i.e.* two-step flash sintering) experiments conducted with $E_{initial}$ =150 V/cm, a fixed first step of 3 A × 6 s (*i.e.*, I_1 = 3 A for a fixed duration of 6 s), and a second step of a fixed current I_2 = 2 A, the grain size only increased to 330 ± 28 nm with a further increase in the relative density to 94.7% (in comparison with the ~267 nm grain size and ~90% density of the 3 A × 6 s sintered specimen; see Fig. 5.1 and Fig. 5.2). A longer second step of 300 s resulted in a grain size of 370 ± 17 nm and a relative density of 96.5% in the 3 A × 6 s + 2 A × 300 s sintered specimen. As shown in Fig. 5.1, the grain growth was suppressed in the TSFS experiments, where the grain sizes were less than 1/3 of those expected in the conventional (one-step) flash sintering with identical densities from interpolation. The grain size *vs.* density curve obtained from the TSFS was similar to that of the optimal case of conventional two-step sintering of ZnO reported in a prior study [5]; yet TSFS achieved this result (~370 nm grain size at ~96.5% relative density) in ~5 minutes, whereas it took ~15-20 hours in conventional two-step sintering to achieve comparable results of densification and grain growth (*i.e.*, ~500 nm at ~95% or ~650 nm at ~98% relative density, with a smaller starting particle/grain size of ~11 nm) [5]. In other words, the new TSFS method is >200 times faster in obtaining comparable (or slightly better) results than the conventional two-step sintering [5], representing a substantial opportunity for energy and cost savings via drastically improving the efficiency.

We also conducted a 2 A × 600 s one-step flash sintering experiment for an additional comparison, which produced a 95.8% dense specimen with the measured average grain size of 2.01 ± 0.18 μm. This result suggested that longer holding at 2 A could not achieve the simultaneous small grain size and high density obtained by the TSFS.

The measured time-dependent current, current density, electric field, and linear shrinkage of a representative specimen undergoing TSFS (in the first ~35 s after the flash) are shown in Figs. 5.4 (a) – (d). The calculated power density and estimated specimen temperature (T_s) from the blackbody radiation model [12] are shown in Figs. 5.4 (e) and (f). The actual current followed the controlled profile (3 A × 6 s + 2 A × 300 s) well with only minor fluctuations, while the relatively large fluctuations in the voltage (electric field) *vs.* time curve reflected the specimen response under the current-control mode. While the current was controlled to be a constant in each step (Fig. 5.4(a)), the current density increased continuously (more noticeably in the first step) due to the specimen shrinkage during densification (Fig. 5.4(b)). It was evident from the measured linear shrinkage *vs.* time curve (Fig. 5.4(d)) that densification was fast in the first step (0 to 6 s) and slowed down in the second step. The power density increased gradually in the incubation period under the voltage-controlled mode prior to the onset of the flash, but it largely followed a two-step function in the TSFS under the current-controlled mode (Fig. 5.4(e)). The estimated specimen temperature (T_s) was between 1600 and 1700 °C in the first step and between 1300 and 1450 °C in the second step; thus, the temperature difference (ΔT_S) between the two steps was estimated to be

~200-300 °C (Fig. 5.4(f)). The final relative density of the 3 A × 6 s + 2 A × 300 s sintered specimen (after cooling to room temperature) was measured to be 96.5 ± 0.3% using the Archimedes method and the grain size was measured to be 370 ± 17 nm.

5.4. Conclusions

In summary, a new TSFS method has been proposed to achieve fast densification (in comparison with the conventional two-step sintering) with suppressed grain growth (in comparison with the conventional flash sintering), where a specimen was kept at a higher current of I_1 for a short duration t_1 after the onset of flash, and electronically switched to a lower current of I_2 ($< I_1$) for a longer duration t_2 ($> t_1$). Using ZnO as a model system, this study successfully achieved ~96.5% of the theoretical density with a grain size of ~ 370 nm (representing a >3 times reduction in final-stage grain growth in comparison with the conventional one-step flash sintering) in ~5 minutes using this new TSFS method, which is >200 times faster than that can be obtained in the conventional two-step sintering. This cost-effective and energy-saving TSFS method can potentially be applied on other materials to achieve fast densification with suppressed grain growth. This study further suggests a new direction to control the densification and microstructural evolution via controlling and manipulating the $I(t)$ profile in flash sintering to any preset profile to achieve better or more customized results.

Chapter 5, in part, is a reprint of the manuscript “Two-Step Flash Sintering of ZnO: Fast Densification with Suppressed Grain Growth”, J. Nie, Y. Zhang, J.M. Chan, S. Jiang, R. Huang, J. Luo, as it appears in Scripta Materialia, 2017, 141, 6. The dissertation author was the primary investigator and author of this paper.

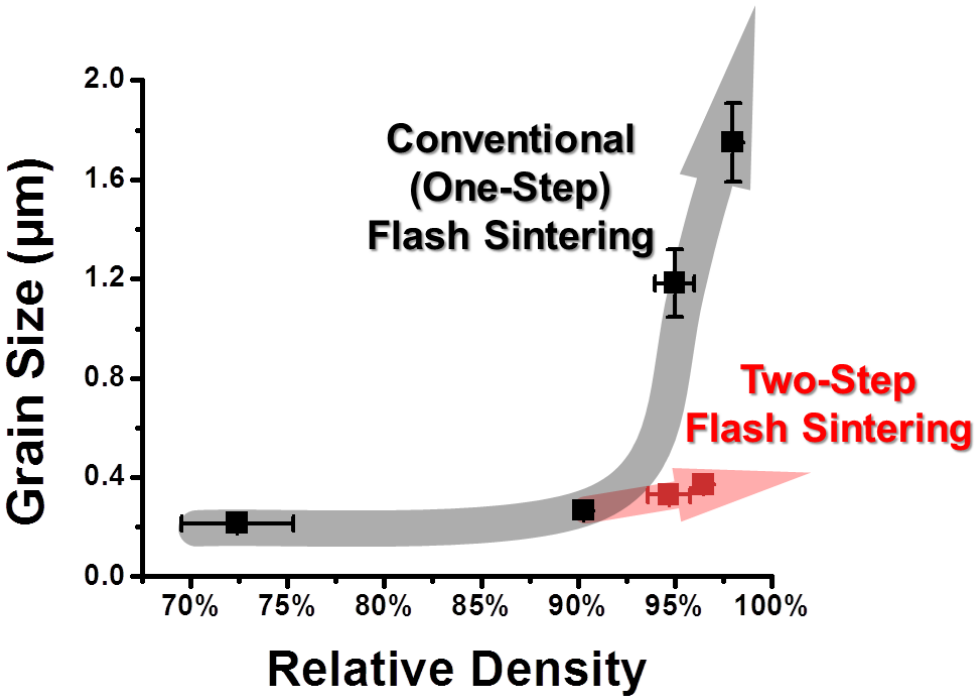

Figure 5.1 Grain size *vs.* relative density of ZnO specimens fabricated by conventional (one-step) and two-step flash sintering.

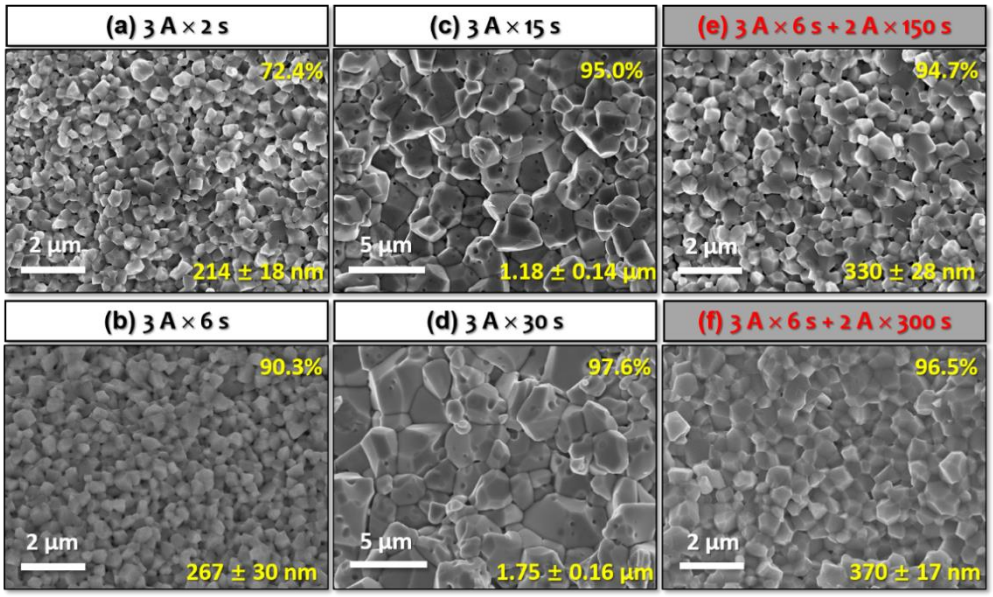

Figure 5.2 SEM micrographs of the fractured surfaces of the conventional (one-step) flash sintered ZnO specimens quenched (a) 2 s, (b) 6 s, (c) 15 s, and (d) 30 s, respectively, after the onset of flash, where the current limits were 3 A, as well as the two-step flash sintered ZnO specimens quenched after (e) 3 A × 6 s + 2 A × 150 s and (f) 3 A × 6 s + 2 A × 300 s.

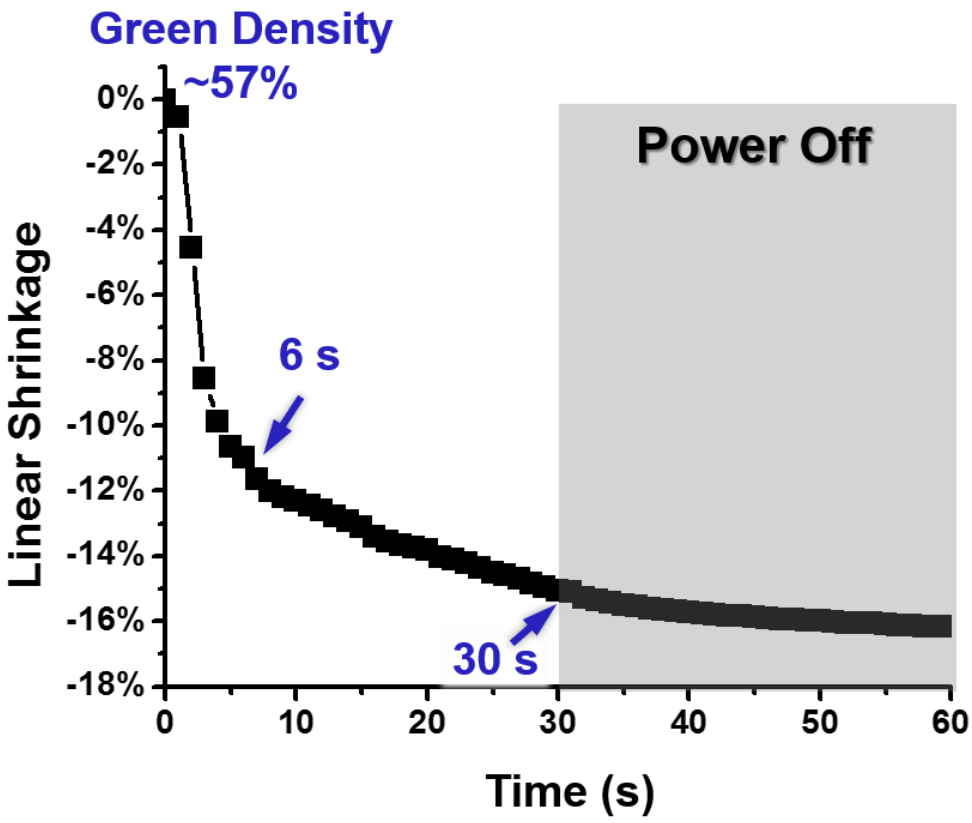

Figure 5.3 Measured linear shrinkage *vs.* time curve for (one-step) flash sintering of ZnO conducted in argon with a constant furnace temperature of T_F = 500 °C, where the applied electric field was set to 150 V/cm initially and the maximum current limit was set to 3 A. Electric power was shut off 30 seconds after the onset of flash (while the densification continues for ~30 s during the cooling of the specimen).

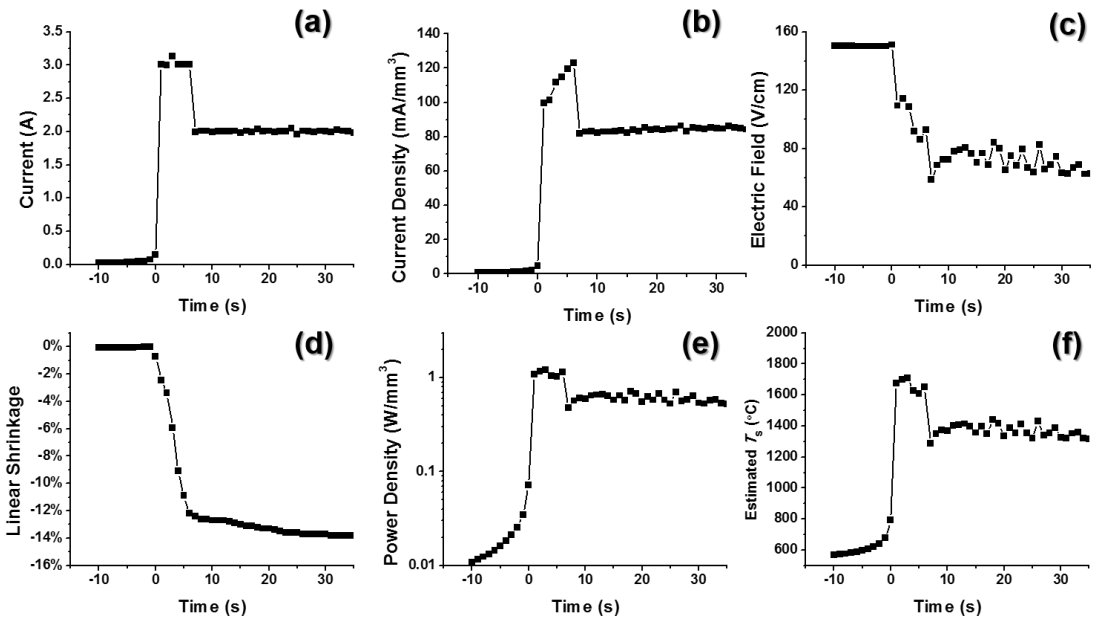

Figure 5.4 *In-situ* measurements of the first ~35 s in TSFS, including time-dependent (a) current, (b) current density, (c) electric field, and (d) linear shrinkage, as well as the (e) computed power density and (f) estimated specimen temperature (T_S).

References

[1] I.W. Chen, X.H. Wang, Sintering dense nanocrystalline ceramics without final-stage grain growth, Nature 404(6774) (2000) 168-171.

[2] X.H. Wang, P.L. Chen, I.W. Chen, Two-step sintering of ceramics with constant grain-size, I. Y_2O_3, Journal of the American Ceramic Society 89(2) (2006) 431-437.

[3] X.H. Wang, X.Y. Deng, H.L. Bai, H. Zhou, W.G. Qu, L.T. Li, I.W. Chen, Two-step sintering of ceramics with constant grain-size, II: $BaTiO_3$ and Ni-Cu-Zn ferrite, Journal of the American Ceramic Society 89(2) (2006) 438-443.

[4] T. Karaki, K. Yan, T. Miyamoto, M. Adachi, Lead-free piezoelectric ceramics with large dielectric and piezoelectric constants manufactured from $BaTiO_3$ nano-powder, Japanese Journal of Applied Physics Part 2-Letters & Express Letters 46(4-7) (2007) L97-L98.

[5] M. Mazaheri, A.M. Zahedi, S.K. Sadrnezhaad, Two-step sintering of nanocrystalline ZnO compacts: Effect of temperature on densification and grain growth, Journal of the American Ceramic Society 91(1) (2008) 56-63.

[6] J.G. Li, Y.P. Ye, Densification and grain growth of Al_2O_3 nanoceramics during pressureless sintering, Journal of the American Ceramic Society 89(1) (2006) 139-143.

[7] Y.I. Lee, Y.W. Kim, M. Mitomo, D.Y. Kim, Fabrication of dense nanostructured silicon carbide ceramics through two-step sintering, Journal of the American Ceramic Society 86(10) (2003) 1803-1805.

[8] M. Mazaheri, A. Simchi, F. Golestani-Fard, Densification and grain growth of nanocrystalline 3Y-TZP during two-step sintering, Journal of the European Ceramic Society 28(15) (2008) 2933-2939.

[9] M. Cologna, B. Rashkova, R. Raj, Flash Sintering of Nanograin Zirconia in < 5 s at 850 °C, Journal of the American Ceramic Society 93(11) (2010) 3556-3559.

[10] M. Cologna, A.L. Prette, R. Raj, Flash-Sintering of Cubic Yttria-Stabilized Zirconia at 750 °C for Possible Use in SOFC Manufacturing, Journal of the American Ceramic Society 94(2) (2011) 316-319.

[11] H. Yoshida, Y. Sakka, T. Yamamoto, J.-M. Lebrun, R. Raj, Densification behaviour and microstructural development in undoped yttria prepared by flash-sintering, Journal of the European Ceramic Society 34(4) (2014) 991-1000.

[12] Y.Y. Zhang, J.I. Jung, J. Luo, Thermal runaway, flash sintering and asymmetrical microstructural development of ZnO and ZnO-Bi_2O_3 under direct currents, Acta Materialia 94 (2015) 87-100.

[13] Y.Y. Zhang, J.Y. Nie, J.M. Chan, J. Luo, Probing the densification mechanisms during flash sintering of ZnO, Acta Materialia 125 (2017) 465-475.

[14] C. Schmerbauch, J. Gonzalez-Julian, R. Röder, C. Ronning, O. Guillon, Flash sintering of nanocrystalline zinc oxide and its influence on microstructure and defect formation, Journal of the American Ceramic Society 97(6) (2014) 1728-1735.

[15] Y.Y. Zhang, J.Y. Nie, J. Luo, Effects of phase and doping on flash sintering of TiO_2, Journal of the Ceramic Society of Japan 124(4) (2016) 296-300.

[16] S.K. Jha, R. Raj, The Effect of Electric Field on Sintering and Electrical Conductivity of Titania, Journal of the American Ceramic Society 97(2) (2014) 527-534.

[17] F. Lemke, W. Rheinheimer, M.J. Hoffmann, A comparison of power controlled flash sintering and conventional sintering of strontium titanate, Scripta Materialia 130 (2017) 187-190.

[18] A. Karakuscu, M. Cologna, D. Yarotski, J. Won, J.S. Francis, R. Raj, B.P. Uberuaga, Defect Structure of Flash-Sintered Strontium Titanate, Journal of the American Ceramic Society 95(8) (2012) 2531-2536.

[19] X. Hao, Y. Liu, Z. Wang, J. Qiao, K. Sun, A novel sintering method to obtain fully dense gadolinia doped ceria by applying a direct current, Journal of Power Sources 210 (2012) 86-91.

[20] A. Gaur, V.M. Sglavo, Densification of $La_{0.6}Sr_{0.4}Co_{0.2}Fe_{0.8}O_3$ ceramic by flash sintering at temperature less than 100 °C, Journal of Materials Science 49(18) (2014) 6321-6332.

[21] A.L. Prette, M. Cologna, V. Sglavo, R. Raj, Flash-sintering of Co_2MnO_4 spinel for solid oxide fuel cell applications, Journal of Power Sources 196(4) (2011) 2061-2065.

[22] E. Zapata-Solvas, S. Bonilla, P. Wilshaw, R. Todd, Preliminary investigation of flash sintering of SiC, Journal of the European Ceramic Society 33(13) (2013) 2811-2816.

[23] S. Grasso, T. Saunders, H. Porwal, B. Milsom, A. Tudball, M. Reece, Flash spark plasma sintering (FSPS) of α and β SiC, Journal of the American Ceramic Society (2016).

[24] Y.H. Dong, I.W. Chen, Thermal Runaway in Mold-Assisted Flash Sintering, Journal of the American Ceramic Society 99(9) (2016) 2889-2894.

[25] S. Grasso, T. Saunders, H. Porwal, O. Cedillos-Barraza, D.D. Jayaseelan, W.E. Lee, M.J. Reece, Flash spark plasma sintering (FSPS) of pure ZrB_2, Journal of the American Ceramic Society 97(8) (2014) 2405-2408.

[26] R.I. Todd, E. Zapata-Solvas, R.S. Bonilla, T. Sneddon, P.R. Wilshaw, Electrical characteristics of flash sintering: thermal runaway of Joule heating, Journal of the European Ceramic Society 35(6) (2015) 1865-1877.

[27] Y. Dong, I.W. Chen, Predicting the Onset of Flash Sintering, Journal of the American Ceramic Society 98(8) (2015) 2333-2335.

[28] Y. Dong, I.W. Chen, Onset Criterion for Flash Sintering, Journal of the American Ceramic Society 98(12) (2015) 3624-3627.

Chapter 6. Electric Field Effect on Grain Growth and Grain Boundary Complexion Transformations

6.1. Introduction

Using electric field and/or current for materials processing has a long history [1]. Since the 1950s, the development and commercialization of a technique later known as Spark Plasma Sintering dramatically accelerated the research on materials processing using electric field [2]. As one of the earliest studies on the effects of electric field on solid-state oxides processing, Mackenzie and co-workers demonstrated improved cation mobility and their relationship with the direction of the external field [3, 4].

Recently, flash sintering, a novel material sintering method using external electric fields, invented by Prof. Raj and his colleagues [5, 6], has attracted significant interests due to its advantages of short densification times and ultra-low furnace temperatures. Flash sintering, together with related techniques like flash SPS [7], has been successfully applied to many materials including YSZ [5], CeO_2 [8], $MgAl_2O_4$ [9], SiC [10], ZnO [11], TiO_2 [12, 13], as well as composites [14, 15] since its invention. Several fundamental studies have successfully modelled and predicted the onset of flash sintering [11, 16, 17] using electric thermal runaway. The fast densifications of green specimens are also explained by the ultra-high heating rate under electric fields [18, 19]. However, many interesting phenomena suggest the possible electric field/current effects on materials' structures beyond Joel heating, although some experiments are not under flash sintering conditions.

For example, anomalous lattice expansion was observed in 8YSZ [20]; reversible cubic-like phase appeared in 3YSZ under electric field and current [21]; abnormal grains were observed at the cathode side in 8YSZ [22] and flash sintered 3YSZ [23]; enhanced grain growth was observed at the anode side in flash sintered ZnO in air [11], but disappeared in flash sintered ZnO in reduced atmosphere [24]. Similar asymmetrical grain growth in the presence of external electric field/current has also been observed in Al_2O_3 [25, 26], $SrTiO_3$ [27], *etc.*

These intriguing observations and fast development of Flash Sintering [28] and Field Assisted Sintering Technologies (FASTs) [29] urge for explorations of the electric field and current effects. Some possible mechanisms have been proposed. For example, electric field interacted with space charge layers which reduces the grain boundary energies and subsequently enhances grain growth [25, 30]; or defects redistribution and electrochemical reduction enhances local cation kinetics, further enhances grain growth [23, 27, 31, 32]**.** Moreover, understanding electric field effects on microstructures is also crucial for improving the stability of electrolytes of like solid-state electrolytes in fuel cells [33], where high current densities and long cycles are desired for industrial applications [34].

In the current study, a classical varistor material, Bi_2O_3-doped ZnO, is used as a model to study the electric field/current effect on microstructure evolutions in the presence of ionic liquid phase. Considering that the densification of green bodies and the grain growth shares similar driving force, pre-sintered specimens are used in this work to decouple them. Specifically, Bi_2O_3-doped ZnO specimens with a special polycrystalline-single crystal-polycrystalline (PC-SC-PC) sandwich

structure were developed. We found highly diversified microstructure evolutions in the sandwich specimens annealed under electric field and current. The grain growth of single crystal towards the opposite direction of the electric field (//-*E*) was significantly enhanced, while grain growth towards the electric field direction (//+*E*) had little difference with specimen annealed without electric field. Bi-enriched highly ordered grain boundary structure was observed at the PC-SC interface where single crystal growth //-*E*, while on the other side, liquid-like intergranular films (IGFs) formed at the grain boundaries. Moreover, near the cathode of the specimen, abnormal grains with strong textures and more than 10 times larger than normal grains were observed. Based on the supportive characterization of photoluminescence at the specimen cross sections, we showed that these phenomena be fully explained by electrochemical polarization of defects through ionic conducting grain boundaries. The advantage of a sandwich specimen is that the asymmetric grain growth was self-comparable, thus ruled out the geometric effect on electric conditions. Also, the ionic insulating but electric conducting single crystal deconvoluted the electric potential and defects electrochemical potential effects on grain growth. The above results indicate that, at least in this work, electrochemical potential dominates the microstructure evolution.

6.2. Experiments

6.2.1. Preparation of dense sandwich specimens

0.5 mol. % Bi_2O_3-doped ZnO powder was prepared by mixing ZnO (99.98% purity, ~ 18 nm, US Nanomaterials) with bismuth acetate (≥99.99% purity, Sigma

Aldrich). Mixed powders were ball-milled for 10 hours with a small amount of isopropyl alcohol. Powders were subsequently dried in oven at 80 °C for 12 hours and annealing at 500 °C for 1 hour.

ZnO $(11\bar{2}0)$ single crystals with both sides polished were purchased from MTI Corporation. Dense Bi_2O_3-doped ZnO polycrystalline-single crystal-polycrystalline (PC-SC-PC) sandwich pellets were prepared by SPS at 780 °C for 5 minutes under 50 MPa pressure, then de-carbonized at 700 °C for 9 hours. After sintering, sandwich specimens reached > 99% relative densities. All sandwich pellets were ground to 5.0 × 5.0 × ~1.6 mm^3 cuboids with 0.5 mm thick single crystal ZnO between two non-connecting polycrystalline regions.

6.2.2. Annealing with electric field/current

Dense sandwich specimens were sputtered with platinum to form two 5.0 × 5.0 mm^2 electrodes using a Denton Discover 18 Sputter System. An external DC electric field were applied on the specimen while annealing at 840 °C for 4 hours with a controlled DC current density J = 6.4 mA/mm^2. The nominal electric field direction was perpendicular to imbedded ZnO $(11\bar{2}0)$ single crystals. More details of the equipment were shown in a previous publication [18].

6.2.3. Annealing without electric field/current

To rule out the Joel heating effect of electric field, the reference sandwich specimen was annealed at 30 °C higher (870 °C) for 4 hours on the same equipment without any external electric field. The annealing temperature of the reference specimen is above the upper limit of the experiment specimen. The

method used for temperature estimation with respect to power density is described in a previous publication [11]. After isothermal annealing, specimens were air-quenched to room temperature.

Additionally, three dense polycrystalline specimens were prepared by SPS and de-carbonized at the same condition described above, then annealed at 880 °C for 4 hours without electric field in air, argon, or argon + 5% H_2.

6.2.4. Characterization

Bulk densities of sandwich specimens were measured using the Archimedes method. Electric potentials and currents of specimens and circuits were recorded using a high- precision digital multimeter (Tektronix DMM 4050, Beaverton, OR, USA) during the experiments. Quenched specimens were characterized by using an ultra-high-resolution Scanning Electron Microscope (Apreo SEM, FEI, Hillsboro, OR) at the cross sections after grinding and polishing. Grain growth of the single crystal was measured at 14 locations along each polycrystalline-single interface. At each location, grain growth was averaged from 16 measurements with 5 μm intervals. Spatial-resolved photoluminescence spectroscopy in the wavelength range from 400 nm to 700 nm on cross section surface of sandwich specimens was carried out on a confocal microscope (Leica SP5, Leica Microsystems) equipped with Multiphoton (MP) system. Microscope spatial resolution and penetration depth was ~ 0.4 μm and ~ 50 nm, respectively. Transmission electron microscopy samples were prepared by using a Dual Beam Focused Ion Beam (FIB) / SEM system (Scios, FEI, Hillsboro, OR). Aberration-

corrected scanning transmission electron microscopy characterization of the grain boundary structures was conducted by using a JEOL JEM-300CF STEM microscope operated at 300 kV. Electron backscattered diffraction (EBSD) mapping was acquired by using an c-wave detector from Oxford Instruments (Concord, MA, USA).

6.3. Results and Discussion

6.3.1. Electric Field Effects on Grain Growth of Bi_2O_3-doped ZnO

Prior to characterize the effect of electric field and current, grain growth of single crystals after SPS and decarbonization was characterized as a baseline before annealing experiments as shown in Fig. 6.1. Aligned holes are used to label the original single crystal surfaces. The grain growths on both sides of SC are very small and have little difference, which indicates a symmetric microstructure of the sandwich specimen before further annealing experiments.

As described in the experimental section, a sandwich specimen was annealed at 870 °C for 4 hours without an external electric field. The microstructure is symmetric as shown in Fig. 6.2. The single crystal growths of the reference specimen were 3.63 ± 0.91 μm and 3.60 ± 0.79 μm on both sides respectively.

However, by annealing the sample under DC electric field with constant a current density J = 6.4 mA/mm^2. asymmetric microstructure was clearly observed as shown in Fig. 6.3. The nominal direction of the external electric field (white arrows), location of high-magnification micrographs (dashed orange squares in Fig. 6.3(a)), as well as the direction of grain growth (blue arrows) were labelled.

Significant grain growth anti-parallel to the electric field direction (//-E) was observed. Well on the other hand, grain growth parallel to electric field (//+E) was comparable to the reference specimen. Quantitative grain growth versus the normalized location on the single crystal surfaces were summarized in Fig. 6.4 (b). Peak of the average grain growth of SC //-E was > 200% larger than the average of grain growth of SC//+E.

In addition to grain growth, pores were observed near the single crystal at the side with small grain growth (SC//+E). Since all the sandwich specimens were pre-densified to more than 99% relative density, and no extra porosity was observed in the reference specimen, the pores are expected to be generated during the annealing under electric field.

6.3.2. Electrochemical Polarization of Defects and Ionic Blocking Single Crystal

Defect concentrations has been demonstrated to affect microstructure evolutions in many materials[23, 27]. In this study, polarization of defects by external electric field was clearly characterized by spatial-resolved photoluminescence (PL) spectroscopy, explains the asymmetric microstructure formation of the sandwich Bi_2O_3-doped ZnO specimens under external electric field. Figure 4 shows both low and high magnification PL spectra in the wavelength ranging from 400 nm to 700 nm. Each PL spectrum in Fig. 6.5 (a, b) is an average of the intensity in the 30 μm × 1.5 μm boxes as shown in the mappings, Fig. 6.5 (c, d), respectively. Locations close to the single crystal surface growing //-E has

much higher intensities than locations near the anode. Detailed peak separations of two representative spectra were plotted in Figure 5. The broad asymmetric peak from 400 nm to 700 nm in both locations is a superposition of two peaks. In Fig. 6.6 (a) the two separated peaks centered at 523 nm and 610 nm, which are close to the corresponding PL wavelengths of $V_O^{\bullet}$ and O_i^{-} defects in ZnO. In Fig. 6.6 (b), the two separated peaks are centered at 505 nm and 577 nm. The PL signal in single crystal region is below the detection limit in the wavelength range of interest, leaving a dark area in the spatial mapping as can be seen in Fig. 6.5 (c, d). Moreover, as shown in the high magnification PL spectra (Fig. 6.5(b)), the grown region (Location ID = 6) of the single crystal (//-E) has lower intensity than the adjacent polycrystalline region (Location ID = 7). Polycrystalline region near the interface //+E has lower intensity than the interface //-E.

The significant difference of PL spectra at different locations reveals how external electric field affects the defect concentrations in the sample. This interesting polarization behavior of ionic defects in Bi_2O_3-doped ZnO is believed due to the combined effects of ionic conducting grain boundary liquid and electric conducting bulk. At the annealing temperature of 840 °C, Bi-rich grain boundaries are good ionic conductors in liquid phase as has been demonstrated by works on Bi_2O_3-based oxygen membranes [35]. On the other hand, bulk ZnO is electric conducting dominated. So, in the sandwich specimens of this work, the Bi-doped single crystal ZnO between two Bi_2O_3-doped ZnO polycrystalline parts is an ionic blocking layer, forming continuous electric potential but “discontinuous” (in microscale) chemical potential of ionic defects along the external electric field

direction. Noting that the chemical potential of defects across the PC-SC interfaces are physically continuous. However, the transition layer cannot be observed due to the slow ion diffusions of ZnO single crystals [36] given the 0.4 μm spatial resolution of the microscope. Though commercial ZnO single crystals' defect concentrations are very low, the grown part of the single crystal is defected according to the PL spectra at location 6, Fig. 6.5 (b). This is similar to the crystal growth behavior of ZnO from molten salts [37]. However, it is worth noting that, at current stage, it is not possible to differentiate the luminescence from the bulk and the grain boundary in the polycrystalline regions.

6.3.3. Proposed Mechanism and Schematic Potential Profiles

The above observations of ionic conducting grain boundaries and ionic blocking single crystals lead to the proposed mixed conducting mechanism as shown in Fig. 6.7. The mixed conducting mechanism explained the microstructure evolution by electrochemical polarization of defects across the sandwich specimen under external electric field and current. Using O^{2-}/O^{-} and $V_O^{\bullet\bullet}$ as examples, positive ionic charge carriers at the polycrystalline grain boundaries, $V_O^{\bullet\bullet}$, are oversaturated at SC front growing //-E as well as the location near the cathode, forming reduced environment locally in the sandwich specimen. On the other hand, negative ionic charge carriers, O^{2-}/O^{-}, oversaturated at the SC front growing //+E and the anode, forming local oxidized environment, which possible oxygen precipitation resulting porous structures. This proposed mechanism explains the gradient of PL intensity and pore formations as shown in Fig. 6.5 and Fig. 6.3 (a).

Additional experiments without electric field demonstrated that inert or reducing atmospheres will enhanced the grain growth. Bi_2O_3-doped ZnO was quenched from 880 °C after annealing for 4 hours in air, argon, or argon + 5% H_2. As shown in Fig. 6.8, average grain size of specimen annealed in air is 2.02 ± 0.17 μm. But specimen annealed in argon and argon + 5% H_2 have larger grain sizes of 3.47 ± 0.51 μm and 5.18 ± 0.60 μm, respectively. This result agrees with the grain growth behavior in the sandwich specimen and the proposed mixed conducting mechanism. Presumably, in the presence of ionic liquid at grain boundaries, electric field/current changes local defects concentration, further decreases the space charges at grain boundaries, and subsequently enhanced grain growth. Electric reduction also significantly enhanced grain growth near the Cathode where abnormal grain growth in polycrystalline was observed, which is further discussed in section 6.3.4.

The formation of defect gradients in the polycrystalline regions also reveals that the rate-limiting steps are defect reactions. Different from experiment setups and modelling of SOFCs where the environment oxygen partial pressures are significantly different on cathode and anode sides, this work is carried out under uniform environmental oxygen partial pressure. Using the region near specimen cathode as an example, under diffusion-control condition (in another word, the defect reaction with the environmental is fast with respect to the electric field driven diffusion), there will be minimal oversaturation of $V_O^{\bullet\bullet}$, which is apparently not the case in this work. Under reaction-control condition, a thin layer with oxygen partial drop will form near the surface of the cathode, and a large chemical potential

gradient of $V_O^{\bullet\bullet}$ will form in the bulk of polycrystalline. This agrees with the observation in the current case. Additionally, the grain growth of Bi_2O_3-doped ZnO is also reaction controlled [38]. Overall, grain boundary $V_O^{\bullet\bullet}$ defect reactions with either environment or the bulk are slow with respect to its diffusion, which are also reasons for the observation of electrothermal polarization of defects in this work.

The profiles of oxygen partial pressure (μ_{O_2}), electric potential (ϕ), chemical potential of ionic oxygens ($\mu_{O^{2-}}$), and electrochemical potential of ionic oxygens ($\eta_{O^{2-}}$) *vs.* position can be complex due to the uncertainties of boundary conditions at the polycrystalline-single crystal interfaces. By assuming the single crystal ZnO is a perfect ionic insulator and has slow oxygen diffusion, the chemical potential of oxygen is sketched following the SOFC electrochemical studies [39]. A nonlinearity is believed to exist due to the local ionic transport number (t_O) difference, which is a result of change in electronic conductivity *vs.* oxygen partial pressure in mixed conducting materials. Similarly, the electric potential and chemical potential of O^{2-} are also plotted. Electric potential is continuous considering the electric conducting nature of the single crystal layer. However, it is not differentiable at the interfaces due to the change of media. Similarly, the chemical potential of ionic oxygen is plotted by assuming a local equilibrium defect reaction $O^{2-} = \frac{1}{2}O_2 + 2e^-$. The electrochemical potential of O^{2-}, $\eta_{O^{2-}} = \mu_{O^{2-}} - 2e\phi$, is also nonlinear because at region with low ionic oxygen transport number, the gradient of $\mu_{O^{2-}}$l contributes to the electrochemical gradient in addition to the constant term at constant total current density and total conductivity[40]:

$$\frac{\partial \eta_{O^{2-}}}{\partial x} = \frac{2eJ_{tot.}}{\sigma_{tot.}} + (1 - t_O)\frac{\partial \mu_{O^{2-}}}{\partial x}$$

In which $\Delta\mu_e = 0$, is assumed to be 0 given the same electrodes. Again, both chemical potentials and electrochemical potentials at PC-SC interfaces are physically continuous, which are simplified in the sketches.

6.3.4. Electric Field Effects on Grain Boundary Complexion and Cathode Textures

Metallic-like Bi IGFs have been observed at locations that are electrochemically reduced. Fig. 6.9 is a summary of the HAADF and BF images of PC-SC grain boundary growing //+*E*, //-*E*, and without *E* (the reference). Reference grain boundaries without *E* have amorphous films ~ 1 nm thick as shown in Fig. 6.9 (e, f), which is reasonable for specimens quenched from liquid phase temperature. At the single crystal grain boundary //+E, where an oxidized environment is expected, similar amorphous structure is observed (Fig. 6.9 (a, b)). However, at the single crystal grain boundary //-E, where a strong electrochemical reduction is expected, highly ordered bilayer or trilayer was observed. The high brightness at the grain boundary in the HAADF image indicates that the grain boundary is enriched with ordered Bi atoms.

The possibility of reducing the grain boundary to metallic Bi is justified by estimating the local oxygen partial pressure at the polycrystalline-single crystal grain boundary. In the estimation, the sandwich specimen is treated as serial resistors under constant current density. Estimated electric potential difference across one polycrystalline region is ~ 0.7 V. Oxygen partial pressure required to

reduce Bi_2O_3 at the annealing temperature of this work, 840 °C, is only 10^{-10} ~ 10^{-11} atm according to Ellingham Diagrams [41]. The electrochemical reduction at the PC-SC interface provides an equivalent oxygen partial pressure ~ 10 orders of magnitude lower. Thus, it is not surprising to observe the metallic-like grain boundary complexion.

As discussed in section 6.3.2, polarization of ionic defects exists in both polycrystalline regions. Area close to specimen cathode are also highly electrochemically reduced. Fig. 6.10 (b) shows the abnormal grains close to the cathode. More interestingly, strong textures of the abnormal grains are observed under EBSD. Fig. 6.10 (c) shows the inverse pole figure with Y axis as reference, which is the same as the nominal direction of external electric field. (11-20) is clearly identified as a strong preferred orientation under electric field and current. Other orientations like (01-10) maybe preferred as well. Similar to SC-PC grain boundary growing //-E, the grain boundaries of the abnormal grains are also highly ordered. These results, again, support the mixed conducting mechanism proposed in section 6.3.3. By comparing the profiles of electric potential and electrochemical potential near the cathode and the PC-SC interfaces growing //+E, it is reasonable to believe that, at least in this study, the external electric field guided the microstructure evolution through electrochemical potential, rather than electric potential directly.

6.4. Conclusions

In this study, polycrystalline - single crystal - polycrystalline (PC-SC-PC) sandwich Bi_2O_3-doped ZnO specimens were designed to study the effect of external electric field/current on the microstructure evolution. Asymmetric grain growth of SC was observed after annealing at liquid phase temperature with external electric field. Photoluminescence of quenched specimen shows polarization of defects in PC regions and ionic blocking SC region. Enhanced grain growths were observed at electrochemically reduced locations. This grain growth behavior was also confirmed in reduced atmosphere without external electric field. Subsequently, a mixed conducting mechanism was proposed that explains the microstructure evolution including enhanced SC grain growth, pore formation, and abnormal grain growth. Grain boundary reduction and complexion transitions happened at locations that are electrochemically reduced. Specifically, ordered metallic-like grain boundaries with 2 – 3 atomic layers of enriched Bi were observed. In the current study, external electric field is believed to affect microstructure evolution electrochemically.

Chapter 6, in part, is a reprint of manuscript “Electric Field Effect on Grain Growth and Grain Boundary Complexion” J. Nie, and J. Luo, in preparation. The dissertation author was the primary investigator and author of this paper.

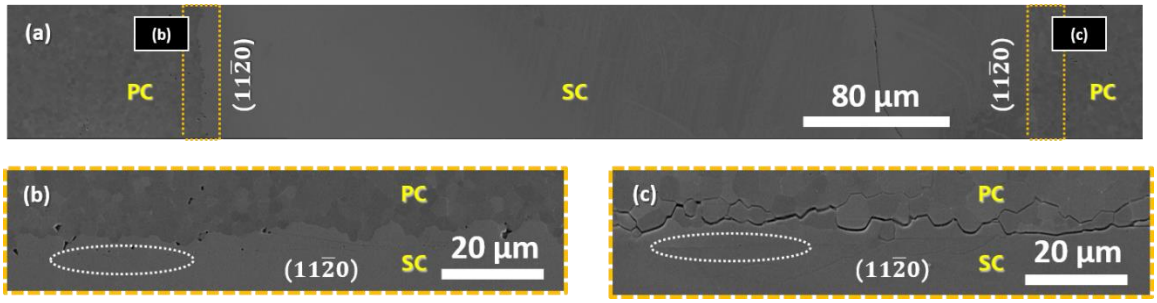

Figure 6.1 (a) Cross-sectional SEM micrograph of Bi_2O_3 doped ZnO polycrystalline-single crystal-polycrystalline sandwich specimen annealed at 700 °C for 9 hours after densified using SPS. (b, c) High magnification SEM micrographs of the single crystal-polycrystalline interfaces on two sides of the single crystal. Aligned holes are circled in (b) and (c) and used to label the original single crystal surfaces.

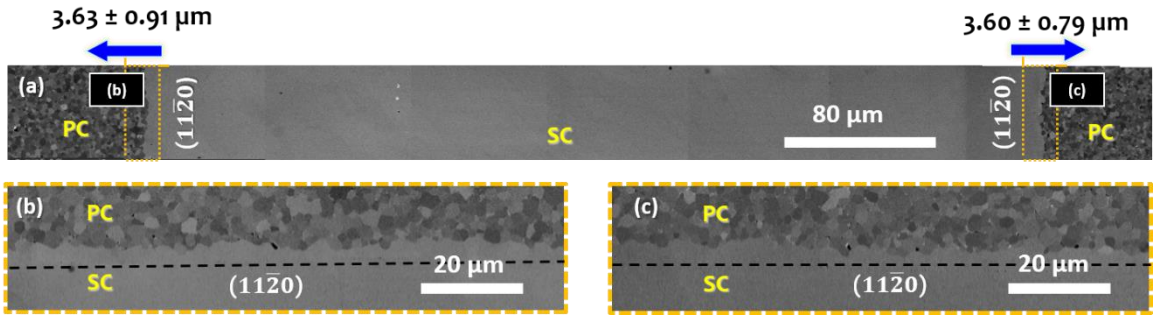

Figure 6.2 (a) Cross-sectional SEM micrograph of Bi_2O_3 doped ZnO polycrystalline-single crystal-polycrystalline sandwich specimen quenched from 880 °C after annealing for 4 hours without any external electric field/current. (b, c) High magnification SEM micrographs of the single crystal-polycrystalline interfaces on two sides of the single crystal. Black dashed lines indicate the original single crystal boundaries. The single crystal growth on two sides are similar. Average single crystal growths on both sides are quantitively measured as shown in Fig. 6.4 (b).

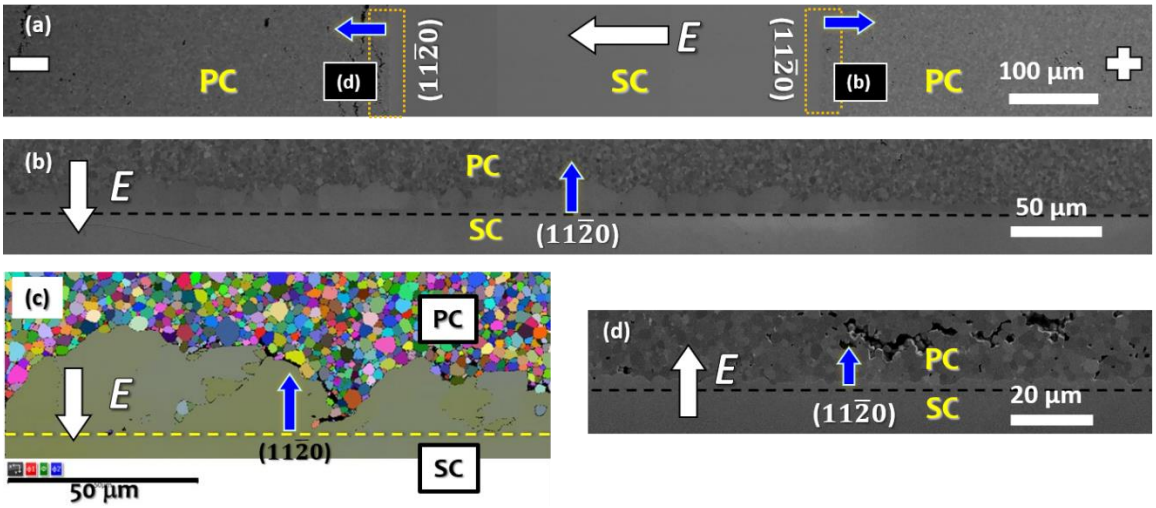

Figure 6.3 (a) Cross-sectional SEM micrograph of Bi_2O_3 doped ZnO polycrystalline-single crystal-polycrystalline sandwich specimen quenched from 840 °C after annealing for 4 hours with constant current density J = 6.4 mA/mm^2. Direction of the external electric field was from right to left as labelled on the micrograph (b) High magnification SEM micrograph and (c) EBSD Euler mapping of the single crystal growth parallel to the negative electric field direction (//-E). (d) High magnification SEM micrograph of the single crystal growth parallel to the electric field direction (//+E). Black or yellow dashed lines indicate the original single crystal boundaries. The single crystal growth //-E is significant larger than the growth //+E. Average single crystal growths on both sides are quantitively measured as shown in Fig. 6.4 (b).

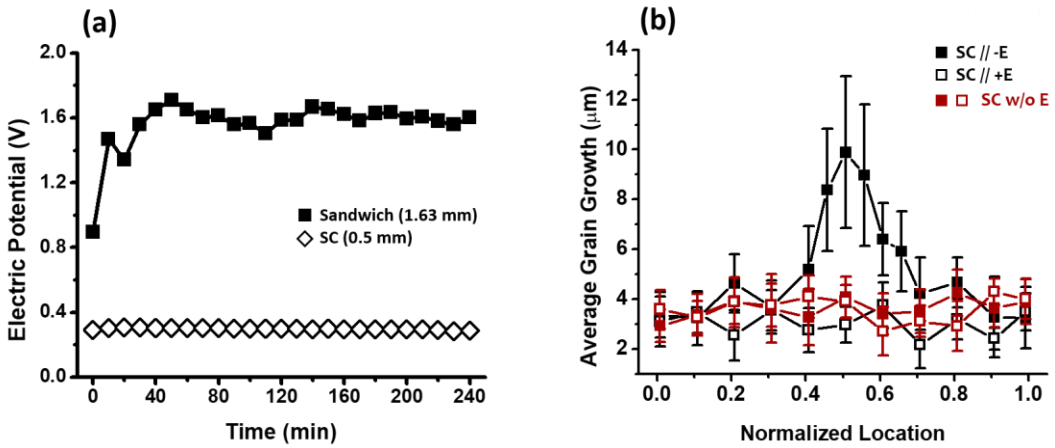

Figure 6.4 (a) Electric potential *vs.* annealing time of Bi_2O_3-doped ZnO sandwich specimen and single crystal with current density J = 6.4 mA/mm^2 at 840 °C. (b) Average single crystal growth (both sides) of Bi_2O_3-doped ZnO sandwich specimen annealed at 880 °C without electric field/current (SC w/o E) and sandwich specimen annealed at 840 °C with constant current density J = 6.4 mA/mm^2 (SC//-E and SC//+E).

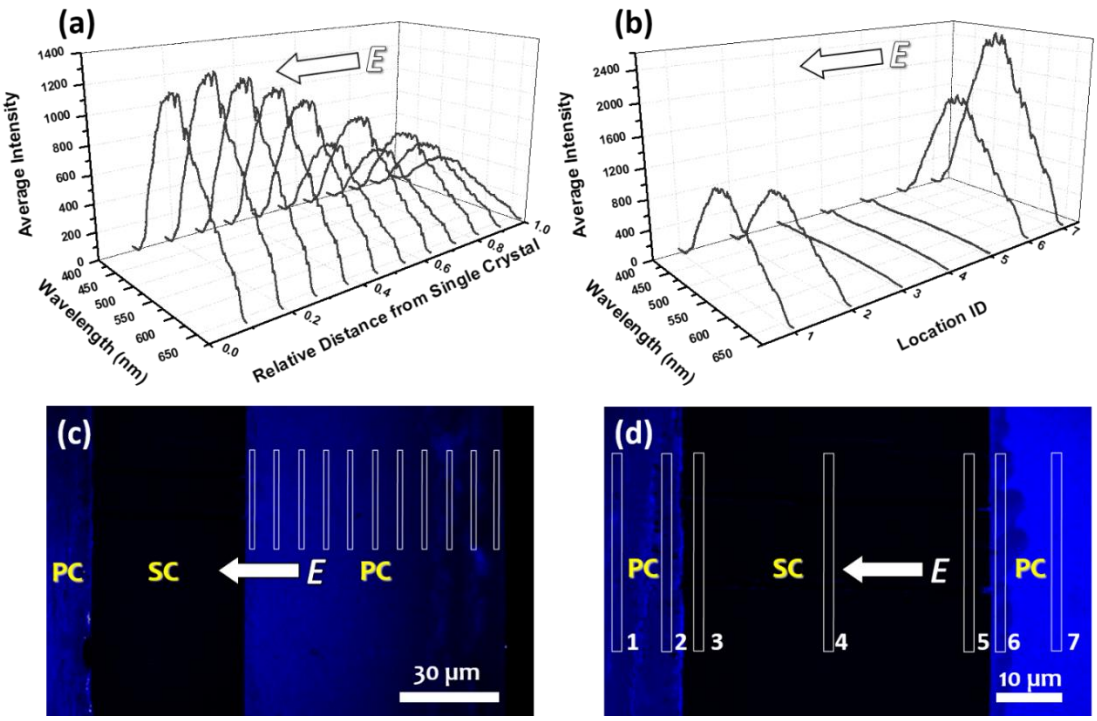

Figure 6.5 (a, b) Average photoluminescence (PL) intensity *vs.* wavelength of Bi_2O_3-doped ZnO sandwich specimen annealed with current density J = 6.4 mA/mm^2 at 840 °C. PL spectroscopy was recorded by averaging the intensities in boxes of 30 μm x 1.5 μm at different locations as shown in (c, d), respectively. (c, d) Mapping of PL at 526 nm of Bi_2O_3-doped ZnO sandwich specimen annealed with current density J = 6.4 mA/mm^2 at 840 °C. In the polycrystalline region on the anode side, locations near the single crystal-polycrystalline interface have higher PL intensity. Grown part of single crystal has lower PL intensity than the adjacent polycrystalline region, higher PL intensity than the polycrystalline region on the negative cathode side.

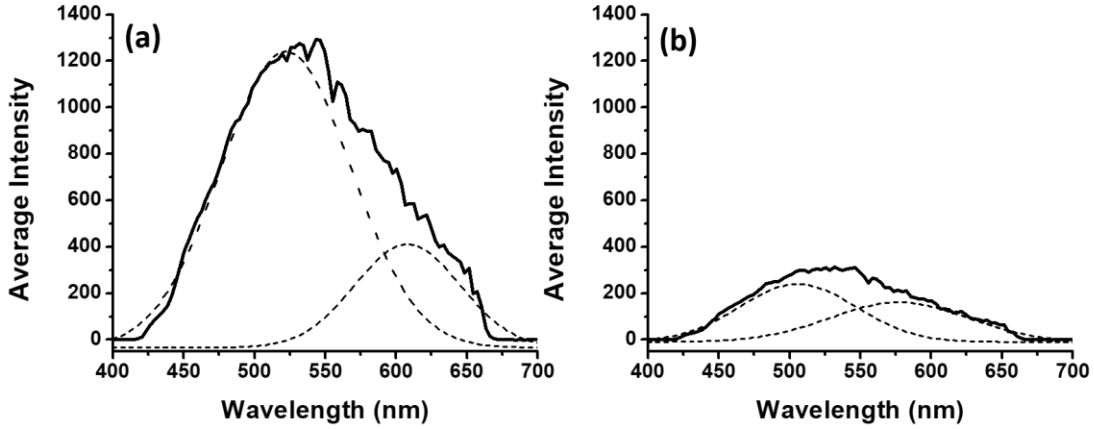

Figure 6.6 Average photoluminescence (PL) intensity *vs.* wavelength in the polycrystalline region on the anode side of Bi_2O_3-doped ZnO sandwich specimen annealed with current density J = 6.4 mA/mm^2 at 840 °C at different locations: (a) near the single crystal-polycrystalline interface and (b) near the anode. PL spectroscopy were recorded by averaging the intensities in boxes of 30 μm x 1.5 μm as shown in Fig. 6.5 (c). The broad PL peak in (a) was separated into peaks centered at 523 nm and 610 nm. The broad PL peak in (b) was separated into peaks centered at 505 nm and 577 nm.

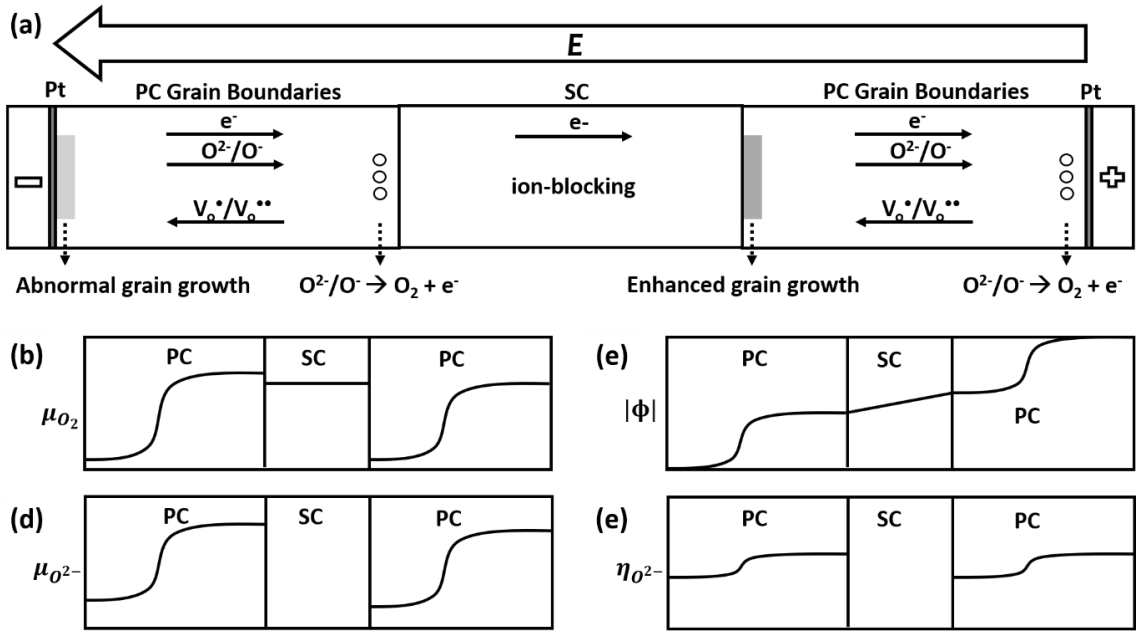

Figure 6.7 (a) The schematic of defects polarization in a polycrystalline – single crystal – polycrystalline (PC-SC-PC) sandwich specimen under external electric field, where grain boundaries in two PC regions are mixed conducting, and SC is electric conducting. O^{2-}/O^{-} and $V_O^{\bullet\bullet}$ pairs are used as examples. (b – e) The schematic profiles of oxygen partial pressure (μ_{O_2}), electric potential (ϕ), chemical potential of ionic oxygens ($\mu_{O^{2-}}$), and electrochemical potential of ionic oxygens ($\eta_{O^{2-}}$) *vs.* position.

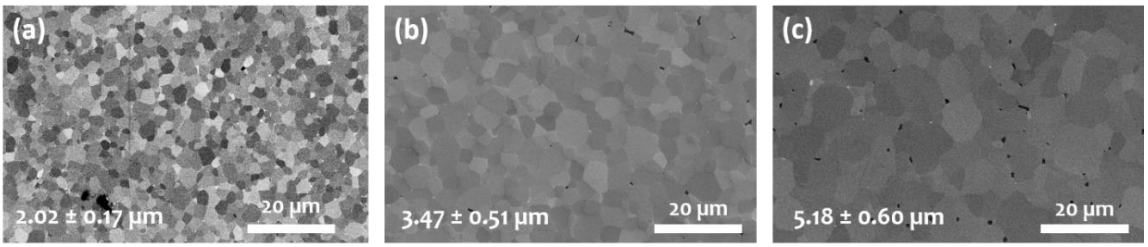

Figure 6.8 Cross-sectional SEM micrographs of Bi_2O_3 doped ZnO polycrystalline specimens quenched from 880 °C after annealing for 4 hours in (a) air, (b) argon, and (c) argon + 5% H_2. The measured average grain sizes of specimens annealed in air and argon are 2.02 ± 0.17 µm, 3.47 ± 0.51 µm, and 5.18 ± 0.60 µm, respectively.

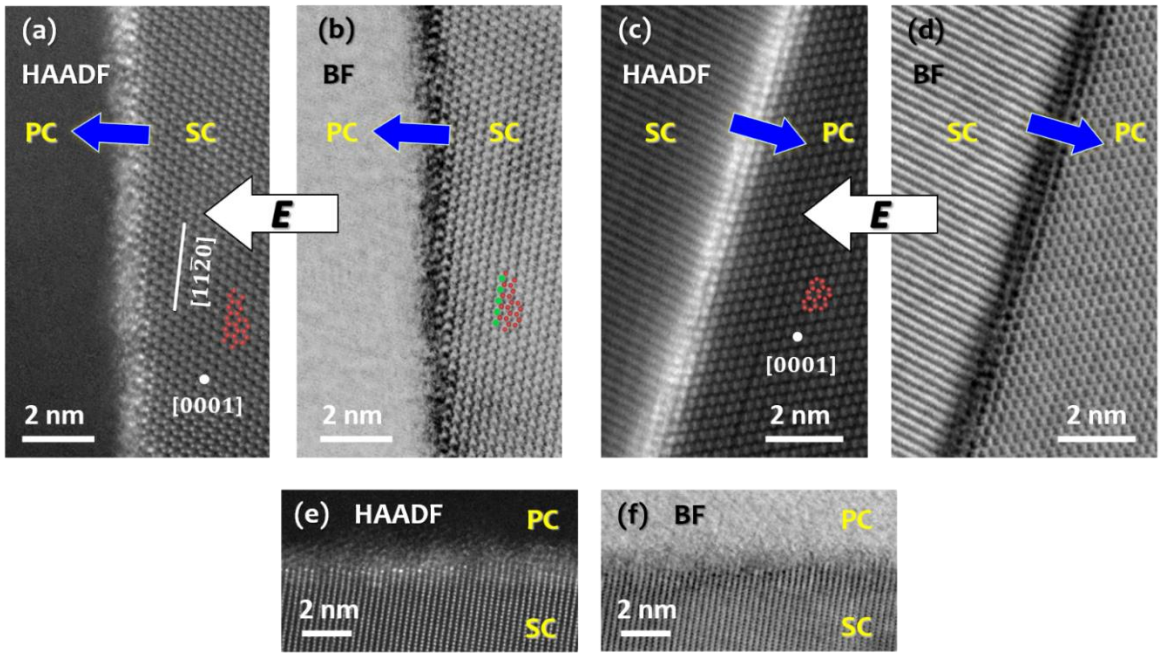

Figure 6.9 Aberration-corrected HAADF and BF STEM images of polycrystalline-single crystal grain boundaries (a, b) // + *E* and (c, d) // - *E* in Bi_2O_3 doped ZnO sandwich specimen quenched from 840 °C after annealing for 4 hours with constant current density J = 6.4 mA/mm^2. (e, f) Aberration-corrected HAADF and BF STEM images of the polycrystalline-single crystal grain boundary in Bi_2O_3 doped ZnO sandwich specimen quenched from 840 °C annealing for 4 hours without electric field or current.

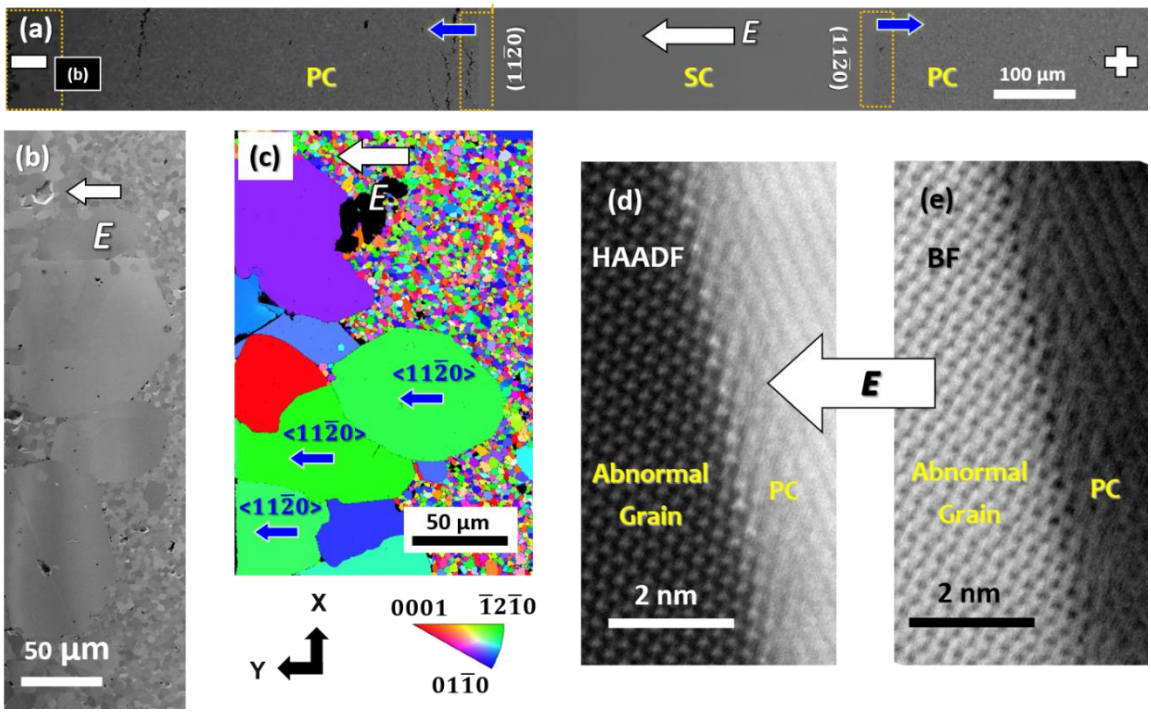

Figure 6.10 (a, b) Cross-sectional SEM and (c) Y-IPF EBSD micrographs of the abnormal grains near the cathode of Bi_2O_3 doped ZnO polycrystalline-single crystal-polycrystalline sandwich specimen quenched from 840 °C after annealing for 4 hours with constant current density J = 6.4 mA/mm^2. (d, e) Aberration-corrected HAADF and BF STEM images of grain boundary between an abnormal grain and other poly crystalline.

References

[1] S. Grasso, Y. Sakka, G. Maizza, Electric current activated/assisted sintering (ECAS): a review of patents 1906-2008, Science and Technology of Advanced Materials 10(5) (2009).

[2] Z.A. Munir, U. Anselmi-Tamburini, M. Ohyanagi, The effect of electric field and pressure on the synthesis and consolidation of materials: A review of the spark plasma sintering method, Journal of Materials Science 41(3) (2006) 763-777.

[3] K.J.D. Mackenzie, R.K. Banerjee, M.R. Kasaai, EFFECT OF ELECTRIC-FIELDS ON SOLID-STATE REACTIONS BETWEEN OXIDES .1. REACTION BETWEEN CALCIUM AND ALUMINUM-OXIDES, Journal of Materials Science 14(2) (1979) 333-338.

[4] K.J.D. Mackenzie, M.J. Ryan, EFFECT OF ELECTRIC-FIELDS ON SOLID-STATE REACTIONS BETWEEN OXIDES .3. INTER-DIFFUSION IN POLYCRYSTALLINE MAGNESIUM AND ALUMINUM-OXIDE PELLETS, Journal of Materials Science 16(3) (1981) 579-588.

[5] M. Cologna, B. Rashkova, R. Raj, Flash Sintering of Nanograin Zirconia in < 5 s at 850 °C, Journal of the American Ceramic Society 93(11) (2010) 3556-3559.

[6] M. Cologna, A.L. Prette, R. Raj, Flash-Sintering of Cubic Yttria-Stabilized Zirconia at 750 °C for Possible Use in SOFC Manufacturing, Journal of the American Ceramic Society 94(2) (2011) 316-319.

[7] C. Maniere, G. Lee, E.A. Olevsky, All-Materials-Inclusive Flash Spark Plasma Sintering, Scientific Reports 7 (2017).

[8] X.M. Hao, Y.J. Liu, Z.H. Wang, J.S. Qiao, K.N. Sun, A novel sintering method to obtain fully dense gadolinia doped ceria by applying a direct current, Journal of Power Sources 210 (2012) 86-91.

[9] B. Yoon, D. Yadav, S. Ghose, R. Raj, Reactive flash sintering: MgO and alpha-Al_2O_3 transform and sinter into single-phase polycrystals of $MgAl_2O_4$, Journal of the American Ceramic Society 102(5) (2019) 2294-2303.

[10] E. Zapata-Solvas, S. Bonilla, P.R. Wilshaw, R.I. Todd, Preliminary investigation of flash sintering of SiC, Journal of the European Ceramic Society 33(13-14) (2013) 2811-2816.

[11] Y.Y. Zhang, J.I. Jung, J. Luo, Thermal runaway, flash sintering and asymmetrical microstructural development of ZnO and ZnO-Bi_2O_3 under direct currents, Acta Materialia 94 (2015) 87-100.

[12] Y.Y. Zhang, J.Y. Nie, J. Luo, Effects of phase and doping on flash sintering of TiO_2, Journal of the Ceramic Society of Japan 124(4) (2016) 296-300.

[13] B. Yoon, D. Yadav, R. Raj, E.P. Sortino, S. Ghose, P. Sarin, D. Shoemaker, Measurement of O and Ti atom displacements in TiO_2 during flash sintering experiments, Journal of the American Ceramic Society 101(5) (2018) 1811-1817.

[14] A. Gaur, V.M. Sglavo, Flash Sintering of (La, Sr)(Co, Fe)O_3-Gd-Doped CeO_2 Composite, Journal of the American Ceramic Society 98(6) (2015) 1747-1752.

[15] B. Du, S.T. Zhou, X.H. Zhang, C.Q. Hong, Q. Qu, Preparation of a high spectral emissivity TaSi2-based hybrid coating on SiOC-modified carbon-bonded carbon fiber composite by a flash sintering method, Surface & Coatings Technology 350 (2018) 146-153.

[16] R. Todd, E. Zapata-Solvas, R. Bonilla, T. Sneddon, P. Wilshaw, Electrical characteristics of flash sintering: thermal runaway of Joule heating, Journal of the European Ceramic Society 35(6) (2015) 1865-1877.

[17] Y.H. Dong, I.W. Chen, Onset Criterion for Flash Sintering, Journal of the American Ceramic Society 98(12) (2015) 3624-3627.

[18] Y.Y. Zhang, J.Y. Nie, J.M. Chan, J. Luo, Probing the densification mechanisms during flash sintering of ZnO, Acta Materialia 125 (2017) 465-475.

[19] W. Ji, B. Parker, S. Falco, J.Y. Zhang, Z.Y. Fu, R.I. Todd, Ultra-fast firing: Effect of heating rate on sintering of 3YSZ, with and without an electric field, Journal of the European Ceramic Society 37(6) (2017) 2547-2551.

[20] E.K. Akdogan, I. Savkliyildiz, H. Bicer, W. Paxton, F. Toksoy, Z. Zhong, T. Tsakalakos, Anomalous lattice expansion in yttria stabilized zirconia under simultaneous applied electric and thermal fields: A time-resolved in situ energy dispersive x-ray diffractometry study with an ultrahigh energy synchrotron probe, Journal of Applied Physics 113(23) (2013).

[21] J.M. Lebrun, T.G. Morrissey, J.S.C. Francis, K.C. Seymour, W.M. Kriven, R. Raj, Emergence and Extinction of a New Phase During On-Off Experiments Related to Flash Sintering of 3YSZ, Journal of the American Ceramic Society 98(5) (2015) 1493-1497.

[22] S.W. Kim, S.G. Kim, J.I. Jung, S.J.L. Kang, I.W. Chen, Enhanced Grain Boundary Mobility in Yttria-Stabilized Cubic Zirconia under an Electric Current, Journal of the American Ceramic Society 94(12) (2011) 4231-4238.

[23] Y.H. Dong, H.R. Wang, I.W. Chen, Electrical and hydrogen reduction enhances kinetics in doped zirconia and ceria: I. grain growth study, Journal of the American Ceramic Society 100(3) (2017) 876-886.

[24] J. Luo, The scientific questions and technological opportunities of flash sintering: From a case study of ZnO to other ceramics, Scripta Materialia 146 (2018) 260-266.

[25] J.H. Han, D.Y. Kim, Effect of external electric field on the boundary migration of Al_2O_3 ceramics, Japan Inst Metals, Sendai, 2001.

[26] J.I. Choi, J.H. Han, D.Y. Kim, Effect of titania and lithia doping on the boundary migration of alumina under an electric field, Journal of the American Ceramic Society 86(4) (2003) 640-643.

[27] W. Rheinheimer, M. Fulling, M.J. Hoffmann, Grain growth in weak electric fields in strontium titanate: Grain growth acceleration by defect redistribution, Journal of the European Ceramic Society 36(11) (2016) 2773-2780.

[28] M. Cologna, B. Rashkova, R. Raj, Flash Sintering of Nanograin Zirconia in < 5 s at 850 °C, Journal of the American Ceramic Society 93(11) (2010) 3556-3559.

[29] S. Grasso, T. Saunders, H. Porwal, B. Milsom, A. Tudball, M. Reece, Flash spark plasma sintering (FSPS) of α and β SiC, Journal of the American Ceramic Society (2016).

[30] H. Conrad, D. Yang, Dependence of the sintering rate and related grain size of yttria-stabilized polycrystalline zirconia (3Y-TZP) on the strength of an applied DC electric field, Materials Science and Engineering a-Structural Materials Properties Microstructure and Processing 528(29-30) (2011) 8523-8529.

[31] J.M. Lebrun, R. Raj, A First Report of Photoemission in Experiments Related to Flash Sintering, Journal of the American Ceramic Society 97(8) (2014) 2427-2430.

[32] S.K. Jha, X.L. Phuah, J. Luo, C.P. Grigoropoulos, H.Y. Wang, E. Garcia, B. Reeja-Jayan, The effects of external fields in ceramic sintering, Journal of the American Ceramic Society 102(1) (2019) 5-31.

[33] M.A. Laguna-Bercero, R. Campana, A. Larrea, J.A. Kilner, V.M. Orera, Electrolyte degradation in anode supported microtubular yttria stabilized zirconia-based solid oxide steam electrolysis cells at high voltages of operation, Journal of Power Sources 196(21) (2011) 8942-8947.

[34] F. Tietz, D. Sebold, A. Brisse, J. Schefold, Degradation phenomena in a solid oxide electrolysis cell after 9000 h of operation, Journal of Power Sources 223 (2013) 129-135.

[35] V.V. Belousov, Oxygen-permeable membrane materials based on solid or liquid Bi2O3, Mrs Communications 3(4) (2013) 225-233.

[36] W.J. Moore, E.L. Williams, DIFFUSION OF ZINC AND OXYGEN IN ZINC OXIDE, Discussions of the Faraday Society (28) (1959) 86-93.

[37] Z.Y. Jiang, T. Xu, Z.X. Xie, Z.W. Lin, X. Zhou, X. Xu, R.B. Huang, L.S. Zheng, Molten salt route toward the growth of ZnO nanowires in unusual growth directions, Journal of Physical Chemistry B 109(49) (2005) 23269-23273.

[38] D. Dey, R.C. Bradt, GRAIN-GROWTH OF ZNO DURING Bi_2O_3 LIQUID-PHASE SINTERING, Journal of the American Ceramic Society 75(9) (1992) 2529-2534.

[39] Y.H. Dong, I.W. Chen, Oxygen potential transition in mixed conducting oxide electrolyte, Acta Materialia 156 (2018) 399-410.

[40] P. Kofstad, T. Norby, Defects and transport in crystalline solids, (2007).

[41] G. Muller, A. Heinzel, G. Schumacher, A. Weisenburger, Control of oxygen concentration in liquid lead and lead-bismuth, Journal of Nuclear Materials 321(2-3) (2003) 256-262.

Chapter 7. Dissertation Summary and Research Prospects

In this dissertation, a quantitative thermodynamic model of subeutectic intergranular films and high-resolution transmission electron microscopy experiments were combined to explain the mystery of enhanced sintering in CuO-doped TiO_2. The first grain boundary λ diagram was calculated to represent the thermodynamic tendency for general grain boundaries in CuO-doped TiO_2 to disorder. In future studies, similar or different (more rigorous and sophisticated) types of GB diagrams should be computed for other ceramic materials, which can potentially have broad scientific and technological impacts.

Motivated by the advancement of electric field assisted sintering technologies, we investigated Al_2O_3 *vs.* Bi_2O_3 doping effects on the flash sintering of ZnO. As an example of bulk aliovalent dopant, Al increased the specimen conductivity to promote flash sintering. The onset flash occurred as natural thermal runaway. Ultrafast field-induced migration of aliovalent cations during the flash sintering of Al_2O_3-doped ZnO were observed. On the other hand, as an example of interfacial doping at the grain boundaries, Bi_2O_3 decreased the specimen conductivity to delay the occurrence of flash sintering to higher temperatures, while it also led to a eutectic reaction and associated premelting-like grain boundary complexion transition that can abruptly increase the specimen conductivity with increasing temperature. Consequently, the onset flash was initiated by a bulk eutectic reaction at a low initial electric field ($E_{initial}$) and by premelting like grain boundary transition at an intermediate $E_{initial}$, respectively. When we further

increased $E_{initial}$, a natural thermal runaway still took place before the occurrence of interfacial and bulk transformation, as predicted by the Arrhenius extrapolation. This is the first study showing that an interfacial complexion transformation can trigger flash sintering, which suggests a new flexibility to tune the flash sintering process.

In a broader perspective, an example of low temperature, transient, interfacial liquid assisting the densification of ceramics under electric field, water-assisted flash sintering (WAFS) was developed using ZnO as a model system. At room temperature, ZnO was densified to ~98% relative density in 30 s in wet Ar + 5% H_2. This method can potentially be extended to consolidate other ceramic systems to achieve fast densification at extremely low furnace temperatures. Furthermore, this study suggests significant technological opportunities for energy and cost savings via exploiting and investigating new ceramic processing science through the interplay of low temperature liquid and electric fields/currents.

Advanced control of electric parameters during electric field assisted sintering also contribute significantly to the advancement of flash sintering. A two-step flash sintering method (TSFS) was developed and clearly demonstrated to improve the microstructure. This study further suggests a new direction that combines the science of conventional sintering with controllable $I(t)$ profile in flash sintering to achieve customized microstructures.

Non-thermal effect of electric field and current on solid oxide microstructures is a long-lasting scientific topic, which gains significance in recent years due to the development of field assist sintering, fuel cells, and solid-state

batteries. In this dissertation, electric field effects on grain growth of in polycrystalline was investigated in the presence of high temperature liquid phase. polarization of ionic defects in PC regions is believed to be the reason of enhanced grain growths at electrochemically reduced locations. Subsequently, a mixed conducting model was developed to qualitatively explain the asymmetry. Other microstructure structure developments including pore formation and abnormal grain growth fitted in the same model. More significantly, electrochemical reduction at the grain boundaries triggered complexion transitions. This finding opens numerous opportunities for grain boundary tailoring that cannot be easily achieved using furnace heating, dopant, or annealing atmosphere. Future studies include modelling of diffusivities of grain boundary complexions induced by electrochemical reduction and reducing the ionic resistance of grain boundaries in solid-state electrolytes.